Journal of Power Sources 697 (2027) 241460

Contents lists available at ScienceDirect

Journal of Power Sources

journal homepage: www.elsevier.com/locate/jpowsour

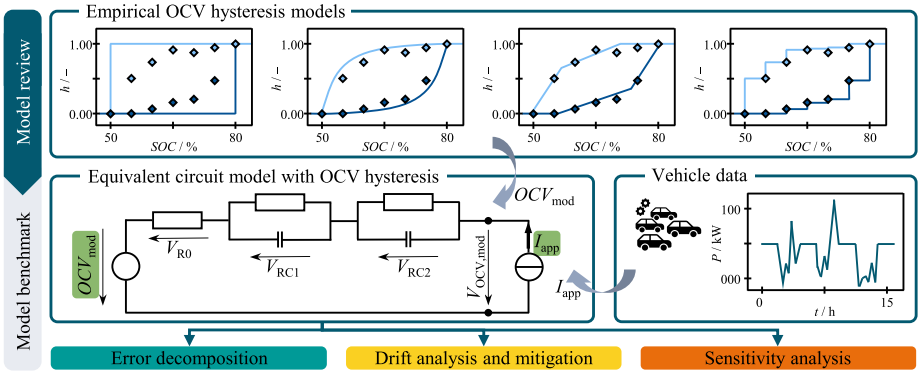
Review article

Comprehensive review and benchmarking of empirical open-circuit voltage hysteresis models for lithium iron phosphate cells including a novel Modified Preisach approach

Valentin Ludwig Elender [a,b,*], Sebastian Ludwig [b], Yannis Horstmann [b], Simon Erhard [b], Jan Philipp Schmidt [a]

[a] Chair of Systems Engineering for Electrical Energy Storage (SysEE), University of Bayreuth, Universitätsstraße 30, Bayreuth, 95447, Bavaria, Germany
[b] BMW Group, Petuelring 130, Munich, 80809, Bavaria, Germany

GRAPHICAL ABSTRACT



HIGHLIGHTS

- Empirical OCV hysteresis models are reviewed and benchmarked in one framework.
- Validation uses a real driving profile from BMW fleet data with added rest phases.
- A novel Modified Preisach model in separated form enforces correct loop orientation.
- Model drift from recuperation and parameter interpolation is quantified.
- Simple strategies reduce drift and parameterization effort without accuracy loss.

ARTICLE INFO

Keywords:
Lithium iron phosphate
OCV hysteresis
Preisach model
Benchmark

ABSTRACT

Open-circuit voltage (OCV) hysteresis affects state estimation in lithium iron phosphate (LFP) graphite cells. This work presents a review and benchmark of empirical open-circuit voltage (OCV) hysteresis models within a framework that treats OCV hysteresis holistically. The Plett Zero-State and One-State model, the Huria model, the Roscher model, and a Modified Preisach model adapted to the proposed framework are considered. Validation uses a real-world profile derived from fleet data (> 75,000 vehicles, > 20 million charging events) and augmented with OCV hysteresis validation points. All models are evaluated on a commercially available

* Corresponding author at: Chair of Systems Engineering for Electrical Energy Storage (SysEE), University of Bayreuth, Universitätsstraße 30, Bayreuth, 95447, Bavaria, Germany.
E-mail address: valentin.elender@uni-bayreuth.de (V.L. Elender).

https://doi.org/10.1016/j.jpowsour.2026.241460
Received 2 June 2026; Received in revised form 14 August 2026; Accepted 6 September 2026
Available online 23 September 2026
0378-7753/© 2026 The Authors. Published by Elsevier B.V. This is an open access article under the CC BY license (http://creativecommons.org/licenses/by/4.0/).
Open access funding enabled and organized by Projekt DEAL.

State of charge estimation

2.6 Ah lithium iron phosphate (LFP) graphite cell for comparability. The Roscher model achieves the best performance, with an overall mean absolute error (MAE) of 1.585 mV and a mean absolute percentage error (MAPE) of 4.7 % for the OCV hysteresis validation points, while also showing the highest robustness against drift. The Modified Preisach, Plett One-State, and Huria model achieve comparable accuracy but exhibit higher sensitivity to drift. Error decomposition indicates that polarization errors dominate under load, whereas hysteresis modeling becomes critical during rest. Sensitivity analysis demonstrates that reducing parameter interpolation decreases drift and measurement effort without compromising accuracy. The results provide guidance for robust hysteresis modeling in automotive battery management systems (BMSs).

1. Introduction

Lithium iron phosphate (LFP) graphite cells are increasingly deployed in battery electric vehicles (BEVs) due to their favorable cost, safety, and cycle-life characteristics compared to nickel-rich chemistries. This trend is reflected in the growing share of LFP graphite cells in the total battery demand of BEVs sold in China, which reached 75 % in 2024 [1]. At the same time, their electrochemical behavior poses specific challenges for battery management systems (BMSs). In particular, the flat open-circuit voltage (OCV) curve over a wide state of charge (SOC) range implies that small voltage errors can translate into large uncertainties in state estimation. Furthermore, the pronounced OCV hysteresis arising from both graphite and LFP electrodes between charge and discharge further complicates state estimation by introducing an additional source of voltage error and, consequently, uncertainty [2–5]. This is especially critical in automotive applications, where the SOC must be estimated accurately over millions of driving and charging events, often without full charge or discharge necessary for recalibration.

Recent work has shown that explicit modeling of OCV hysteresis is essential for robust state estimation of LFP graphite cells, with a variety of modeling approaches emerging in literature [4,6–10]. On the one hand, physics-based models target the underlying behavior on electrode level. For example, the two-phase behavior of LFP can be modeled via different approaches reaching from many-particle theory to phase-field models [11–16]. These modeling approaches explain the phase separation of LFP but not necessarily the LFP hysteresis and offer strong interpretability. Yet, they omit hysteresis contributions of graphite, are typically too complex for onboard BMS implementation, and are not easily formulated in the discrete-time, low-state-dimension form required for embedded observers and filters. On the other hand, empirical models capable of holistic OCV hysteresis modeling, including graphite and LFP contributions, aim to capture hysteretic behavior with moderate parameterization effort and real-time capability. In literature, the Plett Zero- and One-State model [17], the Huria model [18], polynomial models such as the linear Roscher and related formulations [19,20], higher-order models [21], Preisach and Prandtl–Ishlinskii models [10,22,23], and a range of other OCV hysteresis corrections (e.g. [5,24–30]) can be identified as such. In parallel, AI-based and stochastic approaches for holistic OCV hysteresis representation of graphite and LFP have been investigated, either as dedicated hysteresis models, as holistic OCV estimators, or via stochastic noise terms that absorb hysteresis effects during filtering [3,31–35].

This brief overview of the OCV hysteresis model landscape for LFP graphite cells only sketches the main modeling directions and illustrates how broad and heterogeneous this field of research is. From an automotive BMS perspective, empirical models, particularly equivalent circuit models (ECMs) combined with OCV hysteresis sub-models, are often preferred over fully physics-based, AI-based, or stochastic approaches. Unlike these other approaches, such models can be formulated with ease in discrete time with limited state dimension and are highly compatible with common observers and filters such as the extended Kalman filter (EKF).

As this paper is structured as a review and benchmark, Section 3 provides a detailed overview of existing OCV hysteresis models, including the outlined categorization based on their modeling approaches, before focusing on an in-depth review of empirical OCV hysteresis models. Given the scope of this study, which is directed towards the future use of the models in time-discrete, closed-loop observer- and filter-based BMS applications employing ECMs, this focus is legitimate. Subsequently, only empirical approaches are considered for the benchmark. Based on this, it is possible to identify which empirical OCV hysteresis models are suitable for realistic LFP operating conditions. Thus, the benchmark evaluates their performance when embedded in a common environment consisting of the same ECM and validation profile.

From the benchmark perspective, three specific topics are of interest. First, on a model formulation level:

(i) **Preisach implementation:** Preisach-type models are powerful but are often formulated incorrectly for battery applications or rely on the Everett formalism and first order reversal curves (FORCs), which complicates their use in time-discrete BMS frameworks [10,22,36].

And secondly, on a model simulation level:

(ii) **Real-world validation:** Most studies employ idealized laboratory profiles [10,37,38]; systematic benchmarking of OCV hysteresis models against a real driving profile derived directly from a large fleet dataset is rare.

(iii) **Systematic drift analysis:** Drift of empirical OCV hysteresis models caused by realistic profiles with frequent recuperation and from parameter interpolation has mainly been reported qualitatively, e.g. by Ma et al. [38], without detailed analysis of occurrence and mitigation strategies.

This work addresses these points within the intended review and benchmark of OCV hysteresis models for LFP graphite cells, with a focus on empirical models. Therefore, it is essential to conduct a comprehensive analysis of real-world data on customer charging and driving behavior to establish a reliable foundation. To this end, the BMW i4 eDrive40 fleet, comprising more than 75,000 vehicles and over 20 million charging events, is evaluated. This analysis yields a validation profile based on a real driving profile of this vehicle that reflects typical customer behavior. Thus, the validation profile is extended by rest phases to decompose errors into hysteresis and polarization contributions and to provide a true validation of OCV hysteresis model accuracy during rest.

For benchmarking with this validation profile, the goal is to derive a unified time-discrete and BMS-compatible ECM framework that is observer- and filter-ready. Compatibility is understood here on the model and algorithm layer, comprising separability, differentiability, and the computational structure of a single time step, whereas the target implementation layer, i.e. code generation, fixed-point scaling, and the measurement of execution time and memory occupation on automotive microcontroller units (MCUs), is deliberately not addressed, as it depends on the target, the compiler, and the toolchain rather than on the hysteresis model. In the same sense, the benchmark is conducted in open loop and compares the models in the voltage domain, as the SOC of the framework derived here follows from Coulomb counting and is therefore identical for all models under comparison. A SOC error caused by OCV hysteresis arises only in closed loop and is

then a property of the estimator rather than of the hysteresis model. The approach separates major OCV loops and its hysteresis wherever possible. Approaches using an OCV without hysteresis, the Plett Zero-State and the One-State model [17], the Huria model [18], the Roscher model [19], and a Modified Preisach model are analyzed in detail. A key contribution is the Modified Preisach model tailored to holistic OCV hysteresis representation of LFP and graphite. It enforces the correct clockwise loop orientation and is implemented in separated form with respect to major OCV loops. Moreover, it is parameterized from measured minor loops without requiring FORCs, thereby making Preisach-type modeling more accessible for BMS applications.

Besides the evaluation of each OCV hysteresis model's mathematical characteristics, parameterization effort, and accuracy, shortcomings such as drift due to frequent recuperation and parameter interpolation are identified and analyzed. Simple strategies to mitigate drift are investigated in a sensitivity study, demonstrating that drift can be reduced and that parameterization and measurement efforts can be significantly lowered while preserving accuracy.

Therefore, the overall scope is to provide both a comprehensive overview of OCV hysteresis modeling approaches in literature and concrete guidance for the selection and formulation of robust, observer- and filter-ready hysteresis models in automotive BMSs. The remainder of this paper is structured as follows: Section 2 describes the data acquisition, containing the measurements necessary for modeling, as well as an analysis of customer behavior and the derivation of a validation profile from a real driving profile; Section 3 reviews common OCV hysteresis modeling approaches, with a focus on empirical models, and formulates the most promising empirical OCV hysteresis models together with a common ECM within an observer- and filter-ready framework; Section 4 presents the benchmarking results; Section 5 discusses error decomposition, drift phenomena, sensitivity, and a comparison with existing literature; and Section 6 concludes with key findings and recommendations for BMS applications. Given the number of modeling approaches covered, the outcome of each step of this work is condensed into three levels of synthesis that can be read independently of the detailed analysis: Table 4 condenses the literature review by clustering all empirical OCV hysteresis models according to shape, loop capability, and separation strategy, and by stating which clusters are carried into the benchmark; Table 5 condenses the model formulation and mathematical properties of the benchmark into a single comparative view; and Table 10 condenses the benchmark itself into a comparative assessment and a recommended application for each model. The detailed sections provide the reasoning behind these tables and are not required to follow the comparison.

2. Modeling data acquisition

This section describes all procedures related to modeling data acquisition. It includes the experimental determination of several modeling quantities, as well as a fleet data analysis of customer charging and driving behavior, resulting in a validation profile derived from a real driving profile. Thus, the following will be addressed:

- OCV measurement via galvanostatic intermittent titration technique (GITT),
- OCV hysteresis measurement via GITT,
- parameter determination for the ECM under investigation via hybrid pulse power characterization (HPPC),
- analysis of real BEV customer charging and driving behavior,
- and derivation of a validation profile from a real driving profile.

All data were obtained on a LithiumWerks ANR26650m1b LFP graphite cell with power design. Using commercially available cells ensures that the results are reproducible and comparable with existing data. The cell is specified by an upper cut-off voltage of 3.6 V, a lower cut-off voltage of 2.0 V, a nominal voltage of 3.3 V, a nominal capacity of 2.6 Ah, and a nominal energy of 8.58 Wh [39]. All measurements were performed at 25 °C in a climate chamber, since the effects of temperature are neglected in this work. Accordingly, the validity domain of the benchmark presented here is an operating temperature of 25 °C, the charging rate (C-Rate) range covered by the validation profile, and a single commercially available cell. This restriction is deliberate and follows from the objective of the work: a controlled comparison of OCV hysteresis formulations requires an identical cell, ECM, parameterization procedure, and validation profile, so that observed differences are attributable to the hysteresis models alone. A qualification of an individual model over the full automotive operating envelope is not intended.

2.1. Acquisition of parameterization data

All OCV, OCV hysteresis, and ECM-parameter measurements were performed using a Battery Dynamics "High Resolution Battery Tester HTR – M10" with an absolute voltage measurement precision of ≤0.01 % full scale range (FSR), an absolute set precision of ≤0.01 % FSR, and a voltage resolution of 0.001 mV. For current, three ranges are available (±10 A, ±0.5 A, ±50 mA), each with an absolute measurement and set precision of ≤0.01 % FSR. All tests' SOCs are set at a C-Rate of C/3 and, if necessary, with constant voltage (CV) charging down to C/50.

OCVs are obtained from relaxed voltage data after 5 h following the GITT test procedure in Table 1. The resulting OCVs are OCV_{ch} and OCV_{dch}, referred to as the major OCV hysteresis loop in literature. The relaxed voltage after 5 h has not fully reached steady state and shows a mean relaxation gradient $\mathrm{d}OCV/\mathrm{d}t$ of −0.619 mV/h for OCV_{ch} and 0.492 mV/h for OCV_{dch}. Since OCV hysteresis for the investigated cell is on the order of mV, this relaxation must be extrapolated. To capture the relaxation behavior of the residual polarization $\Delta\eta_{\mathrm{residual}}$ in mV, the time-domain distribution of relaxation times (DRT) method from Schmidt and Ivers-Tiffée [40] is applied. In this process, a polarization offset of the DRT over the entire rest phase, equal to $\Delta\eta_{\mathrm{residual}}$, is determined by minimizing the mean absolute error (MAE) between the measured relaxation and the offset DRT fit over the last 1 h of relaxation. The resulting fully relaxed major OCV loops are then used for model parameterization and simulation of OCV and OCV hysteresis, employing piecewise cubic Hermite spline interpolation if necessary, in Sections 3.2, 3.3, and 3.4.

The same GITT-based procedure is applied for OCV hysteresis (see Table 1). First, the definition of OCV hysteresis used in this work must be clarified. Here, OCV hysteresis always refers to the measured relaxed, load-free OCV and not to hysteresis measured under load. Thus, OCV hysteresis measurements always encompass the hysteresis contributions of both graphite and LFP. In literature, graphite hysteresis is reported to be approximately 10 mV, whereas LFP hysteresis reaches approximately 20 mV [5,16,41]. Furthermore, the terminologies for OCV hysteresis used in literature must be explained. A minor OCV hysteresis loop describes the full transition from OCV_{dch} to OCV_{ch} and back to OCV_{dch}, always reaching full saturation of OCV hysteresis at the start, the turning, and the end point of each minor loop. Such a minor loop is also termed an OCV hysteresis eye. In contrast, the term FORC denotes a more general concept for describing and measuring hysteresis. In the context of OCV hysteresis, a FORC is obtained by first fully charging or discharging the cell to reach saturation, then reversing the current and (partially) charging or discharging to a chosen reversal point. From this point, the OCV response is recorded while the current is reversed again towards the original direction. Repeating this for multiple reversal points yields a family of FORCs. The terminologies major and minor loop, as well as FORCs, are highlighted in Fig. A.9 in Appendix A. Thus, in this work, minor OCV hysteresis loops extracted from GITT measurements are used for parameterization and simulation. For model parameterization, $N_{\mathrm{loop}} = 5$ minor loops are measured, each spanning a saturation interval of $\Delta SOC_{\mathrm{saturation}} = 30\,\%$. Thereby, all major OCV hysteresis regions relevant for automotive applications

Table 1
Experiments conducted on the ANR26650m1b LFP graphite cell for model parameterization.

	SOC intervals	Relaxation time	Comment
$GITT_{ch}$	0 % : Δ2 % : 10 %, 10 % : Δ5 % : 65 %, 65 % : Δ2 % : 75 %, 75 % : Δ5 % : 95 %, 95 % : Δ1 % : 100 %	5 h	Charge direction, used for OCV modeling with DRT extrapolation including increased resolution in areas with significant OCV changes
$GITT_{dch}$	100 % : Δ1 % : 95 %, 95 % : Δ5 % : 75 %, 75 % : Δ2 % : 65 %, 65 % : Δ5 % : 10 %, 10 % : Δ2 % : 0 %	5 h	Discharge direction, used for OCV modeling with DRT extrapolation including increased resolution in areas with significant OCV changes
$GITT_{hysteresis}$	60 % : Δ5 % : 30 % : Δ5 % : 60 %, 70 % : Δ5 % : 40 % : Δ5 % : 70 %, 80 % : Δ5 % : 50 % : Δ5 % : 80 %, 90 % : Δ5 % : 60 % : Δ5 % : 90 %, 95 % : Δ5 % : 65 % : Δ5 % : 95 %	5 h	Minor loops, used for OCV hysteresis modeling with DRT extrapolation without increased resolution in areas with significant OCV changes
$HPPC_{ch}$	0 % : Δ5 % : 10 %, 10 % : Δ10 % : 90 %, 90 % : Δ5 % : 100 %	5 h	Charge pulses, used for ECM parameterization (series resistance and RC elements) with linear OCV correction (various C-Rates)
$HPPC_{dch}$	100 % : Δ5 % : 90 %, 90 % : Δ10 % : 10 %, 10 % : Δ5 % : 0 %	5 h	Discharge pulses, used for ECM parameterization (series resistance and RC elements) with linear OCV correction (various C-Rates)

based on BEV customer charging and driving behavior are covered (Section 2.2). In Section 3.2, the average SOC of each minor OCV hysteresis loop, $SOC_{i,\mathrm{avg,loop}}$, is used for the parameterization of each loop itself. Based on Table 1, the resulting $SOC_{i,\mathrm{avg,loop}}$ values are 45 %, 55 %, 65 %, 75 %, and 80 %. For these measurements, a 5 h relaxation time yields an absolute relaxation gradient $|\mathrm{d}OCV/\mathrm{d}t|$, including the charge and discharge direction of the minor loops, of 0.2322 mV/h, which is also corrected via the DRT-based approximation described above for the OCVs according to Schmidt and Ivers-Tiffée [40]. The extracted OCV hysteresis data are then combined with the major loop OCVs and reformulated into hysteresis metrics, such as the absolute value $H(SOC(t),t)$ in mV, which is the hysteresis voltage added to OCV_{dch}, or the relative value $h(SOC(t),t)$, which describes the additional OCV hysteresis $H(SOC(t),t)$ normalized by the maximum OCV hysteresis at this SOC, i.e. the difference between OCV_{ch} and OCV_{dch}. These fully relaxed minor OCV loops are used for model parameterization and simulation of OCV hysteresis, again employing piecewise cubic Hermite spline interpolation if necessary, in Sections 3.2, 3.3, and 3.4. The HPPC tests provide data for the parameterization of an ECM with a series resistance and resistance-capacitor (RC) elements describing cell polarization and follow the described test procedure in Table 1. At each set SOC in charge direction, charging pulses with C-Rates C/20, C/10, C/3, 1 C, 2 C, and 3.5 C are applied, each followed by 5 h relaxation. The same procedure is then repeated with discharge pulses in discharge direction. Separating the characterization in charge and discharge direction is necessary to isolate polarization behavior from OCV hysteresis effects. The HPPC data are then used to fit the ECM with a series resistance and RC elements. Each pulse is either corrected for the incremental ΔOCV from the pulse's charge throughput or for long-term relaxation due to the two-phase behavior of LFP cathodes. The fitting of the extracted HPPC data for an ECM is discussed in Section 3.3.

Detailed information on the tests can be found in Table 1. Besides any temperature variation, the influence of C-Rate on OCV and OCV hysteresis, as described in Roscher et al. [42], is neglected. All SOC set points as well as all GITT steps underlying the OCV and OCV hysteresis measurements are applied at C/3, so that the data used for the parameterization and validation of the hysteresis models are obtained under identical and moderate current conditions. The HPPC pulses used for the ECM parameterization cover C/20 to 3.5 C in both charge directions and thus exceed the current range of the validation profile, which remains below |2 C| (see Section 2.2).

2.2. Analysis of customer behavior and acquisition of validation data

The aim of this work is to investigate OCV hysteresis modeling under realistic conditions. To this end, a statistical analysis of the charging and driving behavior of the BMW i4 eDrive40, equipped with a 81.3 kWh battery pack, is carried out across all markets, covering a fleet of more than 75,000 vehicles and more than 20,000,000 charging events. This vehicle is investigated because its pack size aligns with the increasing importance of LFP battery packs and long-term changes in average BEV battery pack sizes reported by the International Energy Agency [1,43]. The following analysis of charging and driving behavior focuses on SOC and depth of discharge (DOD) ranges. The DOD, like the SOC, refers to the amount of charge in Ah, whereas the state of energy (SOE), which is used later, refers to the amount of energy in Wh.

For the charging behavior, the joint distribution of SOC ranges of three charging types are evaluated: AC, $\mathrm{DC_{mid}}$ with $P \leq 100\,\mathrm{kW}$, and $\mathrm{DC_{high}}$ with $P > 100\,\mathrm{kW}$. For the driving behavior, the PDF for all trips regarding their DODs is of interest. The key findings are summarized in Table 2 and Fig. 1. Across all customers, markets, and charging types, 62.45 % of all charging events result in $SOC_{\mathrm{end}} \leq 90\,\%$. As seen in Fig. 1, SOC_{end} peaks around 80 %. Fig. 1(d) and Table 2 show that 16.7 % of customers drive a DOD of less than 7.5 %, and 82.0 % reach a DOD between 7.5 % and 25 % per trip. With this statistical background on customer behavior, a real driving profile can be selected for further analysis. This profile is based on the actual driving data of a sample customer and includes two driving segments on rural roads and one driving segment on the highway. Fig. G.10(a) and (b) in Appendix G display the speed and the corresponding battery pack power request of the real driving profile of the selected sample customer, which will be used to derive the validation profile investigated here. The maximum jellyroll core temperature estimated by the BMS for the real driving profile is between 21 °C and 29 °C, yielding a mean estimated maximum jellyroll temperature of 25.7 °C and supporting the assumption of a constant operating temperature of 25 °C for this study. First, the selected profile is scaled to the cell used in this study using the cell energy $E_{\mathrm{cell,26650}}$ and the pack energy $E_{\mathrm{pack,i4}}$:

$$P_{\mathrm{cell,26650}} = \frac{P_{\mathrm{pack,i4}} \cdot E_{\mathrm{cell,26650}}}{E_{\mathrm{pack,i4}}} \tag{1}$$

After scaling, the absolute maximum C-Rate at the lower cut-off voltage of 2.0 V is 1.754 C for maximum discharge power and 1.934 C for maximum charge power. This supports restricting the analysis in this paper to moderate C-Rates. For reference, the drivetrain power of 250 kW and the pack energy of 81.3 kWh correspond to a maximum pack-level C-Rate of approximately 3.1 C, so that the selected profile covers about 60 % of the peak capability of the vehicle. The profile therefore reflects the moderate peak currents characteristic of customer driving, rather than an idealized laboratory cycle.

The scaled profile results in a total SOE throughput of 19.1 %. To obtain a realistic validation profile, this profile is repeated twice, leading to a throughput of 38.2 %. Combining the observations of customer behavior regarding SOC and DOD ranges, the scaled and repeated validation profile derived from a real driving profile starts at $SOC_{\mathrm{start}} = 90\,\%$ on OCV_{ch}. From this initial condition, the OCV hysteresis models

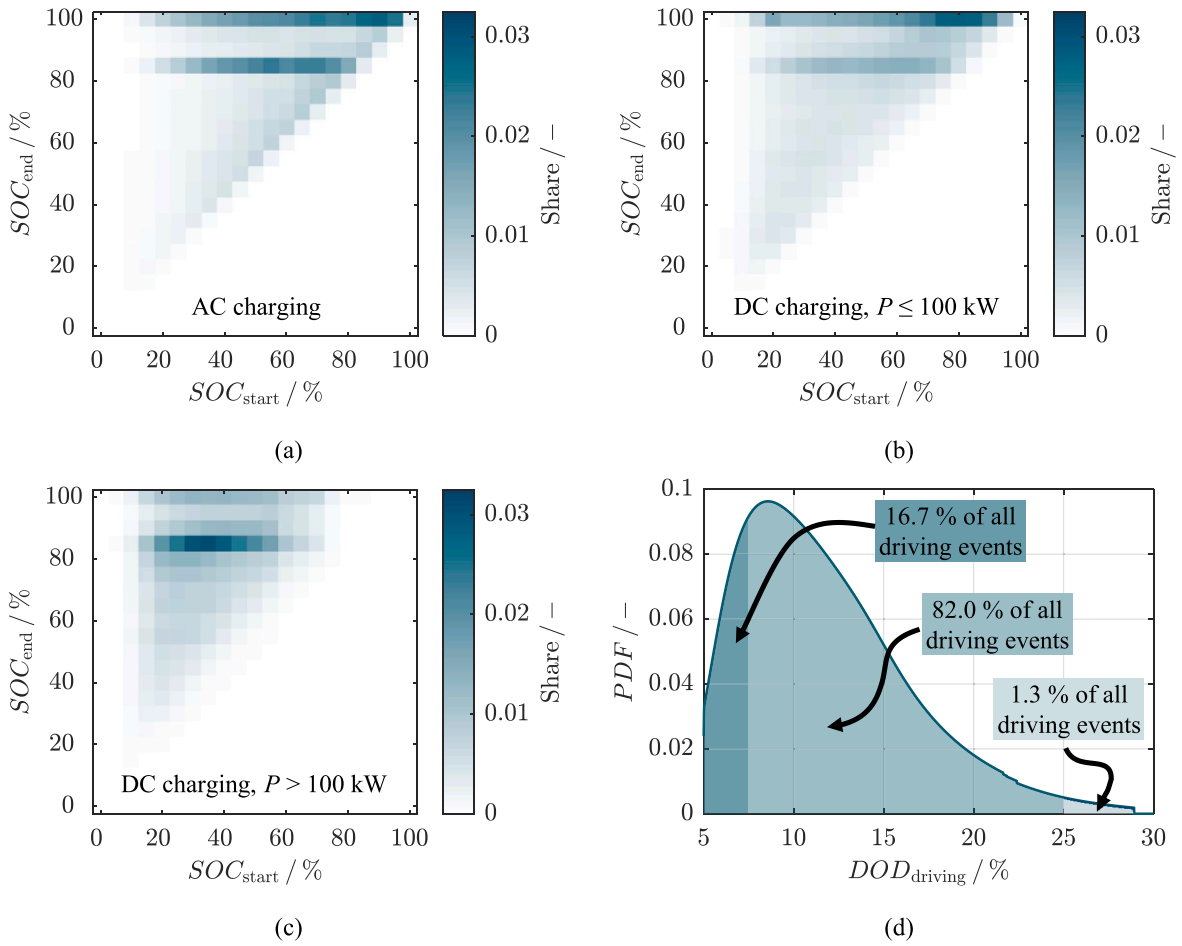


Fig. 1. Fleet data showing the charging and driving behavior for the BMW i4 eDrive40 (250 kW drivetrain and 81.3 kWh battery pack). (a) Joint distribution of SOC_{start} and SOC_{end} for all available AC charging events. (b) Joint distribution of SOC_{start} and SOC_{end} for all available DC_{mid} charging events with $P \leq 100$ kW. (c) Joint distribution of SOC_{start} and SOC_{end} for all available DC_{high} charging events with $P > 100$ kW. (d) PDF of $DOD_{driving}$ for all trips.

Table 2
Relevant shares of all available AC, DC_{mid}, and DC_{high} charging events with respect to SOC_{end} and relevant $DOD_{driving}$ shares for all trips of the BMW i4 eDrive40.

	Share AC /–	Share DC_{mid} /–	Share DC_{high} /–		Share driving /–
$0\,\% < SOC_{end} \leq 100\,\%$	0.815	0.075	0.110	$DOD_{driving} > 25\,\%$	0.013
$SOC_{end} > 90\,\%$	0.396	0.399	0.207	$7.5\,\% < DOD_{driving} \leq 25\,\%$	0.820
$SOC_{end} \leq 90\,\%$	0.604	0.601	0.793	$DOD_{driving} \leq 7.5\,\%$	0.167
$SOC_{end} \leq 80\,\%$	0.305	0.360	0.452		

are compared. To cover the typical customer DOD ranges shown in Table 2 and to validate the OCV hysteresis models experimentally, the profile is interrupted after SOE throughputs of 7.5 %, 25.0 %, and 5.7 % for rest phases of 5 h each. Since the voltage of LFP graphite cells varies only slightly over broad SOC ranges and the profile starts on OCV_{ch} at $SOC_{start} = 90\,\%$, these SOE throughputs closely approximate the corresponding DODs (see Table 3). Thus, the validation profile is augmented with realistic stops that reflect typical customer DODs, each followed by a rest phase, consistent with the thresholds observed in Fig. 1 and Table 2. Including these rest phases enables validation of the OCV hysteresis models at four distinct OCV hysteresis validation points: after charging to OCV_{ch}, within the transition between OCV_{ch} and OCV_{dch}, near OCV_{dch}, and at saturation along OCV_{dch}. Fig. G.10(c) in Appendix G shows the voltage response of the validation profile, i.e., of the scaled and augmented battery-pack power $P_{cell,26650}$ including the rest phases. Owing to measurement accuracy and the complex relaxation behavior of LFP, the normalized OCV hysteresis $h_{measured}$ listed in Table 3 is observed after 5 h of relaxation. These OCV hysteresis validation points are denoted as "parking points" P_1, P_2, P_3, and P_4, indicating relaxed OCVs including OCV hysteresis. The segments between are declared as load and rest phases, namely $Load_1$, $Load_2$, and $Load_3$ as well as $Rest_1$, $Rest_2$, and $Rest_3$.

Other than the parameterization data, the validation data are acquired using an Arbin Instruments "Laboratory Battery Testing System LBT21084 ±5 V 5 A". This tester offers a voltage range of ±5 V and a current range of ±5 A. The absolute voltage measurement precision is ≤0.01 % FSR, with an absolute set precision of ≤0.01 % FSR, and a voltage resolution of 0.001 mV. For currents within ±5 A, the datasheet

Table 3
OCV hysteresis validation points measured on the ANR26650m1b LFP graphite cell for model validation.

SOC_{parking} /%	OCV_{measured} /V	h_{measured} /−	$\mathrm{d}OCV_{\text{measured}}/\mathrm{d}t$ /mV/h
88.1	3.337	0.762	−0.069
80.8	3.335	0.244	0.109
56.0	3.296	0.076	0.093
50.4	3.294	0.006	0.187

specifies a measurement precision of ≤0.0003 % FSR and a control accuracy of ≤0.02 %. Although the calibration procedures of the two testers used for parameterization and validation data acquisition may differ, direct comparison of cell voltages measured with both devices showed deviations below 0.1 mV. Differences in measurement accuracy or calibration between the Arbin and Battery Dynamics systems, both in absolute voltages and FSR, are therefore considered negligible for this study. Besides negligible deviations due to current and voltage accuracy as well as cell-to-cell variation, the actual SOC slightly deviates from the target $SOC_{\text{start}} = 90\,\%$ (see Table 3). Furthermore, the mean surface temperature at the four OCV hysteresis validation points is 27.4 °C, instead of the 25.0 °C setpoint of the climate chamber. Such deviations between the climate chamber setpoint and Battery Dynamics tester were not observed, despite using the same setup and the same climate chamber. Therefore, using the Battery Dynamics tester as temperature calibration for the setup and the climate chamber, this offset is likely due to the temperature measurement accuracy of the Arbin tester, as all load-induced temperature variations should decay after 5 h of relaxation.

Unlike the OCV and OCV hysteresis measurements, no DRT-based relaxation extrapolation is applied here, because the relaxation gradients $\mathrm{d}OCV/\mathrm{d}t$ in Table 3 are sufficiently small compared to those in the GITT measurements. The difference in magnitude of these relaxation gradients $\mathrm{d}OCV/\mathrm{d}t$ is attributed to the two-phase transition behavior of LFP, which can yield different relaxation characteristics depending on DOD and C-Rate, meaning how a SOC point is reached (GITT vs. constant current (CC) charging/discharging vs. dynamic cycling). The only notable deviation occurs for the hysteresis at the first OCV hysteresis validation point, as quantified by h_{measured} (see Table 3). Ideally, OCV_{measured} at this point should match OCV_{ch}, since the start SOC is set from 0 % using a C/3 charging protocol. However, the two-phase transition behavior may introduce not only differences in relaxation behavior but also differences in the OCV itself, which has already been observed by Roscher et al. [42] for varying C-Rates. Such effects cannot be captured by empirical models and lie outside the scope of this work, requiring future investigation, as they are not systematically investigated in literature. Consequently, this deviation is neglected in subsequent model validations in Sections 4 and 5, while the remaining OCV hysteresis validation points are considered valid.

3. Review and model description

With the review and benchmark scope of this work, the following section presents a detailed overview of existing OCV hysteresis models, including the outlined categorization based on their modeling approaches, before focusing on an in-depth review of empirical OCV hysteresis models. As already stated, given the scope of this study, this focus is legitimate. The review is followed by an in-depth analysis of the most relevant empirical OCV hysteresis models, including the derivation of a Modified Preisach model. To facilitate a meaningful comparison, an ECM based on established literature is derived and ultimately combined with the different hysteresis models at the end of this section.

3.1. Literature review on OCV hysteresis models

A variety of modeling approaches have been proposed to describe the OCV hysteresis observed in LFP graphite cells. Models either explicitly represent OCV hysteresis holistically or primarily address the underlying physical behavior on electrode level that causes hysteresis. The main modeling strategies for OCV hysteresis in LFP graphite cells can be categorized as physical approaches, empirical approaches, and AI-based or stochastic approaches. In this work, only physical models tailored for LFP will be highlighted, while graphite models will be omitted. These models originate from descriptions of the fundamental phase-separation mechanisms governing LFP behavior. These models can be further classified into six subtypes: nucleation and growth models [11], phase-field models [12], core–shell models [13], variable diffusivity models [14], resistive reactant models [15], and many-particle models [16]. Among these, only the many-particle model inherently accounts for LFP hysteresis. The cited publications represent key references for each modeling approach. AI-based and stochastic modeling approaches focusing on holistic OCV hysteresis modeling for graphite and LFP have also been explored. Three principal directions can be distinguished. First, dedicated hysteresis models are developed with neural networks, where the network either directly learns the transition between OCV_{dch} and OCV_{ch} from data or indirectly learns parameters describing OCV hysteresis. These models, typically capable of representing major and minor OCV hysteresis loops, are usually combined with filtering approaches [31–33]. Second, combined OCV estimation methods use neural networks to estimate OCV (including hysteresis) holistically, so that major and minor hysteresis loops are inherently captured in the learned mapping [3,34]. Third, some models introduce stochastic noise terms to account for and compensate OCV hysteresis effects during state estimation, thereby treating unmodeled or uncertain hysteresis behavior probabilistically [35]. Finally, numerous empirical models have been proposed, among which the Plett One-State model [17] and the Preisach model [44,45] are the most prominent. Both originate from hysteresis modeling in magnetization theory. The in-depth review of empirical approaches in preparation for the subsequent benchmark follows after an elaboration of further categorization based on various model characteristics. This further characterization, as well as the subsequent review and benchmark of the empirical models, is based on a holistic representation of OCV hysteresis, including contributions from both graphite and LFP. Accordingly, unless otherwise specified, the term OCV hysteresis modeling refers to the combined representation of graphite and LFP contributions, consistent with the corresponding measurement definition. The implications of this combined representation, particularly the influence of graphite, are discussed in Sections 4 and 5. An overview of the already introduced categorization by modeling approach is given in Fig. 2.

Beyond their physical interpretability, OCV hysteresis models can also be categorized according to how they separate model components. Some models treat OCV and OCV hysteresis jointly, i.e., as OCV models that inherently include hysteretic behavior. Others implement OCV hysteresis as an additional OCV correction term, independent of the chosen reference OCV. For a complete categorization, all OCV hysteresis models can further be differentiated according to whether they describe both major and minor hysteresis loops or only major loops (see Section 2).

The in-depth review of empirical approaches is performed irrespective of their separation strategies or loop capabilities. As given by the scope of this work, AI-based and stochastic approaches and physical models are deliberately omitted to ensure maximum comparability among the later investigated empirical models. Table 4 summarizes all relevant empirical OCV hysteresis models and represents the first level of synthesis of this work: it condenses each cluster into its shape, its loop capabilities, and whether it is implemented in separated or combined form, and states whether it is carried into the benchmark.

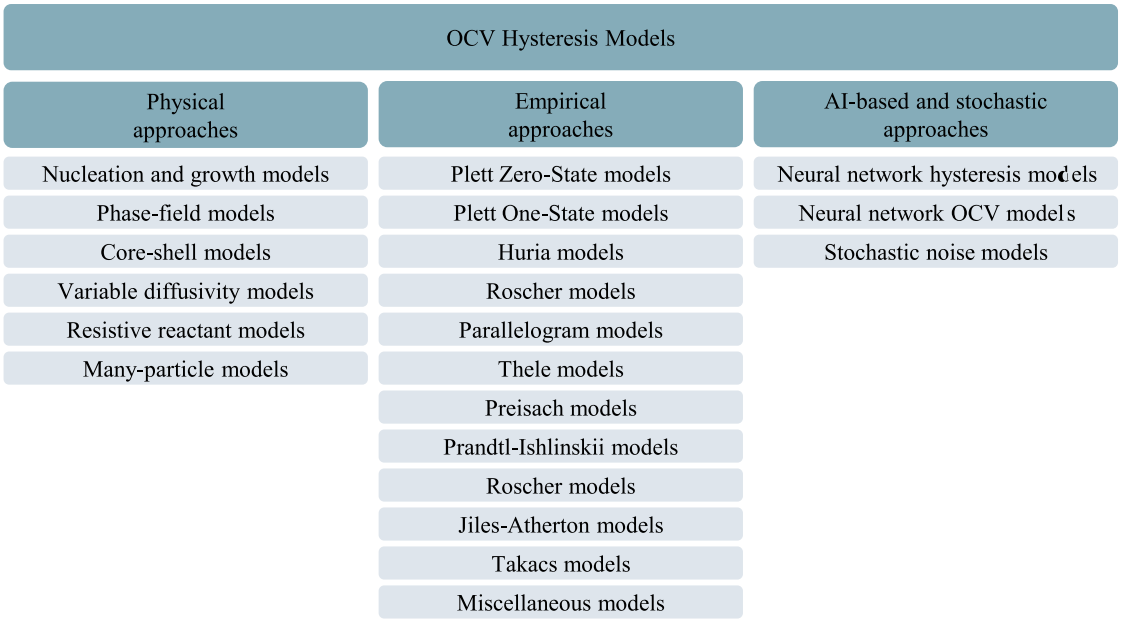


Fig. 2. Categorization of OCV hysteresis models developed in this work according to modeling approaches reported in the literature. Physical approaches focus exclusively on LFP-specific behavior, whereas empirical approaches as well as AI-based and stochastic approaches represent OCV hysteresis holistically, including both graphite and LFP contributions.

Table 4
Clusters of empirical OCV hysteresis models, condensing the review of Section 3.1 and identifying the clusters carried into the benchmark.

	Shape	Loop type	$OCV = OCV_{ref} + H$	$OCV = f(SOC, H)$	Sources	Benchmark
Plett Zero-State	Switching	Major	✓		[17,46–50]	✓
Plett One-State	Exponential	Major, minor	✓		[6,7,17,51–57]	✓
Huria	Exponential	Major, minor	✓	✓	[8,9,18,58–63]	✓
Roscher	1st-order polynomial	Major, minor	✓		[4,19,64–71]	✓
Parallelogram	1st-order polynomial	Major, minor	✓		[20,72]	✗
Thele	2nd-order polynomial	Major, minor	✓		[21,73,74]	✗
Preisach	Switching	Major, minor	✓	✓	[10,22,44,45,75–80]	✓
Prandtl–Ishlinskii	Switching	Major, minor		✓	[23,81–83]	✗
Jiles–Atherton	Non-linear	Major		✓	[24,84]	✗
Takacs	Non-linear	Major, minor	✓	✓	[25,85]	✗

Here, $OCV = OCV_{ref} + H$ denotes separable models, whereas $OCV = f(SOC, H)$ denotes combined models that treat OCV as a function of SOC and hysteretic history. The following review provides the main characteristics and mathematical forms of each cluster and the reasoning behind their inclusion in or exclusion from the benchmark; for the comparative overview alone, Table 4 is sufficient. In addition, empirical models not belonging to any of the listed clusters, and therefore not included in the table, are briefly described.

Plett zero-state model. One of the models in Plett [17] is the Plett Zero-State OCV hysteresis model. It describes only major hysteresis loops by switching between OCV_{ch} and OCV_{dch} depending on the load. Despite this switching behavior, hysteresis is still treated as an additive term around the average OCV OCV_{avg}, enabling a separated description of OCV and hysteresis. Due to its simplicity, it is still used in recent works ranging from parameter estimation studies to general and automotive-focused SOC estimation using filters and observers, as well as temperature-dependent OCV hysteresis investigations [46–50]. Owing to its switching behavior and separated formulation, this approach is included in the present benchmark.

Plett One-State model. A more advanced OCV hysteresis model introduced by Plett [17] is the Plett One-State model. Derived from magnetization theory, it is one of the most widely used OCV hysteresis models. It describes hysteresis as an additive separated variable to OCV_{avg}, governed by a differential equation that enables the representation of major and minor loops. Solving the differential equation analytically or numerically yields exponential minor loop trajectories that asymptotically converge to the major loop. The model is widely applied in recent publications in combination with state estimation, observer and filter enhancements, fractional-order models, and model extensions or multi-physical model combinations [6,7,51–57,86]. Due to its prevalence and balanced trade-off between complexity, parameterization effort, and its state-variable formulation, it is included in this study.

Huria model. The model by Huria et al. [18] follows a similar concept to the Plett One-State model but references hysteresis directly to OCV_{ch} or OCV_{dch} depending on the applied load. The OCV and its hysteresis are modeled jointly, while still allowing major and minor loops to be represented. As a consequence, hysteresis cannot be directly treated as a separate state variable (see Section 3.2), even though OCV and hysteresis remain separable through the explicit use of OCV_{ch} and OCV_{dch} as major loop references. Solving the governing differential equation again yields exponential minor loop trajectories converging to the major loops. Huria et al. [18] combine their model with an EKF. Based on that, several works investigate the model with combined state and parameter estimations, comparisons to other LFP

modeling approaches, combined filter methods and model extensions or multi-physical model combinations [8,9,58–63]. The Huria model is therefore also considered here due to its similarity to the Plett One-State model and comparable parameterization effort, while differing in its governing equations.

Roscher model. In Roscher and Sauer [19], a linear OCV hysteresis model in combination with a state observer is introduced. A hysteresis factor $0 \leq \Psi \leq 1$ serves as a weighting factor between OCV_{ch} and OCV_{dch}. The model's linear character arises from defining Ψ as a sum of weighted integrals with saturation at $\Psi = 0$ and $\Psi = 1$. These weighted integrals lead to piecewise linear minor loop trajectories. The model is thus separated from OCV_{ch} and OCV_{dch} and can represent both major and minor loops. Based on Roscher and Sauer [19], Duong et al. [64] combine this linear model with an EKF, while Jöst et al. [4] generalize it to a sum of n integrals rather than two. For their model-in-the-loop analysis, the order is reduced to $n = 1$. This reduced linear hysteresis model, with a single slope interpolating between OCV_{ch} and OCV_{dch}, directly derived from Roscher and Sauer [19], is widely used in literature [65–71]. Due to its simple parameterization, separated structure, and loop capabilities, this model is included in the following analysis.

Parallelogram model. The parallelogram hysteresis model introduced by Duong et al. [20] and extended by Ko and Choi [72] again employs a hysteresis factor $0 \leq \alpha \leq 1$ as a weighting factor between OCV_{ch} and OCV_{dch}. The difference to Roscher and Sauer [19] lies in the definition of α. Instead of a sum of weighted integrals with saturation, which yields piecewise linear trajectories, α is defined directly by piecewise linear functions. Duong et al. [20] use a sum of two piecewise linear functions, while Ko and Choi [72] generalize this to a sum of k piecewise linear functions. Both works validate a separated model, which can describe major and minor loops, within an EKF. Assuming that the number of integrals n in the generalized Roscher model from Jöst et al. [4] equals the number of piecewise linear functions k in Ko and Choi [72], the approaches are mathematically equivalent, with the same number of parameters and the same degree of freedom (DOF) for piecewise linear minor loop trajectories. For this reason, the parallelogram model is not considered further.

Thele model. In Thele et al. [21], an OCV hysteresis model for nickel metal hydride (NiMH) batteries is proposed. Due to the shape of its hysteresis trajectories, the model can also be applied to LFP graphite cells. The model separates a reference OCV_{dch} and an additional OCV hysteresis that must remain below OCV_{ch}. This OCV hysteresis voltage describes the transition between the two major loops and thus the minor loop trajectories. The concept is based on the charge amount $Q_{\mathrm{hyst,max}}$ required to transition between OCV_{dch} and OCV_{ch}. A maximum deviation ΔH_{max} in both charge and discharge direction from a linear slope drawn between OCV_{dch} and OCV_{ch} at $Q_{\mathrm{hyst,max}}/2$ is used to define three characteristic points for each charge direction, enabling the fit of a 2nd-order polynomial for a complete minor loop trajectory. For operations with turning points inside a minor loop (with smaller charge throughput than $Q_{\mathrm{hyst,max}}$), ΔH_{max} is scaled with the actual throughput, again providing three points for fitting a 2nd-order polynomial. Based on Thele et al. [21], the combination with observers and filters for SOC estimation and temperature-dependent parameterization is explored [73,74]. For dynamic loads, this approach requires extensive parameterization and complex simulation, as every turning point within a minor loop must be associated with a dedicated 2nd-order polynomial and mapped to its starting configuration and major loop references (OCV_{dch} or OCV_{ch}). Due to this complexity in minor loop simulation, the 2nd-order polynomial approach is not pursued further in this study.

Preisach model. The Preisach model, originating from magnetization theory [87], is widely used for OCV hysteresis modeling. It represents hysteresis as a superposition of hysterons with upper and lower switching thresholds (α, β), each switching between −1 and +1 depending on the input history. In the classical model, hysterons are distributed over the Preisach triangle $\alpha \geq \beta$ and combined with a weight function μ. Hysteresis is then obtained by integrating the weighted hysteron states. This yields major and minor loops with wiping-out and congruency properties [87].

Two main discretization strategies exist. The Everett-based approach uses FORCs to identify changes in the Preisach integral at discrete points (α, β) on the Preisach triangle and reconstructs a discrete weight distribution, or directly uses the so-called Everett formalism from the integral [87]. The second approach directly discretizes the Preisach triangle into a finite set of hysterons and fits their weights μ to measured loops [88]. Both can reproduce major and minor loops, but the classical Preisach model naturally generates counter-clockwise loops. For OCV hysteresis, clockwise, monotonically increasing loops are required. This can be enforced by modified integration domains via a moving support, resulting in a rectangular Everett domain rather than the standard triangle [89] or by an impulsive correction of μ within the Preisach triangle [36]. Both approaches lead to slightly modified Preisach models and prove that the Everett formalism identified from FORCs can intrinsically encode the required loop-orientation corrections for OCV hysteresis. Thus, the approach introduced by Visone and Zamboni [36] is the one most commonly adopted for OCV hysteresis. Discrete Preisach models are often implemented without explicit orientation corrections, and weights are fitted only to a limited set of loops, which may result in an asymmetric weight distribution and can impair generalization as well as yield uncontrolled loop orientation. Using different weight sets for increasing and decreasing inputs is possible but conflicts with the Preisach concept. Most OCV-oriented Preisach models use a combined formulation $OCV = f(SOC, H)$ with an offset for OCV_{min} at $SOC = 0\,\%$; Everett-based variants achieve correct loop orientation [10,22,45], whereas discrete versions without correct loop orientation may fail outside the training dataset due to asymmetric weights or need additional compensation mechanisms [75,78–80]. Other applications include mappings with OCV as input and SOC as output [44], neural-network-based parameter estimation for major loop modeling using a classical Preisach model with predefined continuous weight functions [76], and linearly smoothed discrete variants for observers [77]. Given the importance of the Preisach model in literature and its high accuracy combined with a physically meaningful foundation, it is necessary to include the Preisach model in the benchmark of this work. However, to address the exposed limitations and ensure comparability with other approaches, this paper introduces a Modified Preisach model. For better comparability with other OCV hysteresis models, the OCV will be expressed in separated form as $OCV = OCV_{\mathrm{ref}} + H$. The model is parameterized as a discrete Preisach representation for multiple minor loops separately, and the Preisach triangle is modified to enforce clockwise, monotonically increasing loop orientation. Meaning, each minor loop is modeled separately instead of constructing a global additive $H(SOC)$, since such a function would violate the monotonicity of the Preisach model. A discrete implementation is chosen over the Everett formalism because the available measurements do not include FORCs.

Prandtl–Ishlinskii model. The Prandtl–Ishlinskii model is a switching-type hysteresis model, again originating from magnetization theory, using play operators with activation thresholds r for the input x. Activated operators follow a monotonic trajectory governed by x, linear in the baseline model and non-linear (e.g., polynomial) in generalized forms. The generalized variant allows different curves for increasing and decreasing inputs, enabling asymmetric hysteresis [23,90,91]. Conceptually, play operators are defined continuously for thresholds $0 \leq r \leq R$ and combined with a weight function p. The hysteretic response

is then obtained by integrating the weighted play operators over the threshold interval. In practice, the model is discretized into a finite sum of play operators with associated weights [23,90,91]. These models naturally produce counter-clockwise, monotonically increasing loops, whereas OCV hysteresis requires clockwise loops. This can be enforced by inverting the play operators and using negative weights [91], adding a memoryless correction term [90], overfitting the discrete model to selected loops [81–83], or swapping threshold signs for increasing and decreasing inputs, at the cost of slight discontinuities [23]. By shifting thresholds and play operator curves, the LFP OCV relation over its SOC can be approximated as $OCV = f(SOC, H)$, as by He et al. [23], where a generalized discrete model is combined with an ECM and analytically inverted to $SOC = f^{-1}(OCV, H)$ according to Al Janaideh et al. [91]. Other works use discrete generalized variants with polynomial play operators and Kalman filters or scenario-specific weight sets to fit major and minor loops [81–83], all yielding $OCV = f(SOC, H)$. Overall, the Prandtl–Ishlinskii model can represent major and minor OCV hysteresis loops. In principle, it could be reformulated into a separated form with $OCV = OCV_{\mathrm{ref}} + H$. Yet, this model requires extensive parameterization of weights p, play operator curves (e.g., polynomial coefficients a_i), and thresholds r. With linear play operators, a separated model would be similar to the linear Roscher-type approach. Due to its complexity and parameterization effort, the Prandtl–Ishlinskii model is not further investigated.

Jiles–Atherton model. The Jiles–Atherton model forms another class of hysteresis models applied to OCV hysteresis modeling. It is governed by a differential equation and yields a function $OCV = f(SOC, H)$ [24,84]. Both cited works focus on major loops only. Furthermore, the model parameters are defined in the context of magnetization, making their interpretation and transfer to OCV hysteresis non-trivial. Because of this parameter-mapping challenge and the focus on major loops alone, the Jiles–Atherton model is not considered further.

Takacs model. Windarko and Choi [85] apply the Takacs model to describe major OCV hysteresis in NiMH batteries. The model uses hyperbolic tangent functions and separately parameterizes charging and discharging branches. Although the authors state that minor loops can be described in principle, only major loops are analyzed. The model expresses OCV hysteresis as $OCV = f(SOC, H)$, where H simply indicates the branch. Zhao and de Callafon [25] extend the Takacs model to LFP graphite cells and use it in separated form $OCV = OCV_{\mathrm{ref}} + H$, where H is generated by the Takacs hysteresis model and fitted to various minor loop trajectories. Due to its limited presence in the OCV hysteresis modeling literature, its strong non-linearity, and the high parameterization effort for minor loops, the Takacs model is not further considered.

Other exponential OCV hysteresis models [26,27,92,93]. Beyond the Plett One-State and the Huria model, additional exponential hysteresis models exist. In Chin et al. [26] and Gallien and Brasseur [27], hysteresis is modeled similarly to the approaches by Plett [17] and Huria et al. [18], with exponential terms added to a reference OCV that directly describe minor loop trajectories. Zhang and Chow [92] divide the OCV curve into regions with either unique OCV trajectories, exponential behavior, or linear behavior, using coordinate transformations to fit major loop segments and to generate minor loops. The resulting model does not separate OCV and hysteresis and acts as a directly fitted combined OCV model. Eichi and Chow [93] propose a four-state system for major loops only, resulting in sums of exponential functions describing OCV_{ch} and OCV_{dch} without minor loop behavior. Due to their limited relevance and applicability, these exponential models are not considered further.

Other direct OCV hysteresis models [28,29,94,95]. Direct OCV hysteresis models specify OCV and OCV hysteresis in two principal ways. In Ding et al. [94] and Chang et al. [95], a single direct OCV is modeled as a weighted difference between OCV_{ch} and OCV_{dch} added to OCV_{dch}. Yang et al. [29] similarly introduce a separated model with $OCV = OCV_{\mathrm{ref}} + H$ for major loops, where hysteresis is given by a fixed difference between OCV_{ch} and OCV_{dch} and inductive effects from current fluctuations are embedded into H to improve SOC estimation under electromagnetic interference. In Schmitt et al. [28], minor loop trajectories are directly mapped into the OCV description for silicon-graphite anodes. Both classes of models can be interpreted as separate OCV hysteresis formulations. The first group, based on major loop reduction, is considered in this study. The second group is not, due to a lack of suitable experimental data for direct mapping of minor loops and the descriptive rather than model-based character of the approach.

Other linear and non-linear OCV hysteresis models [5,30]. Additional stand-alone empirical models can be identified beyond those in Table 4 and the direct or exponential models discussed above. These will not be included in the model comparison but are summarized here for completeness. In Nagode et al. [30], a mechanical analogy based on the Prandtl formalism is applied to model major and minor OCV hysteresis as piecewise linear trajectories, resulting in a finite-sum representation comparable to $OCV = f(SOC, H)$. Jahn et al. [5] present a semi-empirical approach integrating the many-particle model of Dreyer et al. [16] into an ECM framework. This leads to a formalism capable of describing major and minor loops in the form $OCV = f(SOC, H)$, where H encodes the state of multiple particle groups within the particle ensemble. Due to the non-separable nature of $OCV = f(SOC, H)$ in this model, the increased complexity, and the large number of parameters including parallel voltage sources, this physically meaningful model is not further investigated in this work.

Based on this in-depth analysis of relevant empirical OCV hysteresis models, the preselected models are adapted to the modeling framework developed in this work and then examined in detail, including their parameterization, in the subsequent section.

3.2. Analysis of empirical OCV hysteresis models and parameterization

This section considers all empirical models selected for this study, as listed in Table 4, along with additional direct OCV models based on major loop reduction. All other empirical models are excluded as they entail a high parameterization effort, excessive complexity, redundancy, or limited relevance in the literature.

Desired model composition and parameterization. A central objective of this work is model comparability, which requires a standardized model composition. This composition is also chosen to prepare the models for future investigations in combination with observers or filters, such as a simple EKF. For comparability and observer- and filter-readiness, model components should be separable to allow independent parameterization and analysis. Accordingly, the selected OCV hysteresis models must satisfy the framework introduced in Section 3.4. Meaning that, as mentioned earlier, all models represent OCV hysteresis holistically, including contributions from both graphite and LFP. OCV and OCV hysteresis must be implemented in a time-discrete form and, where applicable, in a separable way such that the hysteresis models only describe the transition between the major OCV loops and not the full OCV. Therefore, this characteristic has been already evaluated in the previous section. Moreover, OCV and hysteresis models are briefly evaluated regarding piecewise continuous differentiability with respect to model states. This model property is required in some observer or filter approaches due to model non-linearity and the need for linearization, as in EKF. The associated derivation of the corresponding Jacobians with respect to the model states, as well as further observer- and filter-related details for the overall model framework and for each OCV hysteresis model specifically, is beyond the scope of this work. Some of the models include their own reference OCVs. The combination of hysteresis models with an ECM derived in Section 3.3 is carried out in Section 3.4, which may involve exchanging the chosen reference OCV of the ECM according to the respective hysteresis model equations. In the following, all equations and variables are, for simplicity, expressed

directly in time-discrete form unless stated otherwise. The notation $\mathcal{X}_i$ denotes any variable $\mathcal{X}$ evaluated at time step t_i. Thus, the desired separated model composition of reference OCV and the additional hysteresis, $OCV = OCV_{\mathrm{ref}} + H$, known from the previous section is derived in a time-discrete manner for all hysteresis models in this section. These formulations may differ slightly depending on each model's definition of reference OCV and additional hysteresis.

For parameterization and analysis, the following notation is used consistently. All SOC values are defined as $SOC_i \in [0\,\%, 100\,\%]$. Rather than using H generically, we define $H(SOC_i, t_i) = H_i$, as already described in Section 2, as discrete hysteresis voltage in mV, defined as the difference between the modeled or measured OCV_i and $OCV_{i,\mathrm{dch}}$, and $H_{\max}(SOC_i) = H_{i,\max}$ as the maximum hysteresis voltage in mV, i.e. the difference between $OCV_{i,\mathrm{ch}}$ and $OCV_{i,\mathrm{dch}}$ at a given SOC:

$$H_i = OCV_i - OCV_{i,\mathrm{dch}} \tag{2}$$

$$H_{i,\max} = OCV_{i,\mathrm{ch}} - OCV_{i,\mathrm{dch}} \tag{3}$$

According to the holistic approach, both H_i and $H_{i,\max}$ include contributions from graphite and LFP. This influences the parameterization and validation of the hysteresis models, as these models depend on or scale with $H_{\max}$, which itself contains information from both graphite and LFP hysteresis. Based on these definitions, the normalized discrete hysteresis parameter $h(SOC_i, t_i) = h_i \in [0, 1]$, which is also already introduced in Section 2, is formulated:

$$h_i = \frac{OCV_i - OCV_{i,\mathrm{dch}}}{OCV_{i,\mathrm{ch}} - OCV_{i,\mathrm{dch}}} \tag{4}$$

This definition of h_i enables consistent comparison and parameterization of all OCV hysteresis models, even when their internal formulations differ and must be transformed into the form of Eq. (4). All models are discretely parameterized in terms of h_i, while their later simulation can follow each model's specific internal definition (see Section 3.4).

Model parameterization is based on minor OCV hysteresis loops extracted from the experimental data in Section 2.1. During parameterization of each minor loop, model parameters are assumed constant with respect to SOC, i.e., local behavior is represented around an average SOC:

$$SOC_{i,\mathrm{avg,loop}} = \frac{SOC_{i,\mathrm{max,loop}} + SOC_{i,\mathrm{min,loop}}}{2} \tag{5}$$

Since each minor loop includes one change in charge direction, parameters may be identified separately for charge and discharge. Across all minor loops, this yields parameter dependencies on SOC via $SOC_{i,\mathrm{avg,loop}}$ and, optionally, on charge direction. The feasible and required DOF for parameters varying with SOC and/or charge direction are specified for each model. The DOF is restricted according to the predefined requirements, in particular regarding continuity and differentiability, and are taken into account during parameterization and simulation. For each minor hysteresis loop and for each OCV hysteresis model, the following constrained non-linear least-squares problem is solved using Matlab's `fmincon` function:

$$S = \sum_{i=1}^{n_{\mathrm{loop}}} \left(h_{i,\mathrm{mod}} - h_{i,\mathrm{measured}}\right)^2 \tag{6}$$

The objective is to determine parameter values that minimize the squared error S between the n_{loop} measured normalized minor loop data points $h_{i,\mathrm{measured}}$ within the respective SOC window (see Section 2.1) and the corresponding normalized predictions $h_{i,\mathrm{mod}}$ computed via Eq. (4) for each model (see Table 5), while enforcing the non-linear constraint $h_{i,\mathrm{mod}} \in [0, 1]$. This constraint is considered during optimization using `fmincon`'s `nonlcon` interface. Mathematically, the constraint is collected in a stacked vector c during optimization and represents a set of values that must satisfy $c \leq 0$. For this purpose, the following two inequality constraint vectors c are used:

$$c_{i,1} = -h_{i,\mathrm{mod}} + \epsilon_{\mathrm{c}} \tag{7}$$

$$c_{i,2} = h_{i,\mathrm{mod}} - 1 + \epsilon_{\mathrm{c}} \tag{8}$$

With $\epsilon_{\mathrm{c}} = -0.05$, the constraint is relaxed to allow $h_{i,\mathrm{mod}} \in [-0.05, 1.05]$ for a normalized minor loop.

`fmincon` is applicable here because the constraints in Eqs. (7) and (8) act on the simulated model output $h_{i,\mathrm{mod}}$ rather than on the model parameters, and can therefore not be expressed as box or linear constraints. `fmincon` supports arbitrary non-linear constraints through its `nonlcon` interface and remains applicable across the full range of parameter dimensions occurring in this study, from models with a single parameter per charge direction to models described by a discrete weight distribution. Applying an identical problem formulation to all models ensures that the reported values of $\mathrm{MAE}_{\mathrm{fit}}$ are directly comparable and not influenced by differing solver or constraint settings. It should be noted that the constraints in Eqs. (7) and (8) are not strictly required for models that remain within the admissible range by construction as described subsequently. The constraints are nevertheless applied uniformly to all models to keep the problem formulation identical. This is consistent with the fact that only the models without such intrinsic limitation require an additional corrective term during later simulation.

Furthermore, `fmincon` is a local, gradient-based solver, while models may exhibit behavior that renders S (Eq. (6)) only piecewise smooth with respect to the model parameters. To confirm that the identified parameters do not depend on the solver or on its initialization, all minor loop fits were repeated with alternative optimization algorithms. The results are reported in Appendix F and confirm the parameter values given in Table 5.

In summary, the models are parameterized in time-discrete form and, where required, transformed to conform to the hysteresis factor $h_{i,\mathrm{mod}}$ in Eq. (4). The resulting hysteresis models can simulate behavior depending on SOC and charge direction, which will be considered, if applicable, in the subsequent parameterization process for each OCV hysteresis model. In the subsequent model framework, this dependence is represented via linear interpolation and clipping-based extrapolation of all model parameters for all models. Interpolation and extrapolation is referenced to the average SOC values $SOC_{i,\mathrm{avg,loop}}$ of the N_{loop} extracted minor loops (Section 2.1) and to the calculated SOC. If applicable, this inter- and extrapolation is combined with charge-direction-dependent parameter switching, thereby introducing an additional dependence relevant for differentiation in observer and filter applications. A dependence on temperature T and applied current I_{app} or C-Rate is not included in the OCV hysteresis models (see Section 2). Throughout this work, $I_{\mathrm{app}} > 0$ denotes charging currents and $I_{\mathrm{app}} < 0$ denotes discharging currents. Under these conditions, stationary OCV hysteresis behavior is assumed to vary only marginally (see Section 2 for details).

Table 5 summarizes the subsequently investigated aspects and corresponding results. The metric $\mathrm{MAE}_{\mathrm{fit}}$ characterizes the quality of the parameterization:

$$\mathrm{MAE}_{\mathrm{fit}} = \frac{1}{N_{\mathrm{loop}} \cdot n_{\mathrm{loop}}} \sum_{j=1}^{N_{\mathrm{loop}}} \sum_{i=1}^{n_{\mathrm{loop}}} \left|h_{i,\mathrm{mod}} - h_{i,\mathrm{measured}}\right|_j \tag{9}$$

Here, $N_{\mathrm{loop}} = 5$ minor loops with $n_{\mathrm{loop}} = 14$ data points each are evaluated, including both charge and discharge directions of the minor loops (see Section 2.1). The MAE is computed for $h_i \in [0, 1]$ and is intentionally chosen because it can be interpreted as a percentage deviation (mean absolute percentage error (MAPE)) by scaling with 100 % and is independent of the absolute magnitude of $H_{i,\max}$ in mV across the SOC range.

In addition, Table 5 reports for each model how and if it can be interpreted as a state variable and, thus, used for state estimation, as well as whether it is piecewise continuously differentiable with respect to model states (relevant for observer and filter applications). Furthermore, Table 5 assesses the models' drift tendency. To facilitate the subsequent differentiation of drift of individual models, the term is refined here.

Drift within OCV hysteresis models is either induced by higher order reversal curves (HORCs) or by interpolation. In the present context, HORC drift denotes the situation where hysteresis trajectories, starting from a FORC at $(SOC_{i,\mathrm{start}}, OCV_{i,\mathrm{start}})$ and reversing charge direction before reaching full saturation of the OCV hysteresis, return to $SOC_{i,\mathrm{start}}$ with $OCV_{i,\mathrm{end}} \neq OCV_{i,\mathrm{start}}$. In other words, this drift addresses whether minor loops from HORCs exhibit closed trajectories. This effect becomes especially relevant under frequent charge direction changes, such as recuperation found in automotive applications. The main reasons for this type of drift observed in OCV hysteresis models, which will be referred to as recuperation-induced drift, are non-linear model behavior and charge-direction-dependent model parameterization. Drift due to interpolation arises when parameters depend on SOC and are inter- or extrapolated. This type of drift is associated with parameter misfitting or overfitting combined with interpolation and is referred to as interpolation-induced drift. Note that the model parameters' charge direction dependency is associated with recuperation-induced drift, as this dependency only surfaces in conjunction with a change in charge direction. Both drifts can affect overall model quality and are identified in detail in Section 4. Based on these considerations, the phenomenon will be discussed in Section 5.

Furthermore, the models' discrete implementation can influence this behavior. However, this will not be explored further here, as it is inherent in all implementations. In conclusion, OCV hysteresis models can also exhibit drift-like behavior, depending on their model type, due to scaling with the maximum hysteresis $H_{\max}$ or due to the direct influence of the major OCV loops or of the maximum hysteresis $H_{\max}$ on the hysteresis trajectory itself. This behavior becomes apparent when the model is scaled by $H_{\max}$ or governed by $H_{\max}$, provided that $H_{\max}$ is not constant, since even linear behavior leads to an increasing or decreasing influence on the hysteresis trajectory. If the major OCV loops themselves govern the model, a monotonic behavior is required to suppress such behavior. It should be explicitly noted here that this behavior is not an unintended drift, but rather an intended model behavior.

Finally, the models will be analyzed regarding their minor loop asymmetry. Because all models are implemented in discrete form, these phenomena are analyzed only for their discrete versions. The governing equations reported in Table 5 emphasize model separation, discrete implementation, parameter fitting, and the dependence on SOC and charge direction. The results summarized in Table 5 are derived in the following. Table 5 thereby forms the second level of synthesis of this work: the governing equations, the identified model parameters, the resulting fit quality, and the mathematical properties listed above are collected in a single comparative view, so that the model-specific derivations that follow can be consulted selectively. These derivations are performed individually because the properties in question, and the drift tendency in particular, cannot be postulated but must be traced back to the respective model formulation before they can be identified in the simulation results in Sections 4 and 5.

Direct OCV model. The direct OCV model is described in the previous section based on Chang et al. [95] and Ding et al. [94]. It can be expressed in discrete terms using an auxiliary variable θ as follows:

$$OCV_{i,\mathrm{direct}} = OCV_{i,\mathrm{dch}} + \theta\, H_{i,\max} \tag{10}$$

The basic idea is to select a suitable constant factor θ for a given application. In this work, the following cases are considered: $\theta = 0$, $\theta = 0.5$, and $\theta = 1$, corresponding to operation on OCV_{dch}, OCV_{avg}, or OCV_{ch}, respectively. The parameter θ is bounded in $[0, 1]$ and has no further conditions or dependencies. Because this model uses the measured OCVs directly, no $\mathrm{MAE}_{\mathrm{fit}}$ is defined, and there are no continuity or differentiability properties beyond those of the OCV itself (see Sections 3.3 and 3.4). Loop asymmetry, drift tendency, and a state-variable interpretation are not applicable. For comparison and analysis, transformation into the normalized $h_{i,\mathrm{direct}}$ via Eq. (4) is straightforward and yields $h_{i,\mathrm{direct}} = \theta$.

Plett zero-state model. The Plett Zero-State model can be seen as an extension of the direct OCV model. In Plett [17] it is defined in discrete terms as:

$$OCV_{i,\mathrm{plett0}} = OCV_{i,\mathrm{avg}} + s_i\, \frac{1}{2}\, H_{i,\max} \tag{11}$$

$$s_i = \begin{cases} 1, & I_{i,\mathrm{app}} > \epsilon_{\mathrm{ch}}, \\ -1, & I_{i,\mathrm{app}} < \epsilon_{\mathrm{dch}}, \\ s_{i-1}, & \text{else}. \end{cases} \tag{12}$$

Thus, the model switches between OCVs depending on charge direction: OCV_{ch} for charging ($I_{i,\mathrm{app}} > 0$), OCV_{dch} for discharging ($I_{i,\mathrm{app}} < 0$), and the previously selected OCV when $I_{i,\mathrm{app}} \approx 0$. To avoid incorrect switching caused by measurement noise and weak recuperation pulses, a stabilization margin ϵ_{ch} and ϵ_{dch} is introduced. Since there is no strict bound on ϵ_{ch} and ϵ_{dch}, they are set to $\epsilon_{\mathrm{ch}} = 1.0\,\mathrm{A}$ and $\epsilon_{\mathrm{dch}} = -0.05\,\mathrm{A}$ in this work to increase stability under net discharge. For easier integration into the ECM (Sections 3.3 and 3.4), an equivalent formulation is used:

$$OCV_{i,\mathrm{plett0}} = \begin{cases} OCV_{i,\mathrm{ch}}, & I_{i,\mathrm{app}} > \epsilon_{\mathrm{ch}}, \\ OCV_{i,\mathrm{dch}}, & I_{i,\mathrm{app}} < \epsilon_{\mathrm{dch}}, \\ OCV_{i-1,\mathrm{plett0}}, & \text{else}. \end{cases} \tag{13}$$

As with the direct OCV model, this pure switching between major OCV loops implies that no $\mathrm{MAE}_{\mathrm{fit}}$ is defined, and continuity and differentiability beyond the major OCV loops themselves do not need to be taken into account. Loop asymmetry, drift tendency, and a state-variable interpretation are likewise not applicable. For comparability, transformation into the normalized $h_{i,\mathrm{plett0}}$ via Eq. (4) leads to $h_{i,\mathrm{plett0}} = 0$ or $h_{i,\mathrm{plett0}} = 1$ depending on charge direction.

Plett One-State model. The Plett One-State model is derived from the following time-continuous differential equation [17]:

$$\frac{\mathrm{d}h_{\mathrm{plett1,lit}}(SOC(t),t)}{\mathrm{d}SOC(t)} = \mathrm{sgn}(I_{\mathrm{app}}(t))\,\gamma(SOC(t)) \left(\mathrm{sgn}(I_{\mathrm{app}}(t))\,\frac{1}{2}\,H_{\max}(SOC(t)) - h_{\mathrm{plett1,lit}}(SOC(t),t)\right) \tag{14}$$

With

$$h_{\mathrm{plett1,lit}}(SOC(t),t) = OCV_{\mathrm{plett1}}(SOC(t),t) - OCV_{\mathrm{avg}}(SOC(t)), \tag{15}$$

where $h_{\mathrm{plett1,lit}}(SOC(t),t)$ denotes the hysteresis factor in its original definition from literature and $\gamma(SOC(t))$ the transition speed between OCV_{dch} and OCV_{ch}. The OCV hysteresis model in Eq. (14) is first rewritten to depend on the applied current $I_{\mathrm{app}}(t)$ by substituting

$$\frac{\mathrm{d}SOC(t)}{\mathrm{d}t} = \frac{\eta_{\mathrm{coul}}\, I_{\mathrm{app}}(t)}{C_{\mathrm{n}}} \cdot 100, \tag{16}$$

with η_{coul} being the coulombic efficiency and C_{n} the nominal capacity in Ah. Solving and discretizing the differential equation leads to [17]:

$$h_{i+1,\mathrm{plett1,lit}} = \exp\left(-\left|\frac{\gamma_i\,\eta_{\mathrm{coul}}\,I_{i,\mathrm{app}}\,\Delta t\cdot 100}{C_{\mathrm{n}}}\right|\right) h_{i,\mathrm{plett1,lit}} + \left(1 - \exp\left(-\left|\frac{\gamma_i\,\eta_{\mathrm{coul}}\,I_{i,\mathrm{app}}\,\Delta t\cdot 100}{C_{\mathrm{n}}}\right|\right)\right) \mathrm{sgn}(I_{i,\mathrm{app}})\,\frac{1}{2}\,H_{i,\max} \tag{17}$$

For compactness, we define:

$$p(\gamma_i, I_{i,\mathrm{app}}) = \exp\left(-\left|\frac{\gamma_i\,\eta_{\mathrm{coul}}\,I_{i,\mathrm{app}}\,\Delta t\cdot 100}{C_{\mathrm{n}}}\right|\right) \tag{18}$$

Table 5
Model formulation and mathematical properties of the empirical OCV hysteresis models under investigation, condensed into a single comparative view. Each model is given in its native formulation; the transformation to $h_{i,\mathrm{mod}}$ follows the model definition and Eq. (4).

	Model formulation			Mathematical properties			
	Governing equations	Parameters	$\mathrm{MAE}_{\mathrm{fit}}$ / –	Continuity, differentiation	State variable	Drift tendency	Loop asymmetry
Direct OCV	$OCV_{i,\mathrm{direct}} = OCV_{i,\mathrm{dch}} + \theta\, H_{i,\max}$	$\theta \in [0,1]$[e]	–	–	–	–	–
Plett Zero-State	$OCV_{i,\mathrm{plett0}} = OCV_{i,\mathrm{avg}} + s_i\, \frac{1}{2}\, H_{i,\max}$	$\epsilon_{\mathrm{ch}} > 0\,\mathrm{A}$[e] $\epsilon_{\mathrm{dch}} < 0\,\mathrm{A}$[e]	–	–	–	–	–
Plett One-State	$h_{i+1,\mathrm{plett1,lit}} = p(\gamma_i, I_{i,\mathrm{app}})\, h_{i,\mathrm{plett1,lit}} + \left(1 - p(\gamma_i, I_{i,\mathrm{app}})\right) \mathrm{sgn}(I_{i,\mathrm{app}})\, \frac{1}{2}\, H_{i,\max}$[a]	$\gamma_{i,\mathrm{ch}} \in [0,1]$ $\gamma_{i,\mathrm{dch}} \in [0,1]$	0.065	piecewise continuous differentiability applicable	✓	✓	✓
Huria	$OCV_{i+1,\mathrm{huria}} = OCV_{i,\mathrm{huria}} + \Delta OCV_{i,\mathrm{huria}}$[b]	$k_{i,\mathrm{ch}} \in [0,1]$ $k_{i,\mathrm{dch}} \in [0,1]$	0.054	piecewise continuous differentiability applicable	✗	✓	✓
Roscher	$h_{i+1,\mathrm{roscher}} = v_{i,1} \cdot \psi_{i+1,1} + (1 - v_{i,1}) \cdot \psi_{i+1,2}$[c]	$v_{i,1} \in [0,1]$ $m_{i,\mathrm{ch},1} \geq 0$ $m_{i,\mathrm{ch},2} \geq 0$ $m_{i,\mathrm{dch},1} \geq 0$ $m_{i,\mathrm{dch},2} \geq 0$	0.031	piecewise continuous differentiability applicable	✗	✗	✓
Modified Preisach	$h_{i,\mathrm{preisach,lit}} = \sum_{\hat{\imath}=1}^{N_\alpha} \sum_{\hat{\jmath}=1}^{N_\beta} \mu_{i,\alpha_{\hat{\imath}},\beta_{\hat{\jmath}}} \cdot \zeta_{i,\alpha_{\hat{\imath}},\beta_{\hat{\jmath}}}$[d]	$\mu_{i,\alpha_{\hat{\imath}},\beta_{\hat{\jmath}}} \in [0,1]$ $\zeta_{i,\alpha_{\hat{\imath}},\beta_{\hat{\jmath}}} \in \{-1,1\}$ $\alpha_{\max} \geq 0$[e] $N_\alpha \geq 0$[e] $\beta_{\max} \geq 0$[e] $N_\beta \geq 0$[e] $\epsilon_{\mathrm{preisach}} \geq 0$[e]	0.063	piecewise continuous differentiability applicable, non-defined derivatives while switching	✗	✓	✓

[a] With $p(\gamma_i, I_{i,\mathrm{app}})$ from Eq. (16).
[b] With $\Delta OCV_{i,\mathrm{huria}}$ from Eqs. (28) and (29).
[c] With $\psi_{i+1,1}$ and $\psi_{i+1,2}$ from Eqs. (31) and (32).
[d] With $\zeta_{i,\alpha_{\hat{\imath}},\beta_{\hat{\jmath}}}$ from Eqs. (48), (50) and (52).
[e] Fixed model settings.

The transition speed γ_i is discretized for the $N_{\mathrm{loop}} = 5$ minor loops from Section 2.1, using the corresponding $SOC_{i,\mathrm{avg,loop}}$. Since γ_i only affects the slope of the transition, it can be parameterized separately for charge and discharge, resulting in $\gamma_{i,\mathrm{ch}}$ and $\gamma_{i,\mathrm{dch}}$. Variations in transition slope over SOC and charge direction can introduce points of non-differentiability in simulated trajectories, and thus discontinuities in the derivative. Although discontinuities may occur, particularly beside the parameter-dependent ones, when the charge direction and, thus the overall trajectory changes, the criterion of piecewise continuous differentiability is not violated. The coulombic efficiency η_{coul} is assumed to be 1. The Plett One-State model treats OCV hysteresis as a separate state $h_{i,\mathrm{plett1,lit}}$:

$$OCV_{i+1,\mathrm{plett1}} = OCV_{i+1,\mathrm{avg}} + h_{i+1,\mathrm{plett1,lit}} \tag{19}$$

Finally, recuperation and interpolation-induced drift will be examined. Due to the non-linear, charge-direction-dependent behavior of the Plett One-State model, which converges towards the major loops, any change in charge direction can cause recuperation-induced drift. First, local slopes depend on the distance to the corresponding major loop, expressed through $H_{\max}/2$ in Eq. (14), which introduces the non-linearity. For example, near OCV_{dch}, slopes are small in discharge direction and large in charge direction, so small recuperation pulses may generate drift. Secondly, the associated charge-direction-dependent nature of the parameterization may further amplify the drift that is already present with frequent recuperation due to the non-linearity itself, as it introduces additional changes in the hysteresis slopes. On the other hand, interpolation-induced drift arises from the SOC-dependent parameterization used, which may be apparent with continuous load or during net discharging. Furthermore, since the model is governed by $H_{\max}/2$, the non-monotonic behavior of $H_{\max}$ arising from the holistic OCV hysteresis representation of LFP and graphite, particularly due to graphite staging, can cause the hysteresis trajectory to exhibit pronounced drift-like behavior in addition to interpolation- and recuperation-induced drift. However, this is not a drift but rather an intentional model property. The magnitude of these effects and their impact on overall model quality, along with comparisons to other models, are analyzed in Sections 4 and 5. Additional model properties (time forwarding, loop asymmetry, and parameterization) reported in Table 5 are derived in Appendix B.

In summary, the discrete Plett One-State model in Eq. (17), which is interpreted as a state variable, is consistently parameterized and analyzed via the normalized hysteresis factor $h_{i,\mathrm{plett1}}$ according to Eq. (4) instead of the literature definition $h_{i,\mathrm{plett1,lit}}$. Simulation is carried out using the model-specific OCV hysteresis formulation with $h_{i,\mathrm{plett1,lit}}$, combined with the ECM (see Sections 3.3 and 3.4).

Huria model. The model proposed by Huria et al. [18] is specified by the following time-continuous differential equations:

$$\left.\frac{\mathrm{d}OCV_{\mathrm{huria}}(SOC(t),t)}{\mathrm{d}SOC(t)}\right|_{\frac{\mathrm{d}SOC(t)}{\mathrm{d}t} \geq 0} = \frac{\mathrm{d}OCV_{\mathrm{ch}}(SOC(t))}{\mathrm{d}SOC(t)} + k(SOC(t))\, \left[OCV_{\mathrm{ch}}(SOC(t)) - OCV_{\mathrm{huria}}(SOC(t),t)\right] \tag{20}$$

$$\left.\frac{\mathrm{d}OCV_{\mathrm{huria}}(SOC(t),t)}{\mathrm{d}SOC(t)}\right|_{\frac{\mathrm{d}SOC(t)}{\mathrm{d}t} \leq 0} = \frac{\mathrm{d}OCV_{\mathrm{dch}}(SOC(t))}{\mathrm{d}SOC(t)} + k(SOC(t))\, \left[OCV_{\mathrm{dch}}(SOC(t)) - OCV_{\mathrm{huria}}(SOC(t),t)\right] \tag{21}$$

The applicable equation is selected by the sign of $\mathrm{d}SOC/\mathrm{d}t$, i.e. the charge direction. As in the Plett One-State model, $k(SOC(t))$ describes the transition speed between OCV_{dch} and OCV_{ch}. The major loops govern the hysteresis behavior depending on charge direction. The

structure of Eqs. (20) and (21) also leads to exponential trajectories when solved analytically, similar to the Plett One-State model; the differences between both models are highlighted in Appendix C. Unlike the Plett One-State model, the Huria model does not treat OCV hysteresis as a state variable. The derivative with respect to SOC is therefore only partially substituted by Eq. (16) as the model equations do not need to be independent of other states.

A time-discrete solution is now derived. For the first term on the right-hand side of Eqs. (20) and (21), if $SOC_i - SOC_{i-1} \neq 0\,\%$, we use backward differences:

$$\frac{\mathrm{d}OCV_{i,\mathrm{ch}}}{\mathrm{d}SOC_i} = \frac{OCV_{i,\mathrm{ch}} - OCV_{i-1,\mathrm{ch}}}{SOC_i - SOC_{i-1}} \tag{22}$$

$$\frac{\mathrm{d}OCV_{i,\mathrm{dch}}}{\mathrm{d}SOC_i} = \frac{OCV_{i,\mathrm{dch}} - OCV_{i-1,\mathrm{dch}}}{SOC_i - SOC_{i-1}} \tag{23}$$

For $SOC_i - SOC_{i-1} = 0\,\%$, the slopes of the major loops use:

$$\frac{\mathrm{d}OCV_{i,\mathrm{ch}}}{\mathrm{d}SOC_i} = \frac{\mathrm{d}OCV_{i,\mathrm{dch}}}{\mathrm{d}SOC_i} = 0 \tag{24}$$

The backward difference scheme uses steps i and $i-1$ to approximate the slope at i, avoiding any dependence on a predicted SOC_{i+1} and OCV_{i+1} values. With sufficiently small Δt, this approximation is adequate. The second term in Eqs. (20) and (21) only requires discretization in time. The fully discrete derivatives are therefore:

$$\left.\frac{\mathrm{d}OCV_{i,\mathrm{huria}}}{\mathrm{d}SOC_i}\right|_{\mathrm{ch}} = \frac{\mathrm{d}OCV_{i,\mathrm{ch}}}{\mathrm{d}SOC_i} + k_{i,\mathrm{ch}}\left(\left|OCV_{i,\mathrm{ch}} - OCV_{i,\mathrm{huria}}\right|\right) \tag{25}$$

$$\left.\frac{\mathrm{d}OCV_{i,\mathrm{huria}}}{\mathrm{d}SOC_i}\right|_{\mathrm{dch}} = \frac{\mathrm{d}OCV_{i,\mathrm{dch}}}{\mathrm{d}SOC_i} + k_{i,\mathrm{dch}}\left(\left|OCV_{i,\mathrm{dch}} - OCV_{i,\mathrm{huria}}\right|\right) \tag{26}$$

Here, $OCV_{i,\mathrm{huria}}$ denotes the OCV including hysteresis. As k_i represents the transition speed between the major loops, it is again discretized by $k_{i,\mathrm{ch}}$ and $k_{i,\mathrm{dch}}$ over the $N_{\mathrm{loop}} = 5$ minor loops using $SOC_{i,\mathrm{avg,loop}}$, analogous to the Plett One-State model. As before, SOC- and charge-direction-dependent k_i's can result points of non-differentiability and thus, derivative discontinuities. Besides the parameter-dependent discontinuities, derivative discontinuities occur with changes in charge direction as the overall trajectory changes. Yet, the model remains piecewise continuously differentiable. Absolute OCV differences in Eqs. (25) and (26) ensure k_i remains positive irrespective of charge direction.

Combining Eqs. (25) and (26) with Eq. (16) and applying a forward Euler step results in $OCV_{i+1,\mathrm{huria}}$:

$$OCV_{i+1,\mathrm{huria}} = OCV_{i,\mathrm{huria}} + \Delta OCV_{i,\mathrm{huria}} \tag{27}$$

$$\Delta OCV_{i,\mathrm{ch,huria}} = \left.\frac{\mathrm{d}OCV_{i,\mathrm{huria}}}{\mathrm{d}SOC_i}\right|_{\mathrm{ch}} \cdot \frac{I_{i,\mathrm{app}}\,\Delta t \cdot 100}{C_{\mathrm{n}}} \tag{28}$$

$$\Delta OCV_{i,\mathrm{dch,huria}} = \left.\frac{\mathrm{d}OCV_{i,\mathrm{huria}}}{\mathrm{d}SOC_i}\right|_{\mathrm{dch}} \cdot \frac{I_{i,\mathrm{app}}\,\Delta t \cdot 100}{C_{\mathrm{n}}} \tag{29}$$

Yet again, the coulombic efficiency η_{coul} in Eq. (16) is assumed to be 1, and therefore neglected in Eqs. (28) and (29). This discrete model, based on Huria et al. [18], must be initialized with a two-step history to allow evaluation at $i-1$ for predicting $i+1$.

In contrast to the Plett One-State model, the Huria implementation does not rely on an additional reference OCV; instead, $OCV_{i,\mathrm{huria}}$ directly replaces the reference OCV in the ECM (see Sections 3.3 and 3.4). If, for instance, $\left|OCV_{i,\mathrm{ch}} - OCV_{i,\mathrm{huria}}\right| = 0$, then $OCV_{i+1,\mathrm{huria}}$ is solely determined by the slope of $OCV_{i,\mathrm{ch}}$ (see Eq. (25)), meaning the major loops are intrinsically embedded in the model via the forward-Euler integration in Eqs. (27), (28), and (29).

The pattern for recuperation and interpolation-induced drift is similar to that of the Plett One-State model. Due to the non-linear, charge-direction-dependent behavior, the Huria model exhibits interpolation-induced drift. Again, the non-linear behavior is expressed through the distance to the corresponding major loop, which governs the OCV hysteresis (see Eqs. (20) and (21)). The associated charge-direction-dependent nature of the parameterization may further amplify this drift. Yet again, interpolation-induced drift arises from the SOC-dependent parameterization used. In contrast to the Plett One-State model, this model is directly governed by the major OCV loops rather than H_{max}, which contains the holistic OCV hysteresis representation of LFP and graphite. As described earlier, with both major loops exhibiting monotonic behavior, no drift-like behavior is expected due to the model formulation itself. The magnitude of these effects and their impact on overall model quality, along with comparisons to other models, are analyzed in Sections 4 and 5. Additional model properties (time forwarding, loop asymmetry, and parameterization) reported in Table 5 and the comparison with the Plett One-State model are provided in Appendix C.

In conclusion, the discrete Huria model, as defined in Eq. (27), is parameterized and analyzed systematically using the normalized hysteresis factor $h_{i,\mathrm{huria}}$, which can be derived from $OCV_{i,\mathrm{huria}}$ based on Eq. (4). Simulation uses the model-specific OCV definition, which inherently includes both major loops and OCV hysteresis. In Section 3.4, the reference OCV in the exemplary output equation of the ECM (Section 3.3) is therefore replaced by the OCV of the Huria model.

Roscher model. The model introduced by Roscher and Sauer [19] describes OCV hysteresis via two integral equations instead of differential equations with transition-speed parameters. The definition in literature directly employs the normalized hysteresis factor $h_{i,\mathrm{roscher}}$ from Eq. (4) making no transformation for parameterization and subsequent analysis necessary. The discretized model formulation reads:

$$h_{i+1,\mathrm{roscher}} = \upsilon_{i,1} \cdot \psi_{i+1,1} + (1 - \upsilon_{i,1}) \cdot \psi_{i+1,2} \tag{30}$$

The parameters $\upsilon_{i,1}$ and $\upsilon_{i,2}$ are weighting factors with $\sum \upsilon_{i,j} = 1$, so $\upsilon_{i,2} = 1 - \upsilon_{i,1}$, whereas $\psi_{i+1,1}$ and $\psi_{i+1,2}$ are defined as:

$$\psi_{i+1,1} = \min\left(\max\left(\psi_{i,1} + m_{i,1} \cdot \frac{I_{i,\mathrm{app}}\,\Delta t \cdot 100}{C_{\mathrm{n}}}, 0\right), 1\right) \tag{31}$$

$$\psi_{i+1,2} = \min\left(\max\left(\psi_{i,2} + m_{i,2} \cdot \frac{I_{i,\mathrm{app}}\,\Delta t \cdot 100}{C_{\mathrm{n}}}, 0\right), 1\right) \tag{32}$$

The parameters $m_{i,1}$ and $m_{i,2}$ represent the slopes of the two linear charge-throughput-dependent model contributions. The discretized integral formulation is already consistent with the SOC convention adopted in this work. Consequently, the coulombic efficiency η_{coul} is also set to 1 here. Due to the linear nature of the Roscher model, a saturation of the integrals, as described in the equations above, is required. This saturation is considered in the parameterization process as well as during simulation.

For this model, the parameters $\upsilon_{i,1}$, $m_{i,1}$, and $m_{i,2}$ are discretized for the $N_{\mathrm{loop}} = 5$ minor loops from Section 2.1, using $SOC_{i,\mathrm{avg,loop}}$. The available DOF must fulfill piecewise continuous differentiability of $h_{i,\mathrm{roscher}}$, i.e., avoid discontinuities in itself. This yields the SOC- and charge-direction-dependent parameters $\upsilon_{i,1}$, $m_{i,\mathrm{ch},1}$, $m_{i,\mathrm{dch},1}$, $m_{i,\mathrm{ch},2}$, and $m_{i,\mathrm{dch},2}$. By enforcing $\upsilon_{i,1}$ (and thus $\upsilon_{i,2} = 1 - \upsilon_{i,1}$) to be independent of charge direction, a change in direction does not instantly alter $h_{i,\mathrm{roscher}}$, but only affects the evolution of ψ_1 and ψ_2 via their slopes. Variations of the slopes m_i over SOC and charge direction and of $\upsilon_{i,1}$ over SOC may generate points of non-differentiability in the OCV hysteresis trajectories. Besides parameterization, reaching saturation and changes in charge direction alter the overall OCV hysteresis trajectory, so there is a discontinuity in the derivative, as these points are non-differentiable. Nevertheless, the criterion of piecewise continuous differentiability is satisfied.

The separation between reference OCV and OCV hysteresis is explicit, and the combination with OCV_{dch} is carried out in Section 3.4. With Eqs. (4) and (30), the overall discrete OCV is:

$$OCV_{i+1,\mathrm{roscher}} = OCV_{i+1,\mathrm{dch}} + h_{i+1,\mathrm{roscher}} \cdot H_{i+1,\mathrm{max}} \tag{33}$$

As with the Huria model, hysteresis here is not treated as a state variable, and the model does not need to be independent of other states.

Recuperation and interpolation-induced drift in the Roscher model behave differently. Due to its linearity, only the charge-direction-dependent behavior of its parameterization may introduce recuperation-induced drift. The linear nature technically allows to describe any minor loop from HORCs as closed loop trajectory by using a charge-direction-independent parameterization. Besides that, interpolation-induced drift arises from the SOC-dependent parameterization used. In contrast to the previous models, as the Roscher model deploys the normalized hysteresis $h_{i,\mathrm{roscher}}$, it is only scaled by $H_{\max}$. As stated, $H_{\max}$ exhibits non-monotonic behavior due to the holistic OCV hysteresis representation of LFP and graphite. Subsequently, the Roscher model also may exhibit, in addition to the interpolation- and recuperation-induced drift, a meaningful, yet drift-like hysteresis trajectory that follows the trajectory of $H_{\max}$. The magnitude of these effects and their impact on overall model quality, along with comparisons to other models, are analyzed in Sections 4 and 5. Additional model properties (time forwarding, loop asymmetry, and parameterization) reported in Table 5 are provided in Appendix D.

In conclusion, the discrete Roscher model in Eq. (30) is consistently parameterized and analyzed using the normalized $h_{i,\mathrm{roscher}}$, by model definition, aligned with Eq. (4). Simulation also uses this normalized hysteresis definition. In Section 3.4, the reference OCV in the exemplary output equation of the ECM (Section 3.3) is replaced by OCV_{dch} in combination with the Roscher model.

Modified Preisach model. The general working principle of the Preisach hysteresis model and its established applications to OCV hysteresis have been discussed in Section 3.1. Building on this foundation, a modified Preisach model is proposed that addresses specific shortcomings of previous implementations. For improved comparability, the model is formulated in separated form, i.e. $OCV = OCV_{\mathrm{ref}} + H$, and discretely parameterized using measured minor OCV hysteresis loops. This approach ensures a clockwise, monotonically increasing loop orientation by modifying the Preisach triangle. A discrete Preisach implementation is chosen over the Everett formalism because the measurement procedure in this work does not provide FORCs. Further background and a literature discussion are given in Section 3.1.

The already spatial- and time-discretized Preisach output equation of the modified OCV hysteresis model is adapted from An and Cai [88]:

$$h_{i,\mathrm{preisach,lit}} = \sum_{\hat{i}=1}^{N_\alpha} \sum_{\hat{j}=1}^{N_\beta} \mu_{i,\alpha_{\hat{i}},\beta_{\hat{j}}} \cdot \zeta_{i,\alpha_{\hat{i}},\beta_{\hat{j}}} \tag{34}$$

As in the classical Preisach model from Mayergoyz [87], $h_{i,\mathrm{preisach,lit}} \in [-1, 1]$ is the hysteresis factor, $\mu_{i,\alpha_{\hat{i}},\beta_{\hat{j}}}$ are discrete weights, and $\zeta_{i,\alpha_{\hat{i}},\beta_{\hat{j}}} \in \{-1, 1\}$ are the corresponding hysterons. In Section 3.4, the resulting overall OCV is formed by combining this hysteresis factor with OCV_{dch} and substituting it for the reference OCV in the ECM from Section 3.3. For parameterization and analysis, the model is transformed to $h_{i,\mathrm{preisach}}$ based on Eq. (4) instead of using $h_{i,\mathrm{preisach,lit}}$. In the subsequent simulations, the literature definition $h_{i,\mathrm{preisach,lit}}$ from Eq. (34) is used directly (see Section 3.4). Generally, this formulation provides a clear separation between reference OCV and OCV hysteresis.

Weights and hysterons are defined on the Preisach plane at discrete coordinates $(\alpha_{\hat{i}}, \beta_{\hat{j}})$. The weights are non-negative and normalized,

$$\sum_{\hat{i}=1}^{N_\alpha} \sum_{\hat{j}=1}^{N_\beta} \mu_{i,\alpha_{\hat{i}},\beta_{\hat{j}}} = 1, \tag{35}$$

which results in $h_{i,\mathrm{preisach,lit}} = -1$ and $h_{i,\mathrm{preisach,lit}} = 1$ when all hysterons are in state -1 or 1, respectively.

Starting from Eq. (34), modifications are introduced to obtain a simple, discrete model with clockwise, monotonically increasing minor loops. The coordinates $\alpha_{\hat{i}}$ and $\beta_{\hat{j}}$ are defined as

$$\alpha_{\hat{i}} = \frac{\alpha_{\max}}{N_\alpha - 1} \cdot (\hat{i} - 1), \quad \text{for } \hat{i} = 1, 2, \ldots, N_\alpha, \tag{36}$$

$$\beta_{\hat{j}} = \frac{\beta_{\max}}{N_\beta - 1} \cdot (\hat{j} - 1), \quad \text{for } \hat{j} = 1, 2, \ldots, N_\beta, \tag{37}$$

which are the discrete coordinates of weights and hysterons. $\alpha_{\max}$ and $\beta_{\max}$ denote the saturation maxima along the two axes describing the Preisach plane. For this model, the maximum of both axes is restricted to $\Delta x_{\max} = \alpha_{\max} = \beta_{\max}$. N_α and N_β denote the number of discretization points per axis, thus specifying the model's DOF. The indices $\hat{i}$ and $\hat{j}$ map the positions on the discrete plane to $\mu_{i,\alpha_{\hat{i}},\beta_{\hat{j}}}$ and $\zeta_{i,\alpha_{\hat{i}},\beta_{\hat{j}}}$. As follows, the coordinates for the Preisach plane (α, β) have a range $\alpha \in [0, \Delta x_{\max}]$ and $\beta \in [0, \Delta x_{\max}]$. Hence, transformation between input x (later SOC_i) and (α, β) is required.

The key modification concerns the Preisach triangle $\mathcal{T}$ within the Preisach plane, which is defined in a "flipped" way:

$$\mathcal{T} = \left[(\alpha, \beta) \mid \beta \geq \alpha,\ \alpha \leq \Delta x_{\max},\ \beta \leq \Delta x_{\max} \right] \tag{38}$$

Consider a state where all discrete hysterons initially satisfy $\zeta_{i,\alpha_{\hat{i}},\beta_{\hat{j}}} = -1$ for all $\hat{i}, \hat{j}$. With increasing input x, mapped to an increasing α, all hysterons fulfilling $\alpha > \alpha_{\hat{i}}$ switch from -1 to 1 when their threshold is exceeded. Due to $\beta \geq \alpha$, crossing the first threshold at $\hat{i} = 1$ switches all N_β hysterons along the line $\alpha_{\hat{i}=1}$ inside $\mathcal{T}$, i.e. $\zeta_{i,\alpha_{\hat{i}=1},\beta_{\hat{j}}} = 1$. As α increases towards $\alpha_{\max}$, the region $\beta \geq \alpha$ shrinks, so fewer hysterons switch at each subsequent threshold $\alpha_{\hat{i}}$. Similarly, starting from $\zeta_{i,\alpha_{\hat{i}},\beta_{\hat{j}}} = 1$ for all $\hat{i}, \hat{j}$ and decreasing the input x (mapped to decreasing β), all hysterons fulfilling $\beta \leq \beta_{\hat{j}}$ switch from 1 to -1 when crossing the thresholds $\beta_{\hat{j}}$, again with the number of switching hysterons, which reduces with decreasing β, determined by the geometry of $\mathcal{T}$.

This switching behavior, combined with constant weights $\mu_{i,\alpha_{\hat{i}},\beta_{\hat{j}}}$, produces the desired discrete, monotonically increasing, clockwise hysteresis loops of the Modified Preisach model. At the same time, it confirms the need for input transformations from x to (α, β) and for reset mechanisms that account for whether the input is increasing or decreasing and whether α or β exceed their maxima $\alpha_{\max}$ and $\beta_{\max}$ (i.e., $\Delta x_{\max}$). The resets are necessary to maintain comparability with an additive OCV hysteresis term that separately covers multiple minor loops during parameterization, followed by simulations over the whole SOC range with interpolated and extrapolated parameters.

The continuous variables x, α, and β used for the description of the Preisach triangle and the switching behavior are now replaced by discrete x_i, α_i, and β_i, because the model operates in discrete time. The following initialization and transformations are used for parameterization and simulation. Therefore, hysteresis evaluation begins at $i = 2$:

$$h_{1,\mathrm{preisach,lit}} = \left(\frac{OCV_{1,\mathrm{preisach}} - OCV_{1,\mathrm{dch}}}{OCV_{1,\mathrm{ch}} - OCV_{1,\mathrm{dch}}} \cdot 2 \right) - 1 \tag{39}$$

The model must be initialized with $h_{1,\mathrm{preisach,lit}} \in \{-1, 1\}$ to ensure a well-defined initial state for all hysterons:

$$\zeta_{1,\alpha_{\hat{i}},\beta_{\hat{j}}} = h_{1,\mathrm{preisach,lit}} \quad \forall \hat{i}, \hat{j} \tag{40}$$

A saturation marker Δx_i is introduced to support transforming and resetting x_i to depict α_i and β_i correctly. Δx_1 is initially defined as:

$$\Delta x_1 = -x_1 + \left(\frac{1 + h_{1,\mathrm{preisach,lit}}}{2} \Delta x_{\max} \right) \tag{41}$$

Likewise, the reset variables $\Delta x_{i,\mathrm{reset,ch}}$ and $\Delta x_{i,\mathrm{reset,dch}}$ are introduced to depict α_i and β_i correctly. They are initialized as:

$$\Delta x_{1,\mathrm{reset,ch}} = \Delta x_{1,\mathrm{reset,dch}} = 0 \tag{42}$$

Finally, $x_{i,\mathrm{prev}}$ is introduced. It is necessary, within the transformation and reset process, to consider a switching threshold $\epsilon_{\mathrm{preisach}}$ for model stabilization, as it stores the last input x_i used for hysteresis updates. It is initialized as:

$$x_{1,\mathrm{prev}} = x_1 \tag{43}$$

For each step $i > 1$, hysteresis is updated as follows. First, the input transformation is applied. The shifted inputs

$$x_{i,\mathrm{shift}} = x_i + \Delta x_{i-1}, \tag{44}$$

$$x_{i-1,\mathrm{shift}} = x_{i-1,\mathrm{prev}} + \Delta x_{i-1} \tag{45}$$

include the input x_i, the last input $x_{i-1,\mathrm{prev}}$ considered for updating hysteresis, and the most recent saturation marker Δx_{i-1}, ensuring that the model operates within $[0, \Delta x_{\max}]$.

Next, α_i and β_i are computed from $x_{i,\mathrm{shift}}$ and the reset variables $\Delta x_{i-1,\mathrm{reset,ch}}$ and $\Delta x_{i-1,\mathrm{reset,dch}}$, which are updated after each step and store information on the last $x_{i-1,\mathrm{shift}}$ value before a direction change. They encode distances to the saturation limits 0 and $\Delta x_{\max}$ and enable consistent re-transformation of α_i and β_i when the input direction reverses, in accordance with the wipe-out property of the flipped triangle. Thus, α_i and β_i are defined as:

$$\alpha_i = x_{i,\mathrm{shift}} - \Delta x_{i-1,\mathrm{reset,ch}} \tag{46}$$

$$\beta_i = x_{i,\mathrm{shift}} - \Delta x_{i-1,\mathrm{reset,dch}} \tag{47}$$

In other words, α_i and β_i incorporate both saturation and input direction resets, which are required to interpret each experimentally determined minor loop separately, while enabling later simulation with parameter inter-/extrapolation over the whole SOC range and preserving the wipe-out property.

With α_i and β_i known, hysterons and auxiliary variables are updated from step $i-1$ to i. An "up-switching" case with $x_{i,\mathrm{shift}} - x_{i-1,\mathrm{shift}} > \epsilon_{\mathrm{preisach}}$ is calculated as:

$$\zeta_{i,\alpha_{\hat{i}},\beta_{\hat{j}}} = \begin{cases} 1, & \text{if } \alpha_i > \alpha_{\hat{i}} \text{ and } \zeta_{i-1,\alpha_{\hat{i}},\beta_{\hat{j}}} = -1, \\ \zeta_{i-1,\alpha_{\hat{i}},\beta_{\hat{j}}}, & \text{otherwise.} \end{cases} \tag{48}$$

$$\forall\, \hat{i},\ \hat{j}$$

$$\begin{aligned} \Delta x_{i,\mathrm{reset,ch}} &= \Delta x_{i-1,\mathrm{reset,ch}} \\ \Delta x_{i,\mathrm{reset,dch}} &= x_{i,\mathrm{shift}} - \Delta x_{\max} \\ x_{i,\mathrm{prev}} &= x_i \end{aligned} \tag{49}$$

For "down-switching" with $x_{i,\mathrm{shift}} - x_{i-1,\mathrm{shift}} < -\epsilon_{\mathrm{preisach}}$ the calculation is specified as:

$$\zeta_{i,\alpha_{\hat{i}},\beta_{\hat{j}}} = \begin{cases} -1, & \text{if } \beta_i \le \beta_{\hat{j}} \text{ and } \zeta_{i-1,\alpha_{\hat{i}},\beta_{\hat{j}}} = 1, \\ \zeta_{i-1,\alpha_{\hat{i}},\beta_{\hat{j}}}, & \text{otherwise.} \end{cases} \tag{50}$$

$$\forall\, \hat{i},\ \hat{j}$$

$$\begin{aligned} \Delta x_{i,\mathrm{reset,ch}} &= x_{i,\mathrm{shift}} \\ \Delta x_{i,\mathrm{reset,dch}} &= \Delta x_{i-1,\mathrm{reset,dch}} \\ x_{i,\mathrm{prev}} &= x_i \end{aligned} \tag{51}$$

The update rules in Eqs. (48)–(51) reflect the behavior described above. The reset variables $\Delta x_{i,\mathrm{reset,ch}}$ and $\Delta x_{i,\mathrm{reset,dch}}$ track the last input values at which the model "anchors" to the saturation boundaries, enabling correct handling of input direction changes. In accordance, $x_{i,\mathrm{prev}}$ is updated with the surpassed threshold $\epsilon_{\mathrm{preisach}}$. The threshold ensures that hysteresis is updated only if the change in input is sufficiently large to suppress noise and avoid large model drifts caused by recurring small input direction changes (see later discussion on recuperation- and interpolation-induced drift).

If the threshold $\epsilon_{\mathrm{preisach}}$ is not exceeded, no hysterons are switched, and the previous state is carried forward:

$$\begin{aligned} \zeta_{i,\alpha_{\hat{i}},\beta_{\hat{j}}} &= \zeta_{i-1,\alpha_{\hat{i}},\beta_{\hat{j}}} \\ \Delta x_{i,\mathrm{reset,ch}} &= x_{i-1,\mathrm{reset,ch}} \\ \Delta x_{i,\mathrm{reset,dch}} &= \Delta x_{i-1,\mathrm{reset,dch}} \\ x_{i,\mathrm{prev}} &= x_{i-1,\mathrm{prev}} \end{aligned} \tag{52}$$

At each time step i, once the hysteron states are updated, Eq. (34) is used to compute $h_{i,\mathrm{preisach,lit}}$. As a last operation per time step i, before forwarding to $i+1$ beginning with Eq. (44), the saturation marker Δx_i is reset if the model reaches $h_{i,\mathrm{preisach,lit}} \ge 1$ or $h_{i,\mathrm{preisach,lit}} \le -1$ (indirectly exceeding $\Delta x_{\max}$, i.e., $\alpha_{\max}$ or $\beta_{\max}$) during parameterization or simulation:

$$\Delta x_i = \begin{cases} \Delta x_{i-1}, & -1 < \mathrm{round}(h_{i,\mathrm{preisach,lit}}, 4) < 1, \\ -x_i + \Delta x_{\max}, & \mathrm{round}(h_{i,\mathrm{preisach,lit}}, 4) \ge 1, \\ -x_i, & \mathrm{round}(h_{i,\mathrm{preisach,lit}}, 4) \le -1. \end{cases} \tag{53}$$

With this general formulation, the novel Modified Preisach model fully satisfies the previously defined framework, including the requirement of clockwise, monotonically increasing loops. Its application to OCV hysteresis proceeds as follows. The discrete input x_i is set to SOC_i, and the switching threshold is chosen as $\epsilon_{\mathrm{preisach}} = 0.165$, corresponding to $|\Delta SOC| \ge 0.165\,\%$ for updating hysterons. The parameterization is performed using the $N_{\mathrm{loop}} = 5$ minor loops with $n_{\mathrm{loop}} = 14$ points each and their respective $SOC_{i,\mathrm{avg,loop}}$ (Section 2.1). The maximum plane coordinates are set to the largest SOC span within a minor loop, yielding $\Delta x_{\max} = \alpha_{\max} = \beta_{\max} = 30$ (i.e., $\Delta SOC = 30\,\%$). The number of discretization points per axis is $N_\alpha = N_\beta = 7$, aligned with $n_{\mathrm{loop}} = 14$. A single set of weights $\mu_{i,\alpha_{\hat{i}},\beta_{\hat{j}}} \ge 0$ is used for both charge and discharge direction. Under these conditions, the model has 28 independent weights per minor loop, which is a reasonable compromise between resolution, parameterization effort, and available measurement data.

With charge-direction-independent weights, only SOC variation may produce points of non-differentiability via parameter inter- and extrapolation, whereas hysteron switching adds discontinuities in the hysteresis trajectories when switching thresholds are crossed, including those thresholds triggered by changes in charge direction. These points with discontinuities in the hysteresis trajectories are also non-differentiable. Given $N_\alpha = N_\beta = 7$ and $\Delta x_{\max} = 30$, switching occurs only for $|\Delta SOC| \ge 5\,\%$ or when the charge direction changes, so the dominant influence on trajectories arises from the inter- and extrapolation of weights. Although discontinuities and thus, undefined derivatives arise when hysterons switch, the requirement of piecewise continuous differentiability is not violated. Unlike the previous models, this approach does not predict the hysteresis for the next time step $i+1$. Therefore, SOC_i is used directly. An adjustment for coulombic efficiency is also neglected here. The overall equation for OCV including OCV hysteresis yields:

$$OCV_{i,\mathrm{preisach}} = OCV_{i,\mathrm{dch}} + \frac{1}{2}\left(h_{i,\mathrm{preisach,lit}} + 1\right) \cdot H_{i,\max} \tag{54}$$

Yet again, recuperation and interpolation-induced drift need to be analyzed for the Modified Preisach model. Regarding the triggers of recuperation-induced drift, the model exhibits non-linearity due to its switching behavior, as well as its reset and transformation mechanisms. At the same time, however, there are no additional charge-direction-dependent parameters that could cause additional recuperation-induced drift. The effect of non-linearity is partially suppressed by the switching threshold $\epsilon_{\mathrm{preisach}}$, which prevents frequent back-and-forth switching between the charge and discharge direction. In particular, the parameter reset triggered by switching the charge direction, making α_i or β_i start from the model's respective saturation point (i.e., 0 or $\Delta x_{\max}$) over and over, can cause extreme drift with input noise and frequent recuperation in the absence of this threshold. Further, potentially asymmetric weight distributions can introduce additional recuperation-induced drift. Besides that, interpolation-induced drift arises from the SOC-dependent parameterization used. Similar to the Roscher model, the Modified Preisach model uses a normalized hysteresis $h_{i,\mathrm{preisach,lit}}$. It is only scaled by $H_{\max}$, which exhibits non-monotonic behavior due to the holistic OCV hysteresis representation of LFP and graphite. Subsequently, this model also may exhibit, in addition to the interpolation- and recuperation-induced drift, a meaningful, yet drift-like hysteresis trajectory that follows the trajectory

of $H_{\max}$. The magnitude of these effects and their impact on overall model quality, along with comparisons to other models, are analyzed in Sections 4 and 5. Additional model properties (time forwarding, loop asymmetry, and parameterization) reported in Table 5 are derived in Appendix E.

In conclusion, the OCV hysteresis of the discrete Modified Preisach model, as defined in Eq. (34), is systematically and discretely parameterized and analyzed using the normalized variable $h_{i,\text{preisach}}$ (see Eq. (4)) instead of the literature definition $h_{i,\text{preisach,lit}}$. Simulation is carried out using the model-specific definition of OCV hysteresis ($h_{i,\text{preisach,lit}} \in [-1, 1]$). In this context, the model's OCV hysteresis is not treated as a state variable. Thus, only the Plett One-State model introduces OCV hysteresis as an additional state. In Section 3.4, the additional reference OCV in the exemplary output equation of the ECM (Section 3.3) is replaced by the required OCV_{dch} for this hysteresis model.

It should be noted that the modification introduced here concerns the geometry of the switching domain only. Defining the Preisach triangle in flipped form reverses the ordering of the switching thresholds of each hysteron, so that the increasing branch lies above the decreasing one and clockwise, monotonically increasing loops result. The switching mechanism itself is retained: hysterons continue to switch between −1 and 1 upon threshold crossing, so that the wiping-out property and the characteristic staged hysteresis trajectories are preserved (see Eqs. (48)–(51) and Fig. 3(f)). While many discrete implementations disregard loop orientation altogether, corrections of the switching domain have been shown to yield the required orientation without affecting the characteristic properties of the Preisach model, even though formulated within the Everett framework [36,89]. The modification proposed here transfers this principle to the discrete formulation, where it follows directly from the model equations, so that the resulting loop orientation is independent of the cell to which the model is applied. Accordingly, a cross-cell study of this model adaptation lies outside the scope of this work, whose objective is the comparison of OCV hysteresis models against each other. This requires an identical cell, ECM, parameterization, and validation profile for all models, so that observed differences are attributable to the hysteresis formulations alone.

Having described all key aspects of the OCV hysteresis models under investigation and summarized them in Table 5, Fig. 3 illustrates the schematic behavior of each model in terms of the normalized hysteresis factor h_i (Eq. (4)). In addition to the non-linear constraints that limit the hysteresis between the major loops during parameterization, all models that do not inherently remain between OCV_{dch} and OCV_{ch} include an additional corrective term to prevent exceeding the major loops during simulation. This applies to the Plett One-State and the Huria model, whereas the Roscher model, through the saturation of $\psi_{i,1}$ and $\psi_{i,2}$, and the Modified Preisach model, through Eq. (35) together with $\mu_{i,\alpha_i,\beta_j} \geq 0$, remain within the admissible range by construction.

3.3. Analysis of the ECM and parameterization

As outlined in the previous section, a baseline time-discrete ECM and its parameterization, including parameter interpolation, are derived here. The fully empirical model follows a well-established structure with a series resistance and two RC elements [17,96]. This structure is sufficient to capture the polarization of LFP graphite cells [37]. The corresponding system and output equations are:

$$\mathbf{x}_{i+1} = f_{\mathbf{x}_{i+1}} = f(\mathbf{x}_i, \mathbf{u}_i) \tag{55}$$

$$y_i = g_{\mathbf{x}_i} = g(\mathbf{x}_i, \mathbf{u}_i) \tag{56}$$

In the following equations, all model parameters are, analogously to the OCV hysteresis models, linearly interpolated. Unlike the OCV hysteresis models, the ECM parameters do not require extrapolation, as their measurement procedure described in Section 2 covers the entire SOC operating window of the validation profile. OCV_{avg} is initially chosen as reference OCV; in the framework of Section 3.4, it is substituted by the respective reference OCV implied by each OCV hysteresis model from Section 3.2. The parameters of the two RC elements and the series resistance depend on SOC, C-Rate, and charge direction. They are interpolated, and switched accordingly during simulation. Their parameters R_0, R_1, R_2, τ_1, and τ_2, are optimized using Matlab's `lsqcurvefit` algorithm. The optimization is carried out in discrete time using the isolated pulses from the HPPC protocol described in Section 2.1. Parameterization is performed for each charge direction, C-Rate and SOC point listed in Table 1, resulting in a parameterization

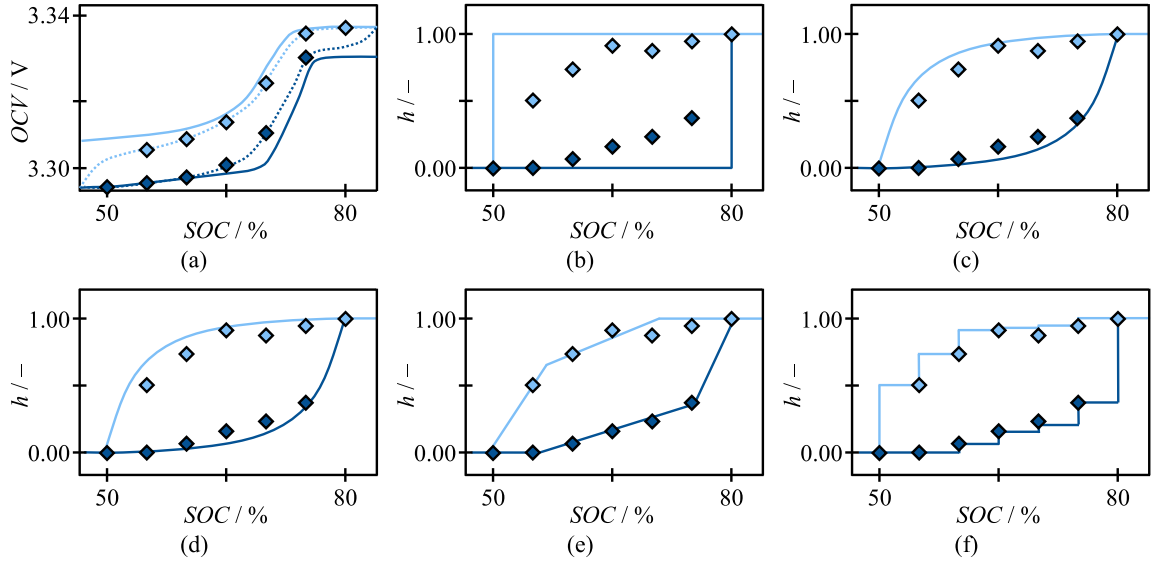


Fig. 3. Schematic description of a measured minor OCV hysteresis loop and the resulting trajectories of the normalized hysteresis factor h_{mod} for the models under investigation. (a) Schematic minor loop bounded between OCV_{dch} and OCV_{ch}. (b) Schematic trajectories of h_{direct} and h_{plett0} for the direct OCV and the Plett Zero-State model. (c) Schematic trajectory of h_{plett1} for the Plett One-State model. (d) Schematic trajectory of h_{huria} for the Huria model. (e) Schematic trajectory of h_{roscher} for the Roscher model. (f) Schematic trajectory of h_{preisach} for the Modified Preisach model.

Table 6
Parameterization results of the ECM with a series resistance and two RC elements for all pulses across SOC, C-Rate, and charge direction for the ANR26650m1b LFP graphite cell.

	MAE / mV	RMSE / mV
Mean	1.910	2.239
Maximum	14.218	15.696
Minimum	0.041	0.052

designed to match behavior under load. To better capture relaxation behavior, an additional rest-phase parameterization is introduced. Here, the C/3 pulses in charge and discharge are used to approximate a parameterization representing pure relaxation behavior (i.e. $I_{\mathrm{app}} \approx 0\,\mathrm{A}$) by averaging the parameterization results from both charge and discharge direction. This is reasonable, since the average absolute current of the validation profile during load is 0.830 A, corresponding to 0.319 C.

For each load-phase parameterization, lower and upper bounds restrict the parameters to physically meaningful ranges. To improve accuracy, a weighting between the pulse behavior during load and rest is applied during fitting, so that both polarization rise and decay are properly considered. For the rest-phase parameterization, parameter bounds and weightings are adjusted to emphasize long-term relaxation processes. Both parameterizations describe polarization rise and decay, but the decay is stronger weighted for the rest-phase parameterization. This procedure results in a lookup table capturing the parameter dependencies on SOC, C-Rate, and charge direction. The parameterization results in terms of MAE and root mean square error (RMSE) can be found in Table 6.

During fitting, parameter bounds and weights for the load-phase and rest-phase parameterization are tuned to optimally describe the validation profile by the ECM in combination with OCV_{avg}. Using OCV_{avg} minimizes model bias or advantages for any particular hysteresis model by preventing undesired compensation of hysteresis through the parameterization of an ECM with a series resistance and two RC elements. The parameters must account for behavior near both OCV_{ch} and OCV_{dch}. The OCVs used in the baseline ECM and in Section 3.4 are directly obtained from experiments (see Section 2.1). From this ECM conception, the resulting system and output equations are given by:

$$\begin{bmatrix} V_{i+1,\mathrm{RC}_1} \\ V_{i+1,\mathrm{RC}_2} \\ SOC_{i+1} \end{bmatrix} = \begin{bmatrix} \mathrm{e}^{-\frac{\Delta t}{\tau_{i,1}}} & 0 & 0 \\ 0 & \mathrm{e}^{-\frac{\Delta t}{\tau_{i,2}}} & 0 \\ 0 & 0 & 1 \end{bmatrix} \begin{bmatrix} V_{i,\mathrm{RC}_1} \\ V_{i,\mathrm{RC}_2} \\ SOC_i \end{bmatrix} + \begin{bmatrix} R_{i,1}\left(1-\mathrm{e}^{-\frac{\Delta t}{\tau_{i,1}}}\right) \\ R_{i,2}\left(1-\mathrm{e}^{-\frac{\Delta t}{\tau_{i,2}}}\right) \\ \frac{\Delta t \cdot 100}{C_{\mathrm{n}}} \end{bmatrix} \left[I_{i,\mathrm{app}}\right] \tag{57}$$

$$V_{i,\mathrm{OCV}_{\mathrm{avg}}} = OCV_{i,\mathrm{avg}} + V_{i,\mathrm{RC}_1} + V_{i,\mathrm{RC}_2} + R_{i,0}\, I_{i,\mathrm{app}} \tag{58}$$

In the output equation, i.e. Eq. (58), all additional polarization terms are added to the OCV, since $I_{\mathrm{app}} > 0\,\mathrm{A}$ is defined as charging current. The same sign convention is used for Coulomb counting in all hysteresis models (Section 3.2) and for SOC calculation in the system equation (see Eq. (57)). For consistency, the coulombic efficiency η_{coul} is also assumed to be 1 here. The indices i and $i+1$ denote time advancement according to Eqs. (55) and (56). For $OCV_{i,\mathrm{avg}}$ and for the parameters of the series resistance and the two RC elements, i indicates interpolation with respect to the current SOC_i and, if applicable, with respect to the applied current $I_{i,\mathrm{app}}$, including charge direction. The model states are SOC_i, V_{i,RC_1}, and V_{i,RC_2}. The observer- and filter-readiness is demonstrated by Plett [17] and Wassiliadis et al. [96].

3.4. Finalization of the time-discrete simulation framework

The time-discrete ECM must now be adapted to the respective OCV hysteresis models derived in Section 3.2. Apart from the Plett One-State model, all hysteresis models only require modification of the output equation (Eq. (58)), since they do not introduce an additional state.

For the direct OCV model, a fixed OCV based on the auxiliary variable θ is used. In this study, θ is set to 0, 0.5, and 1, resulting in $OCV_{i,\mathrm{direct}}$ equal to $OCV_{i,\mathrm{direct,dch}}$, $OCV_{i,\mathrm{direct,avg}}$, or $OCV_{i,\mathrm{direct,ch}}$, respectively. Combined with Eq. (58), this yields the model outputs $V_{i,\mathrm{OCV}_{\mathrm{direct,dch}}}$, $V_{i,\mathrm{OCV}_{\mathrm{direct,ch}}}$, and $V_{i,\mathrm{OCV}_{\mathrm{direct,avg}}}$. The Plett Zero-State model switches between charge and discharge OCV based on the current thresholds ϵ_{ch} and ϵ_{dch}. Accordingly, $OCV_{i,\mathrm{avg}}$ in Eq. (58) is replaced by $OCV_{i,\mathrm{plett0}}$ from Eq. (13), leading to $V_{i,\mathrm{OCV}_{\mathrm{plett0}}}$.

With the additional state variable in the Plett One-State model, both the system equation and the output equation of the baseline ECM must be modified. Eq. (57) is extended to:

$$\begin{bmatrix} V_{i+1,\mathrm{RC}_1} \\ V_{i+1,\mathrm{RC}_2} \\ SOC_{i+1} \\ h_{i+1,\mathrm{plett1,lit}} \end{bmatrix} = \begin{bmatrix} \mathrm{e}^{-\frac{\Delta t}{\tau_{i,1}}} & 0 & 0 & 0 \\ 0 & \mathrm{e}^{-\frac{\Delta t}{\tau_{i,2}}} & 0 & 0 \\ 0 & 0 & 1 & 0 \\ 0 & 0 & 0 & p(\gamma_i, I_{i,\mathrm{app}}) \end{bmatrix} \begin{bmatrix} V_{i,\mathrm{RC}_1} \\ V_{i,\mathrm{RC}_2} \\ SOC_i \\ h_{i,\mathrm{plett1,lit}} \end{bmatrix} + \begin{bmatrix} R_{i,1}\left(1-\mathrm{e}^{-\frac{\Delta t}{\tau_{i,1}}}\right) & 0 \\ R_{i,2}\left(1-\mathrm{e}^{-\frac{\Delta t}{\tau_{i,2}}}\right) & 0 \\ \frac{\Delta t \cdot 100}{C_{\mathrm{n}}} & 0 \\ 0 & 1-p(\gamma_i, I_{i,\mathrm{app}}) \end{bmatrix} \begin{bmatrix} I_{i,\mathrm{app}} \\ \mathrm{sgn}(I_{i,\mathrm{app}})\,\frac{1}{2}H_{i,\max} \end{bmatrix} \tag{59}$$

The output equation (Eq. (58)) is then extended by substituting $OCV_{i,\mathrm{avg}}$ with $OCV_{i,\mathrm{plett1}}$ according to Eq. (19), yielding $V_{i,\mathrm{OCV}_{\mathrm{plett1}}}$. The Huria model does not introduce an additional state and inherently provides an OCV including hysteresis. Thus, only Eq. (58) is modified by replacing $OCV_{i,\mathrm{avg}}$ with $OCV_{i,\mathrm{huria}}$ from Eq. (27), resulting in $V_{i,\mathrm{OCV}_{\mathrm{huria}}}$. Similarly, the Roscher model is formulated without an additional state. Using Eq. (33), Eq. (58) is adjusted to use $OCV_{i,\mathrm{roscher}}$ instead of $OCV_{i,\mathrm{avg}}$, giving $V_{i,\mathrm{OCV}_{\mathrm{roscher}}}$. Finally, the Modified Preisach model also acts as an additive correction to a baseline OCV and does not introduce further states. Accordingly, Eq. (58) is modified by replacing $OCV_{i,\mathrm{avg}}$ with $OCV_{i,\mathrm{preisach}}$ from Eq. (54), leading to $V_{i,\mathrm{OCV}_{\mathrm{preisach}}}$.

In summary, this section has established the complete modeling framework by providing an in-depth review and categorization of existing OCV hysteresis models, implementing the most relevant empirical approaches, including a novel Modified Preisach model, and deriving a baseline ECM that is combined with each hysteresis model. On this foundation, the following sections present detailed simulations, comparisons, and discussions of the OCV hysteresis modeling approaches introduced here. All parameterization processes and simulations are carried out using Matlab R2023b (64-bit Windows). The validation profile is simulated with a fixed time step of $\Delta t = 1$ s, corresponding to $N_{\mathrm{steps}} = 59756$ time steps over the complete profile duration of 16.6 h.

4. Results

After introducing all relevant empirical OCV hysteresis models in the previous section, this section presents the results obtained with the validation profile from Section 2. It is structured into an assessment of overall model performance in Section 4.1 and a detailed analysis of the simulation results of each OCV hysteresis model in Section 4.2. Unless stated otherwise, the hysteresis metrics h and H from Eqs. (4) and (2) are used here, in Section 5, and in Appendix G. In general, they are denoted as h_{mod} and H_{mod}. Furthermore, OCV_{mod} and $V_{\mathrm{OCV}_{\mathrm{mod}}}$ are used as general terms to refer to the modeled OCV and cell voltage.

This choice partly contradicts the h factors defined in the original literature for some models (see Section 3.2). In particular, the hysteresis factors $h_{i,\mathrm{plett1,lit}}$ and $h_{i,\mathrm{preisach,lit}}$ are replaced by $h_{i,\mathrm{plett1}}$ and $h_{i,\mathrm{preisach}}$,

respectively. In addition, $h_{i,\mathrm{huria}}$ is introduced; all other approaches already comply with the definition of h according to Eq. (4). The corresponding transformations are given in the Appendix by Eqs. (B.1), (C.1), and (E.1).

4.1. Evaluation of the overall model performance

The modeling results are presented in Fig. 4 in a separated form that highlights the impact of individual model components. Accordingly, the results are examined in the following order: first the modeled OCVs, then the hysteresis voltage H_{mod}, and finally the modeled polarization $\eta_{\mathrm{OCV_{mod}}}$. The result of H_{mod} is deliberately displayed here to identify the drifts described in the previous section (recuperation- and interpolation-induced) as well as the drift-like behavior of the hysteresis models excited by a direct dependency on or by scaling with H_{max}. Later on, particularly during the discussion, h_{mod} will be used to represent hysteresis without this drift-like behavior.

Throughout this section and the subsequent discussion in Section 5, the error metric is consistently defined as $\mathcal{X}_{\mathrm{measured}} - \mathcal{X}_{\mathrm{mod}}$, where $\mathcal{X}$ denotes an arbitrary quantity. For example, the error relative to the measured voltage V_{measured} is defined as $\Delta V_{\mathrm{OCV_{mod}}} = V_{\mathrm{measured}} - V_{\mathrm{OCV_{mod}}}$. As described in Section 2, the validation profile comprises load and rest phases aligned with typical customer behavior. Because empirically determined hysteresis cannot change during rest, e.g. through equilibration processes within the electrode, only the three load phases Load_1, Load_2 and Load_3 are shown for improved visibility.

Thus, Fig. 4(a)–(c) depict the simulated OCVs including hysteresis in all three load phases. Owing to the stationary behavior of all hysteresis models during rest, the OCV hysteresis validation points P_1, P_2, P_3, and P_4 can be assigned to the beginning as well as the end of the respective load phases. All models are initialized with OCV_{ch} (see Fig. 4(a)). From this starting point, the simulated OCV_{ch} and OCV_{dch} generally decrease over time, with some increases due to recuperation.

For the phases Load_1 and Load_2 (P_1–P_2 and P_2–P_3), the simulated OCVs including hysteresis of all models also exhibit an overall decrease, again with small increases from recuperation and one strong recuperation event in the phase Load_2 at around 5.6 h, which causes all models to shift and, in particular, drives the Modified Preisach model into a higher hysteresis state. This behavior reflects the net discharge in all load phases, which advances the OCVs including hysteresis from OCV_{ch} towards OCV_{dch}, with model-specific trajectories. The phase Load_3 (P_3–P_4) in Fig. 4(c) requires special attention: while the major loops again decrease, some hysteresis models show an increase in their OCV including hysteresis. This behavior is observed for the Modified Preisach, the Huria, and the Plett One-State model, which are all associated with drift in Section 3.2. The occurrence and likelihood of this phenomenon are discussed in detail in Section 5.2. The model performance at the OCV hysteresis validation points P_1–P_4 is also visible in Fig. 4(a)–(c).

Fig. 4(d)–(f) shows H_{mod} (Eq. (2)), i.e. the hysteresis trajectories of all models in non-normalized form. First, H_{max} is analyzed. The proportion of LFP hysteresis in the holistic OCV hysteresis represented by H_{max} is expected to remain constant, since LFP undergoes only a single phase transition during lithiation. Thus, all changes in H_{max} are attributed to graphite staging. During the phase Load_1, the maximum hysteresis H_{max} is approximately constant at $H_{\mathrm{max}} \approx 5\,\mathrm{mV}$, where the graphite anode transition from LiC_6 to LiC_{12} takes place (see Load_1, Fig. 4(d)). The phase Load_2 in Fig. 4(e) begins within this transition and then proceeds into the transition from LiC_{12} to LiC_{18}, resulting in a constant $H_{\mathrm{max}} \approx 11\,\mathrm{mV}$, which also applies to the phase Load_3 (Fig. 4(f)). During saturation of the LiC_{12} phase, the maximum hysteresis reaches a peak of about 23 mV. This peak may arise from charge-direction-dependent phase changes at the graphite plateau transition or from incompletely relaxed major loops (OCV_{ch} and OCV_{dch}). The former can be investigated via differential voltage analysis (DVA) and tracking of graphite peaks, as shown for example in Klick et al. [97], where peak shifts between charge and discharge are observed. Yet, as stated, electrochemical processes in this lithiation range may be slowed, affecting both DVA and thus peak positions.

For the present study, any slowed relaxation in this graphite-lithiation window during OCV_{ch} and OCV_{dch} measurement has been compensated using DRT-based extrapolation and is therefore assumed negligible (see Section 2). The DRT-based corrections in the plateau transition region are consistent with the increased relaxation gradients observed there. Subsequently, due to the influence of graphite on the overall OCV hysteresis behavior, primarily through H_{max}, holistic OCV hysteresis modeling of graphite and LFP requires explicit consideration of graphite hysteresis effects on the modeling results. The explicit impact of graphite staging on model quality will be revisited in Section 5.3. Given this characterization of H_{max}, the hysteresis trajectories in Fig. 4(d)–(f) can be analyzed in more detail.

For the direct OCV models, $H_{\mathrm{direct,ch}} = H_{\mathrm{max}}$, $H_{\mathrm{direct,avg}} = \frac{1}{2} H_{\mathrm{max}}$, and $H_{\mathrm{direct,dch}} = 0\,\mathrm{mV}$ follow. In the Plett Zero-State model, switching occurs when $I_{i,\mathrm{app}} > \epsilon_{\mathrm{ch}}$ or $I_{i,\mathrm{app}} < \epsilon_{\mathrm{dch}}$, mainly due to recuperation; thus, H_{plett0} is either 0 mV or H_{max}, visible as spikes during short recuperation phases.

The behavior of H_{plett1} of the Plett One-State model requires closer inspection. As described in Section 3.2, H_{plett1} is governed by H_{max}. In the phase Load_1, H_{plett1} decreases continuously due to net discharge and nearly constant H_{max}. In the phase Load_2, H_{plett1} continues to decrease until H_{max} increases due to the graphite plateau change. The corresponding drift-like increase in H_{plett1} is meaningful because it is driven by the increase in H_{max}. As H_{max} later converges to about 11 mV and net discharge continues, H_{plett1} declines and reaches 0 mV at the end of the phase Load_2. In the phase Load_3, H_{plett1} exhibits an unfavorable drift, which cannot be explained by the behavior of H_{max}. This drift due to strong recuperation and the model's tendency towards recuperation-induced drift as well as its interpolation-induced drift is elucidated in Section 5.2.

The Huria model behaves similarly in the phase Load_1. In the phase Load_2, its behavior differs from the Plett One-State model despite both following an exponential approach: in the Huria model, OCV hysteresis is not governed by H_{max} but by the reference OCV, which under net discharge is mostly OCV_{dch}. As described, due to the monotonicity of OCV_{dch}, H_{huria} does not exhibit drift-like behavior resulting from the trajectory of H_{max} and converges to 0 mV earlier. In the remainder of the phases Load_2 and Load_3, the Huria model again displays an unfavorable drift caused by strong recuperation. Its occurrence due to the tendency towards recuperation-induced drift as well as its interpolation-induced drift is elucidated in Section 5.2. Especially the drift in phase Load_2 is less apparent in the overall OCV depicted in Fig. 4(b), as it still decreases.

The Roscher model, defined via h_{roscher}, is neither governed directly by a reference OCV nor by H_{max} alone. Its normalized approach is only scaled by H_{max}. Consequently, H_{roscher} decreases continuously in the phase Load_1, and then rises in the phase Load_2 due to scaling with H_{max}. At the end of the phase Load_2, when H_{max} converges to about 11 mV, H_{roscher} also converges to 0 mV. The shape of this trajectory depends on net discharge and the scaling behavior with H_{max}, which introduces a drift-like, yet meaningful trajectory of H_{roscher}. Once a minimum hysteresis of 0 mV is reached, the linear Roscher model, other than the Plett One-State and the Huria model, does not exhibit relevant drift, even under significant recuperation. Thus, H_{roscher} remains at (or very close to) 0 mV in the phase Load_3. Nevertheless, the recuperation- and interpolation-induced drift will also be elucidated for the Roscher model in Section 5.2.

For the Modified Preisach model, h_{preisach} governs a transition between −1 and 1, and the resulting hysteresis is then scaled by H_{max}. As a result, H_{preisach} decreases in the phase Load_1. The discrete switching steps are clearly visible. In the phase Load_2, H_{preisach} increases due to scaling with H_{max} and subsequently decreases again due to net discharge and the eventual stabilization of H_{max}, which is continued

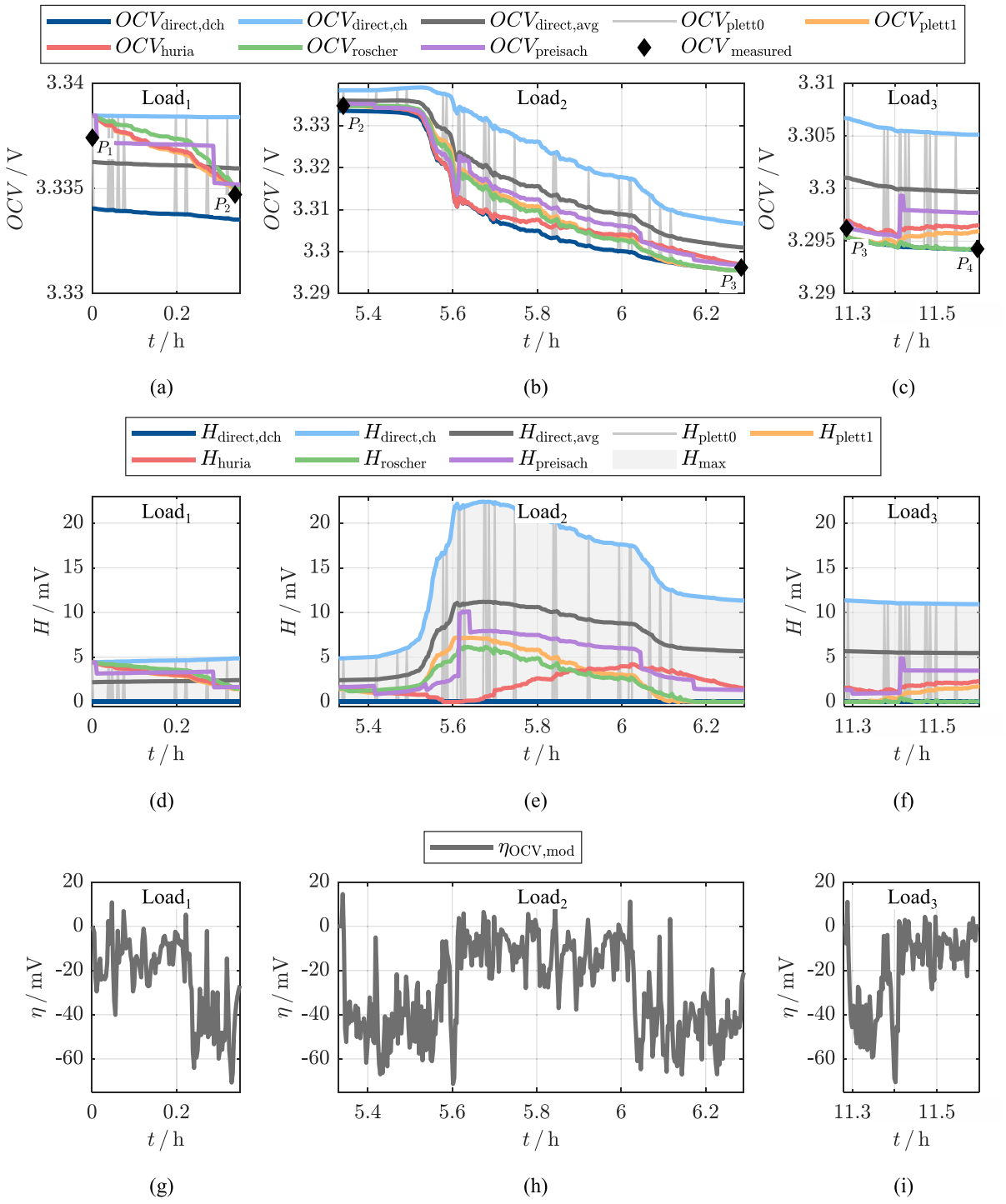


Fig. 4. Separated simulation results of the validation profile for all models under investigation. Depicted are only the three load phases Load_1, Load_2 and Load_3. (a)–(c) Simulated OCVs including OCV hysteresis and measured OCV hysteresis validation points P_1, P_2, P_3 and P_4. (d)–(f) Resulting OCV hysteresis described by H_{mod} in mV. (g)–(i) Additional polarization $\eta_{\text{OCV}_{\text{mod}}}$ by the ECM consisting of a series resistance and two RC elements.

in the phase Load_3. Yet again, this drift-like behavior from scaling with H_{max} is meaningful. Similar to the Plett One-State and the Huria model, the Modified Preisach model tends to drift during strong recuperation. In this case, however, the recuperation-induced drift is caused by the input transformation and reset mechanisms necessary for the Preisach triangle (see Section 3.2). Thus, drift may occur when recuperation events exceed the switching threshold $\epsilon_{\text{preisach}} = 0.165$, i.e. when $|\Delta SOC| > 0.165\,\%$. This is observed in the phases Load_2 and Load_3 for two pronounced recuperation pulses. This tendency towards recuperation-induced drift as well as the model's interpolation-induced drift is elucidated in Section 5.2 including mitigation strategies for the former by increasing $\epsilon_{\text{preisach}}$.

Fig. 4(g)–(i) shows the modeled polarization $\eta_{\text{OCV}_{\text{mod}}}$, which is identical for all models and results from the series resistance and the two RC

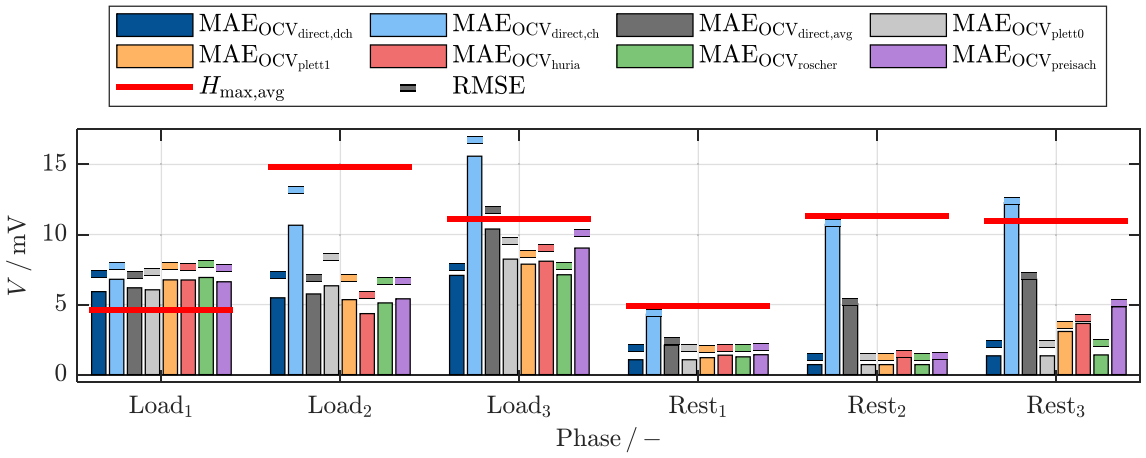


Fig. 5. MAE and RMSE of the validation profile based on $\Delta V_{OCV_{mod}} = V_{measured} - V_{OCV_{mod}}$ for each OCV hysteresis model, comprising both hysteresis and polarization error. Results are displayed for each load and rest phase of the validation profile and include additional information on the prevalent $H_{max,avg}$ in each phase.

elements of the ECM described in Sections 3.3 and 3.4. The separation of errors attributable to polarization $\eta_{OCV_{mod}}$ and OCV hysteresis H_{mod} is discussed in Section 5.1.

Fig. 5 and Table 7 summarize the model errors. Fig. 5 shows MAE and RMSE for each load and rest phase. In all phases, MAE and RMSE are of similar magnitude, indicating that outliers and extreme errors are rare. The average maximum hysteresis $H_{max,avg}$ is also shown to indicate the significance of OCV hysteresis-related contributions to the error. The error metrics reflect both hysteresis and polarization error. However, even though the same parameterization of the series resistance and the two RC elements of the ECM are used for all models and thus, its relative error contribution by $\eta_{OCV_{mod}}$ remains the same, the polarization error does not impact the overall error of each model in the same way: depending on the accuracy of the OCV hysteresis, it may either worsen or improve the overall errors. Therefore, comparing the error metrics to $H_{max,avg}$, which can be interpreted as the average maximum hysteresis error, can only be partially used to conclude the impact of polarization errors.

For the phase Load$_1$, $H_{max,avg}$ is approximately 5 mV, while the overall MAE and RMSE (based on $\Delta V_{OCV_{mod}}$) exceed 5 mV for all models. As visible in Fig. 4(a), the measured OCV remains within an intermediate range between the major loops, and all models, including the direct ones, reach a regime where the OCV hysteresis is reasonably well captured. Thus, in this case, hysteresis modeling has a relatively minor impact due to the extent of $H_{max,avg}$ and the measured OCV hysteresis bandwidth compared to the remaining model errors. Meaning that it is likely that the polarization error in absolute terms dominates the overall modeling results in this phase. In the phase Load$_2$, hysteresis modeling becomes more important. As the measured hysteresis already converges towards OCV_{dch} (Fig. 4(b)) and $H_{max,avg}$ is approximately 15 mV, all hysteresis models, as well as the direct ones (except $OCV_{direct,ch}$), perform similarly. The unexpected deviation of the MAE of the $OCV_{direct,ch}$ model below $H_{max,avg}$ can be used to interpret the influence of the parameterization of the series resistance and the two RC elements of the ECM. In this case, the polarization error compensates for the hysteresis error by overestimating polarization, and the modeling results are driven towards the correct OCV hysteresis. However, it cannot be concluded that this behavior generalizes to the other models, because with more accurate hysteresis modeling, errors in polarization can also increase the absolute error metrics. In the phase Load$_3$, a similar pattern is observed. As the measured OCV hysteresis asymptotically approaches OCV_{dch} (Fig. 4(c)), models that converge to OCV_{dch} also perform best. Besides the $OCV_{direct,ch}$ and the $OCV_{direct,avg}$ model, the models exhibiting strong drift, i.e. the Plett One-State, the Huria, and the Modified Preisach model are outperformed by the Roscher model. The Plett Zero-State model performs slightly worse than the $OCV_{direct,dch}$ model due to occasional switching between the major loops, which causes an overestimation of hysteresis. This emphasizes the importance of capturing the OCV hysteresis of a magnitude of $H_{max,avg} \approx 11$ mV in this phase. Compared to the deviation of the MAE of the $OCV_{direct,ch}$ model below $H_{max,avg}$ in phase Load$_2$, the opposite can be observed in this phase: here, the MAE, as in phase Load$_1$, again exceeds $H_{max,avg}$, which can be attributed to polarization errors that, in absolute terms, worsen the overall modeling results in this phase. Yet again, this behavior cannot be generalized.

Table 7
Aggregated model errors for the validation profile from Figs. 4 and 5, with the best-performing models highlighted in bold.

	MAE /mV	RMSE /mV	$\Delta V_{abs,max}$ /mV
$\Delta V_{OCV_{direct,dch}}$	**1.503**	**2.838**	20.665
$\Delta V_{OCV_{direct,ch}}$	9.270	10.175	30.098
$\Delta V_{OCV_{direct,avg}}$	4.857	5.566	21.956
$\Delta V_{OCV_{plett0}}$	**1.576**	**3.140**	29.246
$\Delta V_{OCV_{plett1}}$	2.096	3.252	**19.236**
$\Delta V_{OCV_{huria}}$	2.447	3.355	20.211
$\Delta V_{OCV_{roscher}}$	**1.585**	**2.825**	**18.918**
$\Delta V_{OCV_{preisach}}$	2.831	3.901	**19.246**

In the rest phases, the MAE and RMSE highlight the improvements achieved through well-designed OCV hysteresis modeling as the impact of polarization errors decreases. In the phases Rest$_1$ and Rest$_2$, all models close to OCV_{dch} have errors below 2 mV, since hysteresis has largely converged to OCV_{dch}. As $H_{max,avg}$ increases across the rest phases, the importance of OCV hysteresis modeling further increases. In the phase Rest$_3$, with $H_{max,avg} \approx 11$ mV, the MAE and RMSE diverge: models with pronounced drift, i.e. the Plett One-State, the Huria, and the Modified Preisach model show errors >4 mV, while the $OCV_{direct,dch}$, the Plett Zero-State, and the Roscher model remain below 2 mV. All rest phases also depend on the relaxation errors of the series resistance and the two RC elements of the ECM, which can cause minor performance differences between models as well as between the rest phases themselves. Given the magnitude of $H_{max,avg}$, this effect is comparatively small.

Table 7 summarizes the errors over the complete validation profile. Again, the MAE and RMSE are based on each $\Delta V_{OCV_{mod}}$. Additionally, the last column reports the maximum absolute voltage error $\Delta V_{abs,max}$. The lowest MAE values are achieved by the $OCV_{direct,dch}$ model, the Plett

Zero-State model, and the Roscher model, with 1.503 mV, 1.576 mV, and 1.585 mV, respectively. The corresponding RMSE values are 2.838 mV, 3.140 mV, and 2.825 mV, respectively. The small differences between MAE and RMSE again suggest a low number of outliers.

The models with the best MAE and RMSE do not necessarily have the smallest maximum absolute voltage error $\Delta V_{\mathrm{abs,max}}$. For this metric, the $OCV_{\mathrm{direct,dch}}$ and the Plett Zero-State model, performing best MAE-wise, are surpassed by the Plett One-State, the Huria, the Roscher, and the Modified Preisach model. The lowest $\Delta V_{\mathrm{abs,max}}$ values are achieved by the Roscher model (18.918 mV), followed by the Plett One-State model (19.236 mV) and Modified Preisach model (19.246 mV). This reflects that modeling the transition between OCV_{ch} and OCV_{dch} reduces the error over the whole OCV hysteresis trajectory.

Among the remaining models apart from the $OCV_{\mathrm{direct,dch}}$, the Plett Zero-State and the Roscher model, the $OCV_{\mathrm{direct,ch}}$ and the $OCV_{\mathrm{direct,avg}}$ models perform worst, as they are the only ones with an MAE and RMSE above 4 mV. The overall performance of the Plett One-State, the Huria, and the Modified Preisach model remains in a range of 2.096 mV–2.831 mV for the MAE and of 3.252 mV–3.901 mV for the RMSE, which is still acceptable compared to the poor-performing direct OCV models. Their relative ranking (Plett One-State, Huria, Modified Preisach) is directly linked to the pronounced drift observed in Fig. 4(e)–(f). The maximum absolute voltage error of these models is generally consistent with their MAEs and RMSEs.

Overall, the most attractive options are models combining robustness (no drift) and simplicity. An additional description of the model input I_{app}, the output $V_{\mathrm{OCV_{mod}}}$ for all hysteresis models, and the error relative to the measured voltage V_{measured} over time is provided in Fig. G.11 in Appendix G. A detailed evaluation of hysteresis errors at the OCV hysteresis validation points P_1–P_4 follows in the next subsection, as only qualitative assessments are possible under load, where polarization and hysteresis are inseparable. This challenge, as well as an in-depth discussion of the drift detected in this section, follows in Section 5.

4.2. Performance of the OCV hysteresis models

The previous subsection highlighted the overall accuracy gains obtained by modeling hysteresis. After analyzing behavior under load and the resulting error metrics, this section focuses on the hysteresis models themselves. The OCV hysteresis validation points P_1–P_4 serve as the only true validation points for OCV hysteresis and thus reveal the accuracy of each approach in describing the transition from OCV_{ch} to OCV_{dch}.

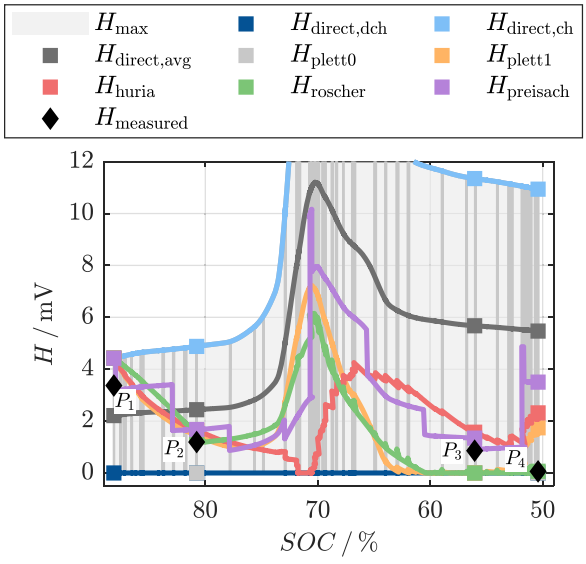


Fig. 6. OCV hysteresis of all models represented by H_{mod} over SOC for the validation profile, including the OCV hysteresis validation points P_1, P_2, P_3, and P_4 (the peak in H_{max} and $H_{\mathrm{direct,ch}}$ is omitted for improved visibility).

Fig. 6 shows the measured OCV hysteresis validation points P_1–P_4 over SOC in combination with each models' H_{mod}, including the $OCV_{\mathrm{direct,ch}}$, the $OCV_{\mathrm{direct,dch}}$, and the $OCV_{\mathrm{direc,avg}}$ model as well as the Plett Zero-State model. This allows to anticipate the true hysteresis trajectory and compare it with the modeling results. The overall behavior partly follows H_{max} due to its direct dependency on or scaling with it, resulting in a drift-like response. This is similar to Fig. 4(d)–(f) and arises from the holistic OCV hysteresis representation incorporating both LFP and graphite. However, in this representation, the influence of recuperation and possibly induced drift becomes more obvious through jagged trajectories. For example, between 70 % and 60 % SOC, this effect is apparent in the Huria and the Roscher model. Furthermore, strong drift observed in the Huria and the Modified Preisach model around 70 % SOC, and in the Plett One-State, the Huria, and the Modified Preisach model around 50 % SOC, coincides with significant switching in the Plett Zero-State model. A detailed analysis of this correlation, which is linked to the rate and magnitude of recuperation, is presented at the discussion of the identified drift behavior in Section 5.2.

In addition to the visual deviations of the models from the OCV hysteresis validation points shown in Fig. 6, Table 8 quantifies the accuracy of each hysteresis model by reporting the errors at P_1–P_4 in terms of $\Delta OCV_{\mathrm{mod}} = OCV_{\mathrm{measured}} - OCV_{\mathrm{mod}}$ and $\Delta h_{\mathrm{mod}} = h_{\mathrm{measured}} - h_{\mathrm{mod}}$, where Δh_{mod} is interpreted as a percentage error. At P_1, all models except the $OCV_{\mathrm{direct,dch}}$ and the $OCV_{\mathrm{direct,avg}}$ model start from $OCV_{\mathrm{direct,ch}}$, i.e. $h_{\mathrm{mod}} = 1$. Due to the deviation of the OCV hysteresis validation point at P_1 from OCV_{ch} described in Section 2, Table 3, the resulting error is $\Delta OCV_{\mathrm{mod}} = -1.054$ mV and $\Delta h_{\mathrm{mod}} = -0.238$ for all of these models. This is the maximum achievable accuracy, as the offset is attributed to the complex two-phase transition behavior of LFP (see Section 2).

At P_2, deviations between models increase and the direct OCV models, as well as the Plett Zero-State model, are clearly outperformed. All real OCV hysteresis models (Plett One-State, Huria, Roscher, Modified Preisach) achieve $|\Delta OCV_{\mathrm{mod}}| < 0.5$ mV and $|\Delta h_{\mathrm{mod}}| < 0.1$. The best results at P_2 are obtained by the Plett One-State model ($\Delta OCV_{\mathrm{plett1}} = -0.242$ mV, $\Delta h_{\mathrm{plett1}} = -0.050$) and the Roscher model ($\Delta OCV_{\mathrm{roscher}} = -0.309$ mV, $\Delta h_{\mathrm{roscher}} = -0.063$).

At P_3, the measured OCV hysteresis has largely converged to OCV_{dch}, so models using OCV_{dch} or converging towards it perform well. The $OCV_{\mathrm{direct,dch}}$, the Plett Zero-State, the Plett One-State, the Huria, the Roscher, and the Modified Preisach model all yield $|\Delta OCV_{\mathrm{mod}}| < 1$ mV and $|\Delta h_{\mathrm{mod}}| < 0.08$. The absolute errors increase compared to P_2 because H_{max} is larger (see Fig. 6). The Huria and the Modified Preisach model perform best at this point, with $\Delta OCV_{\mathrm{huria}} = -0.712$ mV and $\Delta h_{\mathrm{huria}} = -0.063$, as well as $\Delta OCV_{\mathrm{preisach}} = -0.484$ mV and $\Delta h_{\mathrm{preisach}} = -0.043$.

At P_4, hysteresis further converges to OCV_{dch}, and models using or approaching OCV_{dch} outperform the $OCV_{\mathrm{direct,ch}}$ and the $OCV_{\mathrm{direct,avg}}$ model as well as drift-prone models (Plett One-State, Huria, Modified Preisach). The best performance, with $|\Delta OCV_{\mathrm{mod}}| < 0.1$ mV and $|\Delta h_{\mathrm{mod}}| < 0.01$, is observed for the $OCV_{\mathrm{direct,dch}}$, the Plett Zero-State, and the Roscher model. The absolute error range is similar to that at P_3, as H_{max} is comparable. The Plett Zero-State and the $OCV_{\mathrm{direct,dch}}$ model yield $\Delta OCV_{\mathrm{mod}} = 0.061$ mV and $\Delta h_{\mathrm{mod}} = 0.006$, while the Roscher model yields $\Delta OCV_{\mathrm{roscher}} = -0.006$ mV and $\Delta h_{\mathrm{roscher}} = -0.001$.

Since the initial offset at P_1, visible in Fig. 6 and quantified in Table 8, may bias the results, the MAE and RMSE are evaluated separately over P_1–P_4 and P_2–P_4. Considering $\Delta OCV_{\mathrm{mod}}$ (with variable absolute scaling due to H_{max}), the following trends emerge from Table 8: (1) models that perform relatively well at P_1 compared with later points, most notably for the $OCV_{\mathrm{direct,ch}}$ and the $OCV_{\mathrm{direct,avg}}$ model, show worse

Table 8
OCV hysteresis model errors for the validation profile at the OCV hysteresis validation points P_1–P_4, with the best-performing models highlighted in bold. The MAE and RMSE are calculated for P_1–P_4 and P_2–P_4 to assess the bias introduced by the offset at P_1.

	P_1 /mV	P_2 /mV	P_3 /mV	P_4 /mV	$MAE_{P_{1-4}}$ /mV	$MAE_{P_{2-4}}$ /mV	$RMSE_{P_{1-4}}$ /mV	$RMSE_{P_{2-4}}$ /mV
$\Delta OCV_{direct,dch}$	3.370	1.192	0.859	**0.061**	**1.370**	**0.704**	**1.838**	**0.849**
$\Delta OCV_{direct,ch}$	**−1.054**	−3.686	−10.488	−10.878	6.527	8.351	7.795	8.980
$\Delta OCV_{direct,avg}$	1.158	−1.247	−4.815	−5.408	3.157	3.823	3.719	4.242
ΔOCV_{plett0}	**−1.054**	1.192	0.859	**0.061**	**0.791**	**0.704**	**0.905**	**0.849**
ΔOCV_{plett1}	**−1.054**	**−0.242**	0.859	−1.680	0.959	0.927	1.088	1.098
ΔOCV_{huria}	**−1.054**	−0.444	**−0.712**	−2.256	1.116	1.137	1.314	1.389
$\Delta OCV_{roscher}$	**−1.054**	**−0.309**	0.859	**−0.006**	**0.557**	**0.391**	**0.697**	**0.527**
$\Delta OCV_{preisach}$	**−1.054**	−0.484	**−0.484**	−3.441	1.366	1.470	1.832	2.026
	P_1 /−	P_2 /−	P_3 /−	P_4 /−	$MAE_{P_{1-4}}$ /−	$MAE_{P_{2-4}}$ /−	$RMSE_{P_{1-4}}$ /−	$RMSE_{P_{2-4}}$ /−
$\Delta h_{direct,dch}$	0.762	0.244	0.076	**0.006**	**0.272**	**0.109**	**0.402**	**0.148**
$\Delta h_{direct,ch}$	**−0.238**	−0.756	−0.924	−0.995	0.728	0.892	0.786	0.897
$\Delta h_{direct,avg}$	0.262	−0.256	−0.424	−0.495	0.359	0.392	0.374	0.404
Δh_{plett0}	**−0.238**	0.244	0.076	**0.006**	0.141	0.109	0.175	0.148
Δh_{plett1}	**−0.238**	**−0.050**	0.076	−0.153	**0.129**	**0.093**	**0.149**	**0.103**
Δh_{huria}	**−0.238**	−0.091	**−0.063**	−0.206	0.150	0.120	0.167	0.135
$\Delta h_{roscher}$	**−0.238**	**−0.063**	0.076	**−0.001**	**0.095**	**0.047**	**0.129**	**0.057**
$\Delta h_{preisach}$	**−0.238**	−0.099	**−0.043**	−0.315	0.174	0.152	0.205	0.192

metrics when P_1 is excluded; (2) the Modified Preisach and the Huria model exhibit increased error metrics when P_1 is excluded, because their drift-induced errors at P_4 become more dominant; (3) the Plett One-State model shows only minor changes between P_1–P_4 and P_2–P_4, as its error at P_1 is similar in magnitude to those at the other points; (4) some models improve when P_1 is excluded because their largest error occurs there irrespective of the magnitude of H_{max}; this is the case for the Plett Zero-State, the Roscher, and the $OCV_{direct,dch}$ model.

Overall, for P_1–P_4, the Plett Zero-State and the Roscher model perform best in terms of ΔOCV_{mod}, with a $MAE_{P_1-P_4} = 0.791$ mV and $RMSE_{P_1-P_4} = 0.905$ mV, and a $MAE_{P_1-P_4} = 0.557$ mV and $RMSE_{P_1-P_4} = 0.697$ mV, respectively. For P_2–P_4, these models remain the best with a $MAE_{P_2-P_4} = 0.704$ mV and $RMSE_{P_2-P_4} = 0.849$ mV for the Plett Zero-State, and a $MAE_{P_2-P_4} = 0.391$ mV and $RMSE_{P_2-P_4} = 0.527$ mV for the Roscher model. The impact of excluding P_1 on ΔOCV_{mod}-based metrics is therefore limited.

A more balanced assessment uses Δh_{mod} from Table 8 for the MAE and RMSE over both P_1–P_4 and P_2–P_4, as it eliminates biases introduced by a variable H_{max}. In this case, only two main tendencies are observed: (1) the $OCV_{direct,ch}$ and the $OCV_{direct,avg}$ model deteriorate when P_1 is excluded because, at this point, they match the measured OCV hysteresis fairly well; (2) all other models improve when restricting the evaluation to P_2–P_4, as the initial offset at P_1, considered a systematic bias related to LFP two-phase transition rather than an effect related to model quality, is removed.

On this normalized basis, i.e. regarding h_{mod}, the Plett One-State and the Roscher model provide the most accurate description of OCV hysteresis. For P_1–P_4, they achieve a $MAE_{P_1-P_4} = 0.129$ and $RMSE_{P_1-P_4} = 0.149$, and a $MAE_{P_1-P_4} = 0.095$ and $RMSE_{P_1-P_4} = 0.129$, respectively. For P_2–P_4, they reach a $MAE_{P_2-P_4} = 0.093$ and $RMSE_{P_2-P_4} = 0.103$ (Plett One-State) and a $MAE_{P_2-P_4} = 0.047$ and $RMSE_{P_2-P_4} = 0.057$ (Roscher). The Roscher model, in particular, improves by around 50 % when P_1 is excluded, as its largest error occurs at that point.

5. Discussion

After presenting the results in Section 4, the following section provides a detailed discussion of the findings. These findings include an analysis of the varying error contributions during each load phase influenced by the magnitude of OCV hysteresis, its associated model accuracy, and ECM accuracy, the identification of model drift, and the evaluation of bias effects, particularly with respect to P_1. Based on this, a ranking of the models in terms of MAE and RMSE of Δh_{mod} and $\Delta V_{OCV_{mod}}$ is derived, yielding the following for OCV hysteresis models with real transitions: Roscher model, Plett One-State model, Huria model, and Modified Preisach model.

Therefore, an error decomposition is elaborated in Section 5.1, while Section 5.2 focuses on the discussion of recuperation- and interpolation-induced drift phenomena described earlier. Subsequently, Section 5.3 presents a sensitivity analysis, and finally, Section 5.4 offers a comprehensive comparison with existing literature, examines under which conditions the reported errors translate into a SOC error, and consolidates these individual discussions in Table 10, which forms the third level of synthesis by combining all benchmark results into recommendations per model. These sections focus on the OCV hysteresis models with real transitions. Thus, apart from Table 10 and if not necessary, the results of the direct OCV hysteresis models with OCV_{dch}, OCV_{avg}, and OCV_{ch}, as well as the Plett Zero-State model, are omitted.

5.1. Decomposition of modeling errors

This section decomposes the model errors to interpret the specific impact of OCV hysteresis modeling under load, building on the overall error and hysteresis trajectory analysis presented in Section 4. Fig. 7 shows the temporal decomposition of errors from the validation profile for the Plett One-State, the Huria, the Roscher, and the Modified Preisach model. In order to do so, Fig. 7(a)–(c) provides an analysis of the input I_{app} that governs the polarization and hysteresis behavior of each modeling approach. This analysis is based on the root mean square (RMS) of I_{app} and the RMS of its time derivative. Both RMS values are computed by binning the respective signals into time-intervals of 10 s, with results smoothed using a Savitzky–Golay filter for improved visibility. The $RMS(I_{app})$ quantifies the amplitude, while $RMS(dI_{app}/dt)$ characterizes the rate of change of I_{app}. Together, these metrics offer insight into how input dynamics affect model performance. The errors $\Delta V_{OCV_{mod}}$, are shown in Fig. 7(d)–(f). They are smoothed similarly to the RMS. In addition to the errors $\Delta V_{OCV_{mod}}$ of the four remaining hysteresis models, the direct OCV model errors $\Delta V_{OCV_{direct,dch}}$ and $\Delta V_{OCV_{direct,ch}}$ are displayed to show the maximum and minimum possible error resulting from the maximum and minimum hysteresis values. The corresponding h_{mod} values for the investigated OCV hysteresis models are displayed in Fig. 7(g)–(i) for each load phase. This extends the error decomposition by providing a visualization of the hysteresis contribution that is free of any meaningful drift-like behavior, which is excited by a direct dependency on or by scaling with H_{max}.

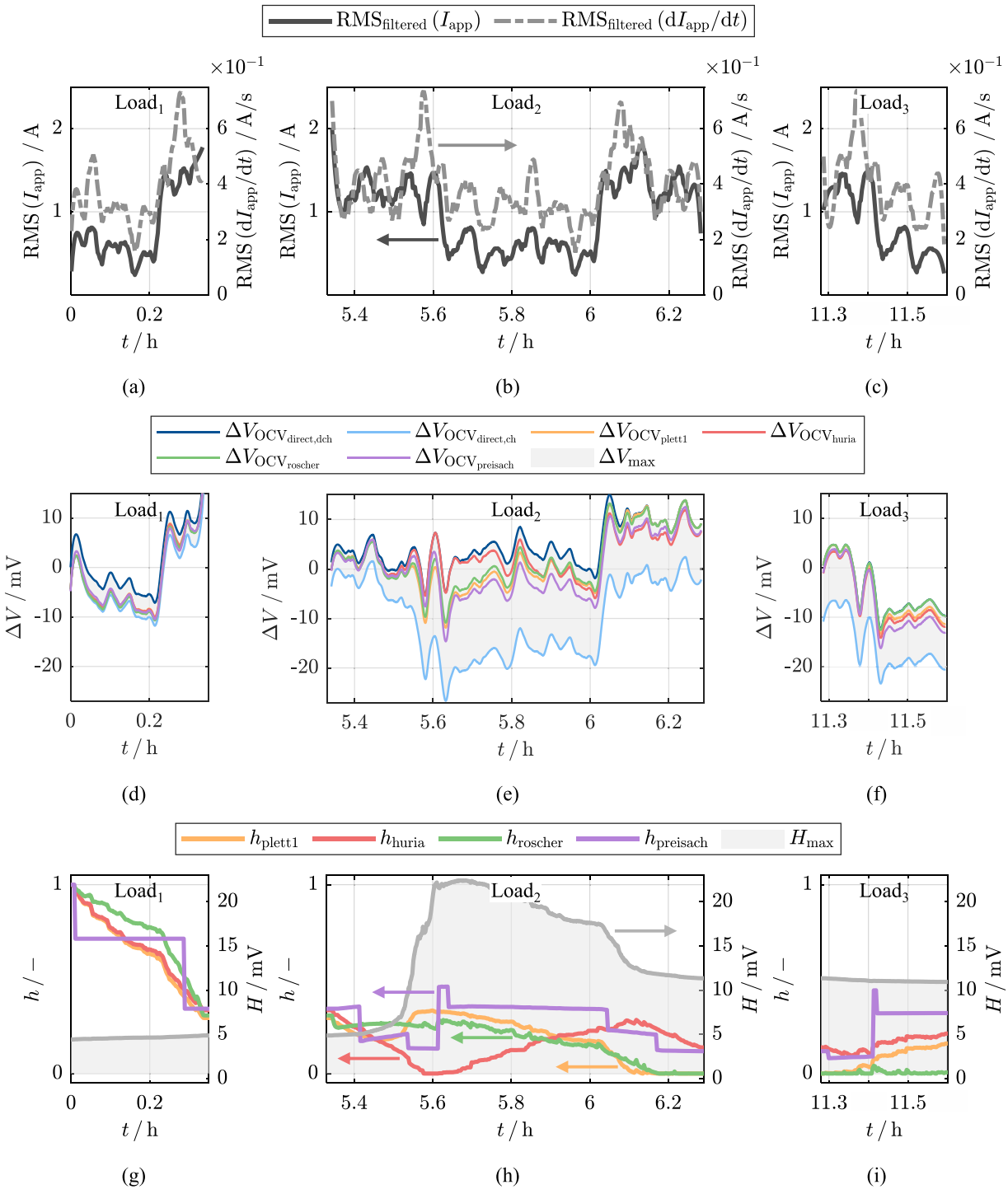


Fig. 7. Error decomposition of the Plett One-State, the Huria, the Roscher, and the Modified Preisach model for the validation profile, showing the input dynamics, resulting errors, and modeled OCV hysteresis across all three load phases. (a)–(c) Smoothened RMS(I_{app}) and RMS(dI_{app}/dt) for all three load phases for analyzing the dynamics of I_{app} regarding its amplitude and rate of change. (d)–(f) Smoothened model errors $\Delta V_{OCV_{mod}}$ for all three load phases. (g)–(i) Corresponding H_{max} and h_{mod} for all three load phases.

Phase Load$_1$. During the phase Load$_1$ (see Fig. 7(a)), RMS(I_{app}) starts below 1 A until t = 0.2 h, after which it rises above 1.5 A. The rate of change, as indicated by RMS(dI_{app}/dt), increases from around 0.3 A/s to a maximum of approximately 0.75 A/s after t = 0.2 h. Thus, both the amplitude and the rate of change rise sharply at this point in time. The corresponding errors (see Fig. 7(d)) are bounded by the direct OCV models based on OCV_{dch} and OCV_{ch}, which represent the maximum extent of the OCV hysteresis. Since H_{max} is limited to approximately 5 mV in this phase (see Fig. 7(g)), the error bandwidth for all hysteresis models does not exceed this value. Besides that, H_{max} and therefore the influence of the holistic OCV hysteresis representation of graphite and LFP is constant, which means that it does not influence the hysteresis

trajectories in any way. Thus, the errors transition correctly from the OCV_{ch} towards the OCV_{dch} boundary. The mean h_{mod} value at P_2 is 0.320, resulting in a negligible change of OCV hysteresis voltage between P_1 and P_2 (2.86 mV on average for all four models). As shown in Table 8, absolute errors for P_2 are less than 0.5 mV across all models, confirming accurate hysteresis modeling in this phase. These aspects already indicate that OCV hysteresis-related errors are not a dominant contributor here. In contrast, the error is strongly affected by input dynamics: as dynamics increase, the cumulative error rises sharply. This shows that errors from the ECM with a series resistance and two RC elements are more significant than those from hysteresis modeling under these conditions.

Phase Load$_2$. In the phase Load$_2$ (see Fig. 7(b)), RMS(I_{app}) remains above 1 A until $t = 5.6$ h, then drops below and rises again above 1 A at $t = 6.0$ h. The rate of change (RMS of the derivative) is around 0.4 A/s, peaking at >0.70 A/s near $t = 5.6$ h and $t = 6.0$ h. The error (see Fig. 7(e)) reflects these dynamics but is also influenced by the trajectory of H_{max} (starting at 5 mV, peaking above 20 mV, ending at 11 mV; see Fig. 7(h)). The error band widens and narrows in accordance with H_{max}, driven by the holistic OCV hysteresis representation of graphite and LFP. Initially, OCV hysteresis has minimal impact due to the low H_{max} and the convergence of h_{mod} towards 0, i.e. OCV_{dch}. During the graphite plateau transition, the error band expands and the error itself diverges for each model, depending on their sensitivity to H_{max} resulting from the holistic OCV hysteresis modeling for graphite and LFP, but also due to drift. The Modified Preisach and the Roscher model scale with H_{max}, while the Plett One-State model is governed by the H_{max} trajectory. The Huria model does not depend on the H_{max} trajectory. Besides the influence of H_{max}, the drift that sets in during this phase, which is accompanied by an increase in dynamics, also plays a role in error decomposition. In particular, the Preisach and the Huria model exhibit drift in this phase, that contributes to the overall error. Distorted by these influences, the precise contribution of each error source is hard to isolate in this region due to overlapping effects. The optimal hysteresis factor likely falls between the direct OCV model with OCV_{dch} and the four hysteresis models, especially when H_{max} is large. As H_{max} stabilizes towards the end of this phase, the models converge again towards the OCV_{dch} error. The average h_{mod} for P_3 is 0.064 for all four models, which corresponds to an average voltage difference of 0.833 mV from P_2 to P_3. In this point-by-point analysis, the OCV hysteresis impact is negligible compared to the overall behavior of $\Delta V_{OCV_{mod}}$. Table 8 confirms that absolute errors for P_3 are less than 0.9 mV, indicating high modeling accuracy. Yet again, input dynamics remain a significant influence on the error progression, with all models showing a rapid absolute error increase (>15 mV) after $t = 6.0$ h due to changes in input dynamics. Generally speaking, for the phase Load$_2$, because the evolution of H_{max} coincides with changes in dynamics, which may also excite drift for some models, it is not possible to decompose these errors to a full extent.

Phase Load$_3$. In the phase Load$_3$ (see Fig. 7(c)), the RMS(I_{app}) remains above 1 A, then falls below after $t = 11.4$ h. The rate of change remains near 0.4 A/s with a peak of 0.75 A/s just before RMS(I_{app}) drops below 1 A. Unlike in phase Load$_2$, H_{max} is constant (11 mV), which allows for clearer separation of error sources as H_{max} does not influence the hysteresis trajectories in any way. Here, drift in h_{mod} is visible for the Plett One-State, the Huria, and the Modified Preisach model (see Fig. 7(i)). The average h_{mod} at P_4 is 0.174, with an absolute error ΔOCV_{mod} below 3.5 mV. This value spreads due to differences resulting from the model drift (see Table 8). While the contribution from this error is higher than for earlier phases, it remains minor relative to the error band between OCV_{dch} and OCV_{ch}. Nevertheless, since models are close to OCV_{dch}, this error contribution is negligible for the overall behavior. Fig. 7(f) shows that error is primarily driven by the ECM with a series resistance and two RC elements, and by input dynamics: the change in load dynamics at $t = 11.4$ h triggers an absolute error increase of about >10 mV for all models.

Summary and implications. Across all load phases, errors from the ECM with a series resistance and two RC elements are dominant when the OCV hysteresis range is narrow, independent of drift or other model errors (phases Load$_1$ and Load$_3$). In the phase Load$_2$, both the load dynamics and the magnitude of H_{max}, and therefore the influence of the holistic OCV hysteresis representation of graphite and LFP, contribute to a more complex error profile. Overall, Table 7 and Fig. 5 demonstrate that the Plett One-State, the Huria, the Roscher, and the Modified Preisach OCV hysteresis model deliver improved accuracy in many cases. These findings have direct implications for the development of cell models for real-world operating conditions. The results indicate that, while advanced OCV hysteresis modeling can enhance accuracy, especially during rest phases, the dominant source of error under dynamic load conditions remains the general accuracy and parameterization of the series resistance and the two RC elements of the ECM. This suggests that, for applications requiring precise voltage prediction under variable loads (such as automotive BMSs), efforts to improve parameterization and identification of the ECM's series resistance and RC elements may yield greater benefits than further refinements in OCV hysteresis modeling alone. Furthermore, the findings indicate that RMS($\mathrm{d}I_{app}/\mathrm{d}t$) appears to play a less dominant role compared to RMS(I_{app}), implying that the errors associated with the ECM with a series resistance and two RC elements are mainly driven by the amplitudes of the input I_{app}. This is particularly evident as this correlates with phases of acceleration or deceleration within the validation profile. The error behavior may depend on the general capabilities of the chosen model under specific loads, as a reduction in RMS(I_{app}) typically leads to, relatively seen, decreased errors, even though the absolute overall error may increase. Additionally, the linear interpolation of parameters of the series resistance and the two RC elements can introduce further errors, especially during rapid changes in load including charge direction changes. Especially the resulting variations in capacitance values of the RC parameters can induce significant changes in the overall error, as they alter the RC elements' saturation behavior. However, errors arising from the interpolation of parameters of the ECM with a series resistance and two RC elements are not further investigated in this work. In addition, the findings highlight the importance of selecting hysteresis models that are robust to changes in H_{max} arising from the holistic OCV hysteresis representation, as well as to drift effects, since these factors continue to impact overall model accuracy, particularly in systems operating across diverse cycling regimes. This also delimits what a validation at higher C-Rates could contribute to the model comparison intended here. The applied current enters the OCV hysteresis models exclusively through the charge throughput, whereas the error under load scales with RMS(I_{app}) through the ECM with a series resistance and two RC elements, which is identical for all models under comparison. An increase in current amplitude would therefore predominantly amplify a shared error contribution and reduce, rather than increase, the resolution of the benchmark with respect to the hysteresis formulations.

5.2. Drift analysis of OCV hysteresis models

After discussing the error decomposition during load phases for the Plett One-State, the Huria, the Roscher, and the Modified Preisach model, the following section examines the drift behavior of each of these OCV hysteresis models. In Sections 3 and 4, the drift behavior of the individual models, including the expected drift-like behavior resulting from direct dependency on or scaling with H_{max}, was described and identified as part of the holistic OCV hysteresis representation of LFP and graphite. In addition, the impact of drift on model errors was briefly highlighted in the previous section. Each model behavior will be revisited in the following. The Plett One-State model exhibits drift-like behavior due to its dependence on H_{max}. The model reveals recuperation-induced drift due to its non-linearity and the charge

direction dependency of the parameters. Furthermore, interpolation-induced drift can arise due to the SOC dependency of the parameters. The Huria model depends directly on OCV_{dch} or OCV_{ch}. With their monotonicity, it does not exhibit drift-like behavior due to the influence of H_{max}. Furthermore, just like the Plett One-State model, it exhibits recuperation-induced drift due to non-linearity and charge-direction-dependent parameterization. Similarly, interpolation-induced drift may also arise due to its parameters' SOC dependency. For the Roscher model, scaling by H_{max} results in drift-like behavior. Due to its linearity, recuperation-induced drift can only occur through charge-direction-dependent parameterization. Interpolation-induced drift may also arise here due to SOC-dependent parameters. Finally, like the Roscher model, the Modified Preisach model exhibits drift-like behavior from scaling with H_{max}. Recuperation-induced drift arises in this model due to the transformation and rest mechanisms, which are partly suppressed by the threshold $\epsilon_{preisach}$. Potentially, an asymmetric weight distribution can also generate recuperation-induced drift. Interpolation-induced drift may result from the SOC dependence of the weights.

As previously described, the drift-like behavior resulting from the direct dependency on or scaling with H_{max} is a desired model property arising from the holistic OCV hysteresis representation. Therefore, it will not be discussed further here. To mitigate the effects of H_{max}, the normalized hysteresis factor h_{mod} is used here.

For the examination of drift behavior, Fig. 8 presents the following metrics of the validation profile with the OCV hysteresis validation points P_1–P_4: Fig. 8(a)–(c) shows the temporal evolution of the net charge balance Q_{net}, the positive charge balance Q_{ch}, and the ratio $|Q_{ch}/Q_{dch}|$ across all three load phases. At the same time, these subfigures display the number of recuperation phases within intervals of 180 s as charge counts. Each load phase can be identified in Fig. 8(d) within the representation of h_{mod} and H_{max} as a function of SOC. The phase $Load_1$ (Fig. 8(a)) is located between $Rest_1$ and $Rest_2$, the phase $Load_2$ (Fig. 8(b)) is located between $Rest_2$ and $Rest_3$, and the phase $Load_3$ (Fig. 8(c)) is located between $Rest_3$ and $Rest_4$. This allows the assessment of recuperation events relative to the progression of h_{mod} over the net charge balance, i.e. the SOC in Fig. 8(d). Additionally, Fig. 8(d) reveals minor OCV hysteresis loops during intense recuperation, characterized by fine, backward-oriented spikes. First, the recuperation-induced drift will be assessed; this is followed by the interpolation-induced drift, before concluding with mitigation strategies.

Assessment of OCV hysteresis drift due to recuperation. Examining Q_{net}, Q_{ch} and $|Q_{ch}/Q_{dch}|$ in Fig. 8(a) for the phase $Load_1$, the net discharge progresses nearly linearly up to $t = 0.2$ h, matching the trends of Q_{ch} and the ratio $|Q_{ch}/Q_{dch}|$. Beyond this time, the net discharge accelerates significantly, showing a corner in Q_{net}. Charge counts confirm more frequent recuperation events before $t = 0.2$ h, on average 13 per 180 s, dropping to 8 per 180 s afterward. This behavior aligns with input dynamics from the previous section, suggesting a higher likelihood of recuperation-induced drift before $t = 0.2$ h. However, Fig. 8(d) shows no recuperation-induced drift in the phase $Load_1$ for any model. This stability may be explained by the model characteristics. The Plett One-State and the Huria model are susceptible to drift due to their non-linearity and charge-direction-dependent parameterization. Yet, during recuperation (charging) near OCV_{ch}, their hysteresis trajectories increase gently with a minimal expected influence from their charge-direction-dependent parameterization, while discharge leads to steep reductions in h_{mod}, again with minimal expected influence from their parameterization, preventing drift. The Modified Preisach model mainly drifts due to extreme recuperation surpassing its threshold $\epsilon_{preisach}$ ($|\Delta SOC| \geq 0.165\,\%$), which does not occur in this phase. The Roscher model, due to its linearity, might only drift due to its charge-direction-dependent parameterization, which is not the case in the phase $Load_1$.

Thus, all four models' h_{mod} shows a clear, monotonically decreasing trend in the phase $Load_1$, reflecting their typical transition behaviors (see Fig. 8(d)).

For the phase $Load_2$ (Fig. 8(b)), Q_{net} and Q_{ch} continue to mirror input dynamics, with low recuperation indicated by steep Q_{net} and flat Q_{ch} as well as the low ratio $|Q_{ch}/Q_{dch}|$ in the beginning of this phase. At $t = 5.6$ h, this trend reverses, with the slope of Q_{net} flattening and the one of Q_{ch} increasing, raising the ratio as well. After $t = 6.0$ h, Q_{net} decreases sharply again, Q_{ch} flattens, and the ratio starts to drop from about 0.15. Charge counts likewise shift: on average 7 per 180 s up to $t = 5.6$ h, 13 between $t = 5.6$ h and $t = 6.0$ h and 6 after $t = 6.0$ h. These patterns indicate a high likelihood of recuperation-induced drift between $t = 5.6$ h and $t = 6.0$ h and correlate with the drift phenomena in Fig. 8(d). The Modified Preisach model drifts only when the preset recuperation threshold is surpassed, as seen near $SOC = 71\,\%$. The Roscher model only shows slight drifts due to its charge-direction-dependent parameterization near $SOC = 71\,\%$, caused by recuperation. The Huria model, however, is governed by OCV_{dch} during net discharge, causing its h_{mod} to rapidly approach zero. Within the critical interval for recuperation-induced drift, the net discharge minimizes the distance to OCV_{dch} resulting in minimal slopes of h_{mod} in discharge direction, whereas recuperation achieves a maximum distance to OCV_{ch} resulting in steep slopes in case of recuperation, thereby enabling drift. This drift may be amplified or attenuated through the additional charge-direction-dependent parameterization. The steepness differences between OCV_{dch} and OCV_{ch} initially compensate any recuperation-induced drift during the change in graphite plateau before $t = 5.6$ h, irrespective of the recuperation rates. From this point onward, increased recuperation combined with $h_{mod} < 0.29$ introduces a strong drift up until $SOC > 66\,\%$. Yet, even with reduced recuperation at $t > 6$ h, the remaining recuperation is still sufficient to sustain drift at least up to $SOC > 61\,\%$ (see Fig. 8(d)). The Plett One-State model reaches similar h_{mod} values but does not drift in this phase. Governed by $H_{max}/2$, which is still visible in the normalized representation, h_{mod} remains stable or increases during increased recuperation due to the trajectory of H_{max} it self, maintaining sufficient distance to boundary curves. Yet again, this drift-like behavior, still visible in h_{mod}, is an intended, meaningful behavior of this model. Unlike the Huria model, the Plett One-State does not use the full distance between OCV_{ch} and OCV_{dch} for determining the transition gradient (i.e. H_{max}); it uses only $H_{max}/2$ combined with OCV_{avg} as baseline, shifting risk of recuperation-induced drift to lower h_{mod} values. At the same time, the charge-direction-dependent parameterization is expected to have a minimal influence on the observed behavior even with strong recuperation. Thus, in this phase, the Plett One-State model is not prone to recuperation-induced drift, unlike the Huria model. After $t = 6.0$ h as H_{max} stabilizes, h_{mod} for the Plett One-State model converges towards zero, but lower recuperation rates and its resilience prevent drift at the end of this phase.

In the phase $Load_3$ (Fig. 8(c)), recuperation rates increase at $t = 11.4$ h based on the known metrics (charge counts, Q_{net}, Q_{ch} and $|Q_{ch}/Q_{dch}|$). Average charge counts rise from 9 to 14 per 180 s after $t = 11.4$ h, peaking at 18 and 17 at the end of this phase. Models are likely to exhibit recuperation-induced drift from $t = 11.4$ h onward, corresponding to $SOC = 52\,\%$ in Fig. 8(d). As before, the Roscher model exhibits only minor drift due to its charge-direction-dependent parameterization. However, it can compensate for this. The Modified Preisach model shows drift only when a recuperation pulse exceeds its threshold around $SOC = 51\,\%$. The Plett One-State and the Huria model begin to drift as h_{mod} of each model approaches zero due to their non-linear slopes, causing transition gradients to diverge between charge and discharge direction. Additionally, the charge-direction-dependent parameterization of both models might have an influence on the observed drift.

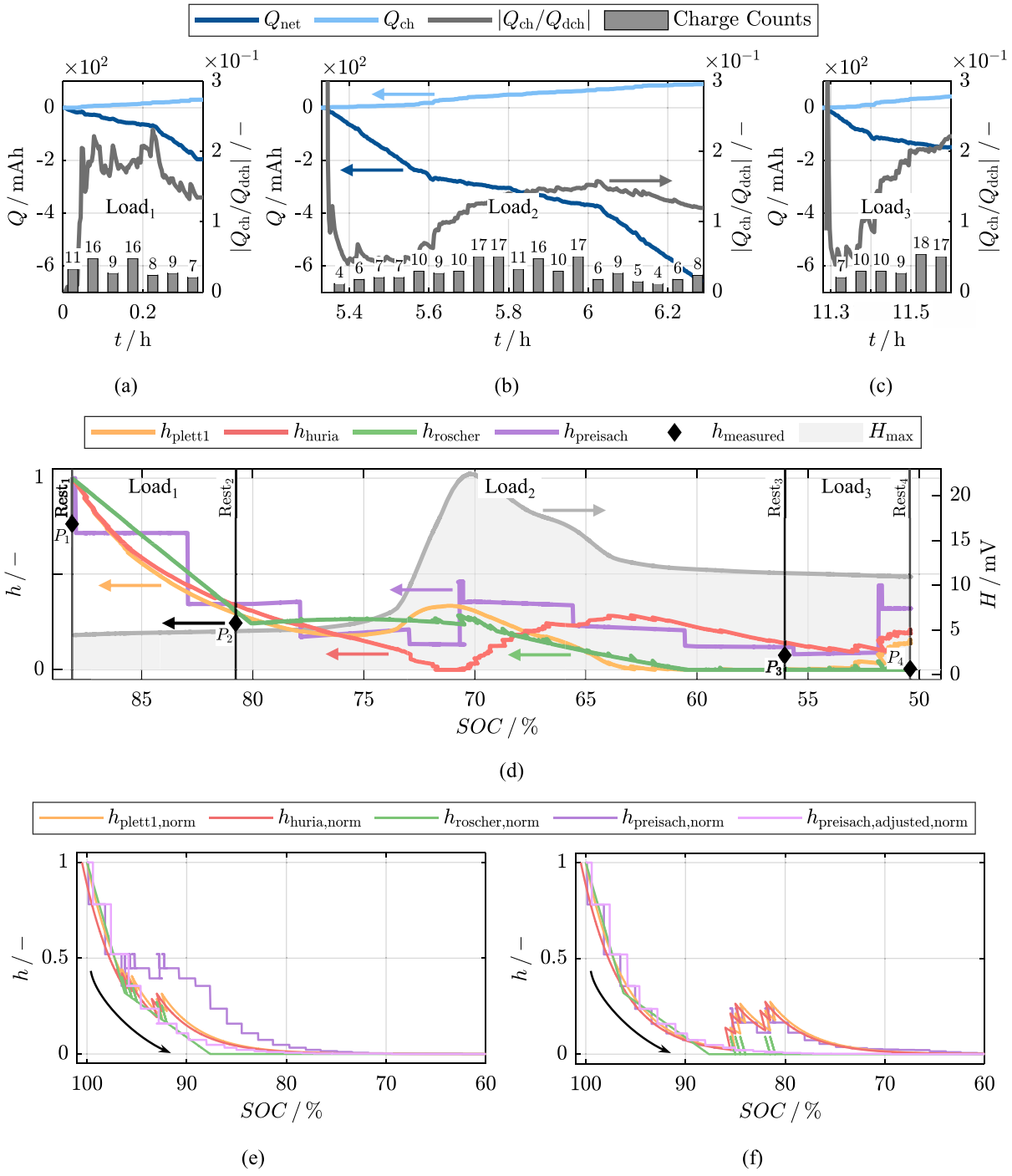


Fig. 8. Analysis of recuperation- and interpolation-induced drift of the Plett One-State, the Huria, the Roscher and the Modified Preisach model for the validation profile, including the OCV hysteresis validation points P_1–P_4, based on the input dynamics for all three load phases, the resulting h_{mod}, and an exemplary synthetic demonstration of recuperation-induced drift sensitivity. (a)–(c) Analysis of the input dynamics regarding the resulting Q_{net}, Q_{ch}, $|Q_{ch}/Q_{dch}|$ as well as charge counts binned over 180 s for all three load phases. (d) Resulting h_{mod} over SOC partly showing recuperation- and interpolation-induced drift. (e)–(f) Synthetic demonstration of the extent of recuperation-induced drift at high h_{mod} and low h_{mod}.

The impact of the charge-direction-dependent parameterization of the Plett One-State, the Huria, and the Roscher model on recuperation-induced drift cannot be directly assessed here, although it is considered to be minor. This will be evaluated in the sensitivity analysis in Section 5.3. The drifting phenomenon is generalized in Fig. 8(e)–(f). It illustrates the recuperation-induced drift likelihood of the individual models, omitting a charge-direction-dependent parameterization: at lower h_{mod} values, the Plett One-State, the Huria, and the Modified Preisach model are more susceptible to drifting compared to higher h_{mod}. For the Modified Preisach model, increasing the threshold in $h_{preisach,adjusted,norm}$ can easily mitigate drift, as shown in Fig. 8, (e)–(f) and discussed further below.

In summary, the Huria model is most prone to recuperation-induced drift, with drift risk increasing at low h_{mod} and under high recuperation rates, followed by the Plett One-State model. The Modified Preisach model may also be prone to recuperation-induced drift depending

on its threshold $\epsilon_{\text{preisach}}$. Since recuperation-induced drift is triggered by changes in charge direction, its extent depends on the rate and magnitude of recuperation events and therefore on the dynamics of the profile. A more aggressive profile is thus expected to increase, not decrease, the differences between the models identified here.

Assessment of OCV hysteresis drift due to interpolation. Besides recuperation-induced drift, the impact of SOC-dependent parameterization on drift is non-negligible. Yet, quantification of interpolation-induced drift is difficult. Nevertheless, this drift can be observed for the Modified Preisach and Roscher model, which are primarily scaled by H_{max} and are thus less influenced by the holistic OCV hysteresis representation of graphite and LFP. Interpolation-induced drift is observable in Fig. 8(d) for the Modified Preisach model, where h_{mod} increases minimally between $SOC = 83\,\%$ and $SOC = 78\,\%$ or between $SOC = 71\,\%$ and $SOC = 61\,\%$ within different switching levels. Similarly, for the Roscher model, h_{mod} flattens or temporarily increases against the expected trend between $SOC = 80\,\%$ and $SOC = 71\,\%$, due to SOC-based interpolation. For the Plett One-State and the Huria model, interpolation-induced drift is harder to distinguish due to their exponential transition trajectories and dependence on OCV major loops or H_{max}, but it can still modulate transition speeds over SOC.

Overall, interpolation-induced drift is most pronounced near graphite plateau transitions, raising questions as to whether it reflects a physical effect or an artifact of overfitting or misfitting arising from SOC-dependent parameterization within holistic OCV hysteresis modeling of graphite and LFP, where OCV hysteresis follows a non-monotonic trajectory. This topic is further examined in the sensitivity analysis in Section 5.3.

Mitigation of OCV hysteresis drift. To the best of the authors' knowledge, drift phenomena in OCV hysteresis, whether caused by recuperation-induced or interpolation-induced effects, have not been systematically addressed in the literature, making direct comparisons impossible. For example, Ma et al. [38] briefly mention the issues of drift near the boundary curves for the Huria and the Plett One-State model, but does not analyze them in detail. Based on the presented drift types and issues, we propose potential mitigation strategies that also help analyze specific aspects of the respective drift types. First, one can revoke SOC- and charge-direction-dependent parameterization. This mitigates interpolation-induced drift through SOC-dependent parameterization and also suppresses and shows the influence of charge-direction-dependent parameterization regarding recuperation-induced drift. Secondly, to directly suppress recuperation-induced drift, we propose introducing a recuperation threshold for switching the hysteresis trajectory, similar to the Modified Preisach model's threshold ($\epsilon_{\text{preisach}} = 0.165$). This approach would prevent trajectory switching for small recuperation events, generally reducing recuperation-induced drift. These strategies provide a simple and pragmatic pathway to mitigate drift and motivate the sensitivity analysis presented in the following section.

5.3. Sensitivity analysis of OCV hysteresis models

To assess the impact of parameter interpolation and recuperation on hysteresis modeling, several implementations of the Plett One-State, the Huria, the Roscher, and the Modified Preisach model are compared. This investigation is motivated by the mitigation strategies described in the previous section, as well as the general idea of investigating the impact of charge-direction-dependent parameterization and SOC-dependent parameterization on modeling results and drift. In the following, the baseline models use their standard implementation with variable parameters across SOC and charge direction (subscript var). The following sensitivities are considered: (1) averaged parameters across SOC and charge direction in order to simultaneously evaluate the impact of charge-direction-dependent parameterization on recuperation-induced drift as well as the overall impact of interpolation-induced drift due to SOC-dependent parameterization (subscript avg); (2) one optimal parameter set for each charge direction valid for all SOCs to evaluate the impact of interpolation-induced drift due to SOC-dependent parameterization and to provide insights regarding parameter over- and misfit (subscript opt); and (3) an extreme case with a maximum threshold suppressing all recuperation effects and using the optimal parameters to provide an approach with fully mitigated recuperation and interpolation-induced drift (subscript ϵ_{max}). The sensitivity for the validation profile is evaluated with respect to the MAE of $\Delta V_{\text{OCV}_{\text{mod}}}$ and Δh_{mod}, computed over P_2–P_4 to mitigate bias from P_1, as described in Section 4.2. The results of the sensitivity analysis are summarized in Table 9 and visualized in Fig. G.12 in Appendix G.

Using averaged parameters improves the MAE for both the overall voltage ($\Delta V_{\text{OCV}_{\text{mod}}}$) and the OCV hysteresis validation points (Δh_{mod}) over P_2–P_4 for all models, compared to the baseline models with standard implementation. This suggests two major points: (1) parameter dependencies on SOC and charge direction can introduce unintended behavior linked to interpolation- and recuperation-induced drift; and (2) excessive fitting to various OCV hysteresis eyes within a holistic OCV hysteresis description for LFP and graphite, particularly near graphite plateau transitions, can lead to overfitting or misfitting. The use of optimal parameters, fitted directly to one OCV hysteresis eye at a representative $SOC_{i,\text{avg,loop}}$, further clarifies this trend. For each model, the optimal parameter set was selected to minimize interpolation and graphite staging effects while achieving best results: for the Plett One-State model, $SOC_{\text{avg,loop}} = 45\,\%$ (charge direction) and $SOC_{\text{avg,loop}} = 55\,\%$ (discharge direction); for the Huria model, $SOC_{\text{avg,loop}} = 55\,\%$ (charge direction) and $SOC_{\text{avg,loop}} = 45\,\%$ (discharge direction); for the Roscher model, $SOC_{\text{avg,loop}} = 45\,\%$ for both directions; and for the Modified Preisach model, $SOC_{\text{avg,loop}} = 55\,\%$ (weights independent of charge direction). This approach (subscript opt) again improved the MAE of Δh_{mod} for all models; for $\Delta V_{\text{OCV}_{\text{mod}}}$ related errors, improvements were observed in some cases, with minor deteriorations in others, but the overall changes remained small. Notably, improvements in Δh_{mod} demonstrate that overfitting and misfitting inherent to the holistic OCV hysteresis representation of LFP and graphite during parameterization, as well as interpolation-induced drift, are significant error sources. These effects primarily arise from parameter extrema near graphite plateau transitions. In contrast, parameters are relatively stable in the high and low lithiation regions. Thus, identifying a single optimal OCV hysteresis eye unaffected by graphite staging is sufficient for practical modeling, reducing both parameterization and measurement effort. The final strategy, suppressing all recuperation effects using an extreme threshold combined with optimal parameters, yielded the lowest errors for all models. This indicates that, in addition to minimizing interpolation and graphite staging effects in the holistic OCV hysteresis representation, either developing models with little recuperation-induced drift like the Roscher model or suppressing recuperation-induced drift further enhances model accuracy. Specifically, the MAE improvements regarding $\Delta V_{\text{OCV}_{\text{mod}}}$ exceeded 0.5 mV for the Plett One-State, the Huria, and the Modified Preisach model, while those regarding Δh_{mod} improved by more than 0.08 for the Modified Preisach and 0.03 for the Plett One-State and the Huria model. The Roscher model, which is little sensitive to recuperation-induced drift due to its charge-direction-dependent parameterization, also showed slight improvement.

In summary, an optimal holistic OCV hysteresis model incorporating hysteresis from both LFP and graphite should avoid parameter interpolation over SOC and, where necessary, maintain charge-direction dependence. Parameter sets should be chosen from regions unaffected by graphite staging, and the impact of recuperation should be limited through thresholding. Future work should focus on optimizing recuperation thresholds and further validating these strategies, particularly for the Plett One-State and the Huria model.

Table 9
Sensitivity of $\Delta V_{OCV_{mod}}$ and Δh_{mod} of the OCV hysteresis models for the validation profile with respect to parameterization. Δh_{mod} is evaluated only over P_2–P_4 due to bias introduced by the offset at P_1.

	MAE_{var} /mV	MAE_{avg} /mV	MAE_{opt} /mV	$MAE_{\epsilon_{max}}$ /mV
$\Delta V_{OCV_{plett1}}$	2.096	2.088	2.016	1.446
$\Delta V_{OCV_{huria}}$	2.447	2.187	2.197	1.453
$\Delta V_{OCV_{roscher}}$	1.585	1.497	1.650	1.413
$\Delta V_{OCV_{preisach}}$	2.831	2.801	2.656	1.457
	$MAE_{P_{2-4},var}$ /–	$MAE_{P_{2-4},avg}$ /–	$MAE_{P_{2-4},opt}$ /–	$MAE_{P_{2-4},\epsilon_{max}}$ /–
Δh_{plett1}	0.093	0.091	0.074	0.043
Δh_{huria}	0.120	0.082	0.079	0.047
$\Delta h_{roscher}$	0.047	0.028	0.019	0.012
$\Delta h_{preisach}$	0.152	0.140	0.117	0.029

5.4. Comprehensive discussion of modeling results

Finally, the results for the Plett One-State, the Huria, the Roscher, and the Modified Preisach model obtained in this study are compared with those reported in literature, followed by a discussion of the conditions under which the reported errors become relevant for SOC estimation and by a final evaluation. All approaches from literature presented here follow the holistic OCV hysteresis representation of LFP and graphite to ensure comparability. Models lacking dedicated simulation of OCV hysteresis trajectories are intentionally omitted, as their performance is well-established in previous research. Given the diversity of prior studies, including differences in implementation, validation protocols, and cell chemistries, this comparison focuses on the original references for the Huria and the Roscher model by Huria et al. [18] and Roscher and Sauer [19]. For the Plett One-State model, results by Hu et al. [37] are considered, as the original publication by Plett [17] uses a cell with $LiMn_2O_4$ cathodes. The Modified Preisach model is compared using insights from Venegas et al. [10], while Ma et al. [38] is included for its comparative analysis of the first three models under varying conditions. With validation by a real driving profile, including OCV hysteresis validation points, drift analysis, error decomposition, and an introduction of a Modified Preisach model, this work enables the evaluation of OCV hysteresis model accuracy under both load and rest phases. Thus, the following review of the literature highlights the distinct contributions and expansions of this work compared to previous publications. Unless otherwise stated, this section refers to the baseline implementation of each model, without any mitigation strategies for drift.

Plett One-State model. As noted, direct quantitative comparison with literature is possible only to a limited extent and primarily yields qualitative insights. Regarding the Plett One-State model, Hu et al. [37] evaluated several empirical models, including the Plett One-State OCV hysteresis model and an ECM with a series resistance and two RC elements, using a LFP high-power 18650 cell (1.1 Ah, former A123, now LithiumWerks), which is expected to be similar to the cell used in this study. Their validation employed both the federal urban driving schedule (FUDS) and dynamic stress test (DST) profiles, with parameters identified separately for three temperatures (10 °C, 22 °C, and 35 °C). Averaged over these temperatures, their model achieved an RMSE of approximately 5 mV for both protocols. Given that the FUDS profile represents a real driving profile and includes brief rest phases, it is most comparable to the validation approach in this work. Herein, the baseline Plett One-State model achieved an RMSE of 7.437 mV for the load phases only, and 3.252 mV overall, demonstrating strong agreement with the results by Hu et al. [37]. Ma et al. [38] also evaluated the Plett One-State model by combining it with an ECM with a series resistance and one RC element for a 1.1 Ah LFP 18650 cell. Further cell specifics were not provided. Validation was performed using both DST and FUDS profiles; however, only the MAE for simulated voltage of the DST profile is reported, yielding 11.0 mV. The FUDS results are presented only for SOC estimation with an EKF. Due to the less dynamic and more staged nature of the DST, it is less comparable to the investigated validation profile in this work, where the Plett One-State model achieved an overall MAE of 2.096 mV and a load-phase MAE of 6.144 mV. In summary, despite differences in experimental setups and reporting, the error magnitudes and trends observed for the Plett One-State model in this work are in good qualitative and quantitative agreement with previously published results.

Huria model. The Huria model, as introduced in the original publication by Huria et al. [18], is paired with an ECM with a series resistance and two RC elements, an approach highly comparable to that employed in this study. The original work uses a 4.4 Ah high-power cell of an unspecified manufacturer and validates the model using a real driving profile, but only in conjunction with an EKF. This complicates direct comparison, as EKF corrections influence the voltage error and are not present in the here presented open-loop analysis. Other studies, such as by Nejad et al. [59], which also applies the Huria OCV hysteresis model with an ECM with a series resistance and two RC elements, also do not provide adequate open-loop data for a meaningful comparison. Thus, only the publication by Ma et al. [38], which reports both model (a series resistance and one RC element) and cell specifications (1.1 Ah LFP 18650), serves as a suitable reference. Yet again, the DST profile, is reported to have an MAE of 10.8 mV for their Huria model. In contrast, for the baseline implementation of the Huria model in this work, an MAE of 2.447 mV over the complete validation profile and of 5.593 mV under load conditions is achieved. These results indicate that the Huria and the Plett One-State model in this study deliver a comparable performance, thus proving their validity. Yet, both substantially outperform the MAE values reported in Ma et al. [38]. However, due to differences in validation protocols and reporting, these comparisons remain qualitative rather than quantitative.

Roscher model. In the original publication of the Roscher model by Roscher and Sauer [19], a high-power cell is modeled using an ECM with a series resistance and one RC element. The capacity and format of the investigated cell are not specified. Based on the C-Rate and current scaling presented, the cell capacity is estimated to be around 2 Ah. However, Roscher and Sauer [19] emphasize closed-loop SOC accuracy, making direct comparison with the baseline model's open-loop voltage error infeasible. The same limitation applies, e.g., to the work by Jöst et al. [4]. As a result, only the study by Ma et al. [38], which reports both model configuration and cell specifications (see previous paragraphs), is used as a reference. For the DST profile, the authors report an MAE of 3.5 mV for the Roscher model. In this study, the Roscher model with baseline implementation achieves an MAE of 1.585 mV for the complete profile and 5.895 mV under load conditions. This suggests a consistent ranking of model performance between our study and that of Ma et al. [38], though the MAE values here are substantially lower. As with previous comparisons, these error levels should be interpreted qualitatively due to differences in testing protocols and parameter identification methods.

Modified Preisach model. The newly introduced Modified Preisach model developed in this work is compared to similar approaches in the literature. Although not identical, comparable results are presented by Venegas et al. [10], who employ a Preisach model based on the Everett function for OCV hysteresis modeling. Their implementation uses an ECM with a series resistance and one RC element, and, as described in Section 3.1, models the entire OCV as an Everett function of the Preisach model. Venegas et al. [10] validate their approach using both open-loop and EKF-based methods; for comparison, the open-loop validation is most relevant here. They utilize the highway fuel economy test (HWFET) profile, repeated five times and characterized by minimal rest phases. A MAPE of 0.401 % is reported. In this study,

Table 10
Summarization of findings and recommendations for modeling OCV hysteresis in LFP graphite cells, condensing the benchmark results of Sections 4 and 5 into a comparative assessment and a suggested application per model. Operations per time step refer to the hysteresis sub-model only, excluding the shared ECM, and are derived analytically from the model equations (see Appendix H). For the Modified Preisach model, the worst case with hysteron switching is reported.

	Parameterization effort	Operations per time step	Model simplicity	Model accuracy	Drift & noise robustness	Observer & filter compatibility	Suggested application
Direct OCV	↓	0	↑	↘	↑	↑	Continuous charge/discharge
Plett Zero-State	↓	3	↑	↗	↓	↑	Continuous charge/discharge
Plett One-State	↘	12 and 1 exponential	↗	↑	↘	↑	Without drift mitigation only FORCs
Huria	↘	11 and 1 division	↗	↗	↘	↗	Without drift mitigation only FORCs
Roscher	↗	17	↗	↑	↑	↗	Fully applicable to drive cycles
Modified Preisach	↑	102	↘	↗	↗	↘	Without drift mitigation only FORCs

Qualitative rating of the respective attribute: low: ↓, medium-low: ↘, medium-high: ↗, high: ↑.

the baseline Modified Preisach model achieves a MAPE of 0.194 % under load and 0.086 % for the complete validation profile. While the models differ in key aspects, including ECM structure and Preisach model design, the results are qualitatively comparable. Notably, the model developed here demonstrates superior performance compared to the results reported by Venegas et al. [10].

Relevance of the reported errors for SOC estimation. From a BMS perspective, the quantity of interest is the SOC error caused by OCV hysteresis rather than the voltage error itself. In the framework of Section 3.4, the SOC follows from Coulomb counting (Eq. (57)) and is therefore identical for all models under comparison, so that no SOC error can arise from the hysteresis model in open loop. OCV hysteresis affects the SOC exclusively through a voltage-based correction, that is, when the SOC is recalibrated from a relaxed OCV or corrected by an observer or filter. In both cases, an OCV error (ΔOCV, i.e. through OCV hysteresis) is converted into a SOC error (ΔSOC) through the local slope of the reference OCV,

$$\Delta SOC = \frac{\Delta OCV}{\left|\mathrm{d}OCV_{\mathrm{ref}}/\mathrm{d}SOC\right|}, \tag{60}$$

where the same derivative constitutes the SOC-relevant entry of the output Jacobian of the ECM and thus governs the gain assigned to the voltage measurement in a filter-based correction. A lookup-based inversion and a filter-based correction therefore lose their leverage simultaneously as the major loops flatten. The condition under which an improved OCV hysteresis description improves the SOC is consequently set by $\left|\mathrm{d}OCV_{\mathrm{ref}}/\mathrm{d}SOC\right|$ at the operating point and not by the magnitude of the hysteresis itself.

For the cell and the validation profile investigated here, this distinguishes two regimes. In the flat regions, in which the OCV hysteresis validation points P_1–P_4 are located, the slope of the major loops is <0.2 mV per % SOC, so that the prevailing maximum hysteresis of $H_{\max} \approx 11$ mV in the lower plateau corresponds to a SOC interval >50 %. In this regime, the inversion of Eq. (60) is ill-conditioned. A SOC error evaluated in this regime would therefore characterize the conditioning of the inversion rather than the hysteresis models, and would not discriminate between them. Around the graphite plateau transition, in contrast, the major loops are steeper, so that the corresponding SOC interval narrows despite the larger $H_{\max}$ in this region. This is the regime in which the differences between the hysteresis models identified in Section 4.2 become relevant for SOC estimation. The validation profile traverses this region under load, where hysteresis and polarization cannot be separated (Section 5.1), so that no relaxed validation point and hence no open-loop SOC error is available there either.

Consequently, the accuracy differences reported in Tables 7 and 8 are relevant for SOC estimation at those operating points at which the major loops carry SOC information, whereas in the flat regions the SOC necessarily rests on Coulomb counting and the benefit of hysteresis modeling lies in the predicted terminal voltage itself, which is used for power capability and cell voltage limit management. A quantification of the resulting closed-loop SOC error requires an observability and convergence analysis of the respective observer or filter and is beyond the scope of this open-loop benchmark, as outlined in Section 6.

Table 10 summarizes the results derived in this work for all models, focusing on the baseline implementation including drift phenomena, and provides final recommendations for each modeling approach beyond the accuracy measures discussed here. These recommendations additionally consider parameterization effort, model simplicity, drift and noise robustness, and observer/filter compatibility, and conclude with a suggested application for each model. They further consider the computational structure of a single time step, which is derived analytically from the model equations of Section 3.2 and reported in Appendix H together with the interpolation effort per time step. Two properties are relevant beyond the operation count: the Plett One-State model requires an exponential function in every time step (Eq. (17)), and the Huria model in its present discretization requires a division by $SOC_i - SOC_{i-1}$ (Eqs. (22) and (23)), which requires special numerical handling for small increments, whereas the remaining models rely on multiply-accumulate operations, comparisons, and saturation only. A quantification of execution time and memory occupation on a specific automotive MCU is not attempted.

Together with Tables 4 and 5, Table 10 allows the selection of an OCV hysteresis model to be traced from the literature landscape through the model formulation to the benchmark results without recourse to the detailed discussion.

6. Conclusion

A comprehensive review and benchmark of empirical OCV hysteresis models was performed. All measurements and simulations are conducted on a LithiumWerks ANR26650m1b LFP graphite cell. A large BMW i4 eDrive40 fleet dataset (>75,000 vehicles, >20,000,000 charging events) is analyzed to derive driving behavior with a realistic hysteresis trajectory. Based on this, a real driving profile is augmented by rest phases to obtain a validation profile with distinct OCV hysteresis validation points between OCV_{ch} and OCV_{dch}. Beyond accuracy, the models are characterized with respect to their structural properties for embedded state estimation. All approaches investigated here rely on elementary operations per time step, with only two models requiring an exponential function or a division. Error decomposition on the validation profile shows that, under dynamic load, the dominant contribution to voltage error originates from the ECM with a series resistance and two RC elements, whereas hysteresis modeling becomes decisive during rest phases. All models under investigation that describe a real hysteresis trajectory adopt a holistic OCV hysteresis representation of

both LFP and graphite contributions. Across the validation profile, the best overall accuracy is achieved by models that reliably converge to OCV_{dch} without drift, with the Roscher model combining highest accuracy, drift robustness, and moderate parameterization effort. The novel Modified Preisach model achieves comparable hysteresis accuracy at higher computational and parameterization cost. It avoids the complexity of Everett functions and loop-orientation issues, yielding a generalizable description of major and minor loops in separated form. Thus, it provides a promising basis for future extensions.

Previous studies have not fully analyzed or compared the fundamental behavior of OCV hysteresis models. A central result is the quantitative investigation of OCV hysteresis model drift. Two distinct mechanisms are identified: (i) recuperation-induced drift, arising from frequent charge direction changes that drive models with non-linear behavior combined with a charge-direction-dependent parameterization away from consistent trajectories; and (ii) interpolation-induced drift, caused by SOC-dependent parameters influenced by the holistic OCV hysteresis representation of graphite and LFP, where interpolation leads to local over- or underestimation of OCV hysteresis. The Roscher model is most robust against recuperation-induced drift due to its linear, integral structure, despite having a charge-direction-dependent parameterization, whereas the Plett One-State, the Huria, and the Modified Preisach model require mitigation. The sensitivity analysis demonstrates that (i) avoiding SOC-dependent interpolation, (ii) using a single optimal minor loop to minimize the influence of graphite plateau transitions, and (iii) mitigating drift via recuperation thresholds can significantly reduce parameterization effort and drift while preserving accuracy - a key insight for future BMS implementations aiming to minimize measurement overhead.

This comprehensive analysis establishes a solid foundation for future research, enabling meaningful application of advanced observer- and filter-based state estimation methods without inheriting error sources from open-loop OCV hysteresis models.

Based on these results, the following recommendations can be made:

- For continuous charge or discharge profiles, direct OCV methods or the Plett Zero-State model are sufficient.
- For modeling OCV hysteresis trajectories of a real driving profile, the Roscher model demonstrated the best performance and required no adaptation for such conditions.
- For models prone to recuperation-induced drift (Plett One-State, Huria, and Modified Preisach), introducing a threshold mechanism for recuperation significantly improves performance for real driving profiles. With this mitigation, any of these models is suitable for such open-loop simulation.
- For observer- and filter-based approaches that require model differentiation, the Plett One-State and the Huria model may be preferable, as they are already formulated using differential equations.

These recommendations are intended to guide model selection and implementation for a range of applications and highlight areas where further methodological development is required. With regard to observer and filter applications, future work should address challenges related to the differentiation of OCV hysteresis trajectories, arising from model design, parameterization, and changes in charge direction that lead to abrupt changes in trajectory slope. All of these factors introduce discontinuities in the model's derivatives, which can adversely affect the stability and performance of observers and filters. Generally, for such applications combined with OCV hysteresis modeling, an investigation of observability, robustness against different error types, and convergence behavior is needed. In addition to the accuracy gains achieved through OCV hysteresis modeling, such observer and filter applications can dynamically compensate errors arising from the ECM with a series resistance and two RC elements in response to changing operating conditions, which have been highlighted in this work.

Finally, extending the validation of holistic OCV hysteresis modeling of graphite and LFP to a broader range of temperatures, including low-temperature driving cycles, to C-Rates beyond those covered in this work, as well as to further real driving profiles and to LFP graphite cells of different capacity and housing format, will be essential to ensure generalization and robustness of these modeling strategies.

Beyond the model layer, the structural assessment provided characterizes the models but does not replace an implementation study. Automatic code generation, fixed-point scaling, and the measurement of single-step execution time and worst-case execution time (WCET) on representative automotive MCUs remain subject to future work and are required before quantitative statements on the real-time behavior of these models in series BMS software can be made.

Overall, the results of this review and benchmark of OCV hysteresis models for LFP graphite cells offer a solid basis for future investigations in combination with observers and filters and point to simple, practical drift-mitigation strategies that are readily transferable to automotive BMS software.

CRediT authorship contribution statement

Valentin Ludwig Elender: Writing – original draft, Visualization, Validation, Methodology, Investigation, Formal analysis, Conceptualization. **Sebastian Ludwig:** Writing – review & editing, Supervision, Conceptualization. **Yannis Horstmann:** Methodology, Conceptualization. **Simon Erhard:** Writing – review & editing, Supervision. **Jan Philipp Schmidt:** Writing – review & editing, Supervision.

Declaration of generative AI and AI-assisted technologies in the manuscript preparation process

During the preparation of this work, the authors used large language models (LLMs), including ChatGPT (OpenAI) and Claude (Anthropic), to support code development and debugging, as well as manuscript rewriting, language improvement, review, and editing. All AI-assisted outputs were critically reviewed, verified, and revised by the authors, who take full responsibility for the content of the final article.

Declaration of competing interest

The authors declare the following financial interests/personal relationships which may be considered as potential competing interests: Valentin Elender reports financial support was provided by BMW Group. Sebastian Ludwig reports financial support was provided by BMW Group. Yannis Horstmann reports financial support was provided by BMW Group. Simon Erhard reports financial support was provided by BMW Group. Jan Philipp Schmidt reports financial support was provided by University of Bayreuth. Valentin Elender reports a relationship with BMW Group that includes: employment. Sebastian Ludwig reports a relationship with BMW Group that includes: employment. Yannis Horstmann reports a relationship with BMW Group that includes: employment. Simon Erhard reports a relationship with BMW Group that includes: employment. Jan Philipp Schmidt reports a relationship with University of Bayreuth that includes: employment. If there are other authors, they declare that they have no known competing financial interests or personal relationships that could have appeared to influence the work reported in this paper.

Acknowledgments

The authors gratefully acknowledge the financial support of the BMW Group. This work was conducted in collaboration with the Chair of Systems Engineering for Electrical Energy Storage at the University of Bayreuth.

Appendix A. Terminology of major loops, minor loops and FORCs

See Fig. A.9.

Appendix B. Additional information on the Plett One-State OCV hysteresis model

The discrete Plett One-State model is derived in Section 3.2, including the interpretation and DOF of its parameters and the overall OCV composition. Its properties regarding observer- and filter-readiness, interpretation as a state, drift tendency, and limiting between major loops during parameterization and simulation have been addressed. Additional details, partly shown in Table 5, are summarized below.

Time forwarding. In the Plett One-State model, OCV hysteresis is obtained by Coulomb counting (see Section 3.3). Given the applied current $I_{i,\mathrm{app}}$ at time t_i, the current maximum hysteresis $H_{i,\max}$, and the present hysteresis $h_{i,\mathrm{plett1,lit}}$, the upcoming hysteresis $h_{i+1,\mathrm{plett1,lit}}$ can be predicted, treating it as a model state variable. This is reflected in the overall OCV expression in Eq. (19).

Loop asymmetry. Because $\gamma_{i,\mathrm{ch}}$ and $\gamma_{i,\mathrm{dch}}$ are parameterized separately for charge and discharge, asymmetric minor loop shapes can be represented. Moreover, the dependence of $H_{i,\max}$ on SOC due to the holistic OCV hysteresis representation of LFP and graphite in the model equations introduces additional loop asymmetry during parameterization. In general, during simulation, asymmetries arise from the charge-direction-dependent implementation of $\gamma_{i,\mathrm{ch}}$ and $\gamma_{i,\mathrm{dch}}$, as well as from SOC-dependent variations of the governing $H_{i,\max}$ and all model parameters, which are derived from the holistic OCV hysteresis representation.

Parameterization. Dependencies of model parameters on C-Rate and temperature are neglected. The parameters $\gamma_{i,\mathrm{ch}}$ and $\gamma_{i,\mathrm{dch}}$ are optimized for each minor loop using Eqs. (6), (7), and (8) and the associated parameterization procedure. Since parameterization and analysis are performed in normalized form for comparability, Eq. (17) is reformulated as

$$h_{i,\mathrm{plett1}} = \frac{h_{i,\mathrm{plett1,lit}} + OCV_{i,\mathrm{avg}} - OCV_{i,\mathrm{dch}}}{OCV_{i,\mathrm{ch}} - OCV_{i,\mathrm{dch}}}. \tag{B.1}$$

Yet, since h_{measured} used for parameterization is derived from the holistic OCV hysteresis representation of graphite and LFP, the contributions of each electrode may vary for different values of $SOC_{i,\mathrm{avg,loop}}$ during parameterization. After fitting the parameters for each minor loop, they are linearly interpolated and extrapolated by clipping to form charge-direction-dependent lookup tables at SOC values $0\,\%, 10\,\%, 20\,\%, \ldots, 100\,\%$. The resulting MAE according to Eq. (9) is $\mathrm{MAE_{fit}} = 0.065$, corresponding to an average deviation of 6.5 % over all $N_{\mathrm{loop}} \cdot n_{\mathrm{loop}}$ measured hysteresis data points for the Plett One-State model.

Appendix C. Additional information on the Huria OCV hysteresis model and comparison to the Plett One-State model

The discrete Huria model is derived in Section 3.2, including the interpretation and DOF of its parameters and its overall OCV composition. Its properties regarding observer- and filter-readiness, interpretation as a state, drift tendency, and limiting between major loops during parameterization and simulation have been discussed. Additional details, partly included in Table 5, as well as a comparison with the Plett One-State model, are provided below.

Time forwarding. The Huria model can predict $OCV_{i+1,\mathrm{huria}}$, including hysteresis, using Coulomb counting (see Section 3.3) with the applied current $I_{i,\mathrm{app}}$, the current value $OCV_{i,\mathrm{huria}}$ and its derivative, as well as the current major loops and their derivatives at time t_i (see Eqs. (22)–(29)). This predictive capability is reflected in the overall OCV formulation in Eq. (27).

Loop asymmetry. Similar to the Plett One-State model, the Huria model can represent asymmetric minor loop behavior through separate parameterization of $k_{i,\mathrm{ch}}$ and $k_{i,\mathrm{dch}}$. Additionally, the presence of $OCV_{i,\mathrm{ch}}$ and $OCV_{i,\mathrm{dch}}$ in Eqs. (25) and (26), both varying with SOC, introduces further loop asymmetry during parameterization. In simulation, asymmetries result from the charge-direction-dependent implementation of $k_{i,\mathrm{ch}}$ and $k_{i,\mathrm{dch}}$, as well as from SOC-dependent variations of the model's governing major loops and its parameters. Yet again, the holistic OCV hysteresis representation of graphite and LFP therefore indirectly influences both parameterization and simulation.

Parameterization. Dependencies of model parameters on temperature and C-Rate are neglected. As for the Plett One-State model, the parameters $k_{i,\mathrm{ch}}$ and $k_{i,\mathrm{dch}}$ are optimized for each minor loop using Eqs. (6), (7), and (8) and the associated procedure. Since parameterization and analysis are performed in normalized form, Eqs. (29), (28), and (27) are combined into

$$h_{i,\mathrm{huria}} = \frac{OCV_{i,\mathrm{huria}} - OCV_{i,\mathrm{dch}}}{OCV_{i,\mathrm{ch}} - OCV_{i,\mathrm{dch}}}. \tag{C.1}$$

Yet, since h_{measured} used for parameterization is derived from the holistic OCV hysteresis representation of graphite and LFP, the contributions of each electrode may vary for different values of $SOC_{i,\mathrm{avg,loop}}$ during parameterization. After fitting, the parameters are linearly interpolated and extrapolated by clipping to construct a charge-direction-dependent lookup table at the above mentioned SOC values. The resulting $\mathrm{MAE_{fit}}$, computed using Eq. (9), is 0.054, i.e., an average deviation of 5.4 % over all $N_{\mathrm{loop}} \cdot n_{\mathrm{loop}}$ hysteresis data points for the Huria model.

Comparison to the Plett One-State model. The relationship between the Plett One-State and the Huria model is clarified by comparing the underlying differential equations (Eq. (14) and (20) or (21)).

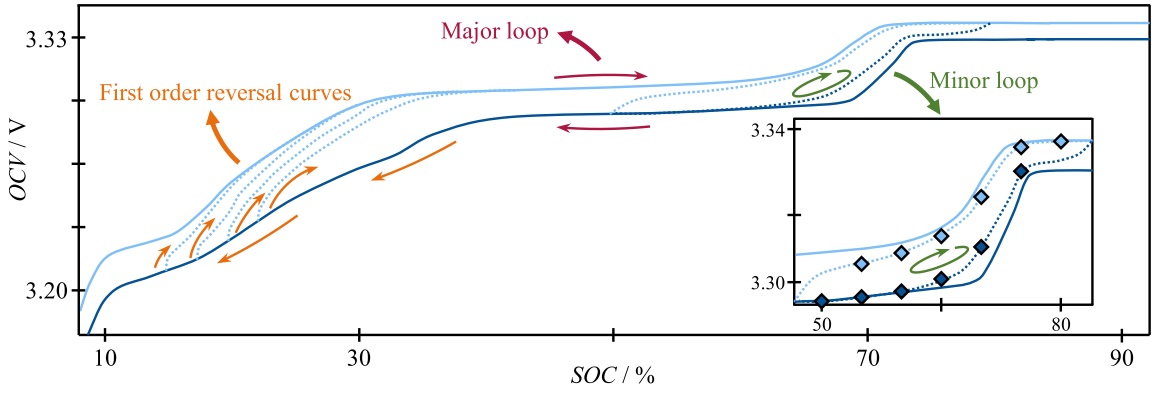


Fig. A.9. Differentiation between major loops (red), minor loops (green), and FORCs (orange) regarding OCV hysteresis in LFP graphite cells. (For interpretation of the references to colour in this figure legend, the reader is referred to the web version of this article.)

For simplicity, only the charge direction is considered in a discrete formulation; the discharge case is analogous. Using Eq. (15), Eq. (14) can be rewritten as

$$\left.\frac{\mathrm{d}OCV_{i,\mathrm{plett1}}}{\mathrm{d}SOC_i}\right|_{\frac{\mathrm{d}SOC_i}{\mathrm{d}t}\geq 0} = \frac{\mathrm{d}OCV_{i,\mathrm{avg}}}{\mathrm{d}SOC_i} + \gamma_i \left[OCV_{i,\mathrm{ch}} - OCV_{i,\mathrm{plett1}}\right], \tag{C.2}$$

whereas Eq. (20) yields

$$\left.\frac{\mathrm{d}OCV_{i,\mathrm{huria}}}{\mathrm{d}SOC_i}\right|_{\frac{\mathrm{d}SOC_i}{\mathrm{d}t}\geq 0} = \frac{\mathrm{d}OCV_{i,\mathrm{ch}}}{\mathrm{d}SOC_i} + k_i \left[OCV_{i,\mathrm{ch}} - OCV_{i,\mathrm{huria}}\right]. \tag{C.3}$$

These formulations show that the models differ primarily in how the OCV derivative with respect to SOC is treated: one uses the major loop OCVs (OCV_{ch} or OCV_{dch}) directly as a reference, whereas the other one uses OCV_{avg} as reference.

Appendix D. Additional information on the Roscher OCV hysteresis model

The discrete Roscher model is derived in Section 3.2, including the interpretation and DOF of its parameters and its overall OCV composition. Its properties with respect to observer- and filter-readiness, interpretation as a state, drift tendency, and limiting between major loops during parameterization and simulation have been discussed. Additional details, partly included in Table 5, are summarized below.

Time forwarding. The Roscher model can also predict the next hysteresis value $h_{i+1,\mathrm{roscher}}$ via Coulomb counting (see Section 3.3) using the applied current $I_{i,\mathrm{app}}$ and the model parameters (see Eqs. (30), (31), and (32)). This predictive behavior is reflected in the overall OCV expression in Eq. (33).

Loop asymmetry. The Roscher model can represent asymmetric minor loop behavior through charge-direction-dependent slopes m_i. Although $\upsilon_{i,1}$ is independent of charge direction, the m_i's modify the transition trajectories asymmetrically. Since the model is formulated directly in normalized form, $h_{i+1,\mathrm{roscher}}$, no additional loop asymmetries are introduced by major loop variations with SOC in the model equations during parameterization. In simulation, asymmetries arise from charge-direction-dependent slopes m_i, from SOC-dependent variations of all parameters, and from scaling with $H_{i,\max}$, which incorporates the holistic OCV hysteresis representation of LFP and graphite.

Parameterization. Dependencies of parameters on temperature or C-Rate are neglected. As with the other models, the parameters $\upsilon_{i,1}$, $m_{i,\mathrm{ch},1}$, $m_{i,\mathrm{dch},1}$, $m_{i,\mathrm{ch},2}$, and $m_{i,\mathrm{dch},2}$ are optimized according to their DOF using Eqs. (6), (7), and (8) and the associated procedure for each minor loop. Since the Roscher model is already formulated in normalized form through Eqs. (30), (31), and (32), no additional transformation is required. Yet, since h_{measured} used for parameterization is derived from the holistic OCV hysteresis representation of graphite and LFP, the contributions of each electrode may vary for different values of $SOC_{i,\mathrm{avg,loop}}$ during parameterization. After fitting, parameters are linearly interpolated and extrapolated by clipping to build a charge-direction-dependent lookup table at the above mentioned SOC values. According to Eq. (9), the optimization yields $\mathrm{MAE}_{\mathrm{fit}} = 0.031$, i.e., an average deviation of 3.1 % over all $N_{\mathrm{loop}} \cdot n_{\mathrm{loop}}$ measured hysteresis data points for the Roscher model.

Appendix E. Additional information on the modified Preisach OCV hysteresis model

The discrete Modified Preisach model is derived in Section 3.2, including the interpretation and DOF of its parameters and its overall OCV composition. Its properties regarding observer- and filter-readiness, interpretation as a state, drift tendency, and limiting between major loops during parameterization and simulation have been addressed. Additional details, partly shown in Table 5, are summarized below.

Time forwarding. In its current implementation, the Modified Preisach model does not predict the future hysteresis $h_{i+1,\mathrm{preisach,lit}}$, because hysteresis is evaluated based on SOC_i. A predictive formulation could be introduced by using SOC_{i+1} obtained from Coulomb counting with $I_{i,\mathrm{app}}$ and Δt. This limitation is reflected in the overall OCV expression in Eq. (54).

Loop asymmetry. Asymmetric hysteresis behavior can be realized via the discrete weight distribution $\mu_{i,\alpha_{\hat{i}},\beta_{\hat{j}}}$, which is the only remaining DOF and controls both charge and discharge trajectories via the evolution of α_i and β_i. Strongly asymmetric weight distributions yield asymmetric loops. Because $h_{i,\mathrm{preisach,lit}}$ is intrinsically normalized in $[-1, 1]$, no additional asymmetries are introduced by major loop variations during parameterization. In simulation, besides the loop asymmetry from the weight distribution, further asymmetries arise from SOC-dependent weight inter-/extrapolation, and from scaling with $H_{i,\max}$, which incorporates the holistic OCV hysteresis representation of LFP and graphite.

Parameterization. As for the other hysteresis models, the influence of temperature and C-Rate on the Modified Preisach weights is neglected. The 28 weights $\mu_{i,\alpha_{\hat{i}},\beta_{\hat{j}}}$, as the only DOF, are optimized analogously to the previous models using Eqs. (6), (7), and (8) and the associated parameterization procedure for each minor loop. Due to the model design, the weights are fitted jointly for charge and discharge. For parameterization and analysis, $h_{i,\mathrm{preisach,lit}}$ is transformed to $h_{i,\mathrm{preisach}}$ to ensure comparability:

$$h_{i,\mathrm{preisach}} = \frac{1}{2}(h_{i,\mathrm{preisach,lit}} + 1). \tag{E.1}$$

Yet, since h_{measured} used for parameterization is derived from the holistic OCV hysteresis representation of graphite and LFP, the contributions of each electrode may vary for different values of $SOC_{i,\mathrm{avg,loop}}$ during parameterization. Subsequent simulation uses the original interpretation of the Modified Preisach model. After fitting, the weights are linearly interpolated and extrapolated by clipping to obtain a charge-direction-independent weight lookup table at the above mentioned SOC values. The resulting $\mathrm{MAE}_{\mathrm{fit}}$ according to Eq. (9) is 0.063, corresponding to an average deviation of 6.3 % over all $N_{\mathrm{loop}} \cdot n_{\mathrm{loop}}$ measured hysteresis data points for the Modified Preisach model.

Appendix F. Verification of the parameter identification for the OCV hysteresis models

The parameter identification for the OCV hysteresis models described in Section 3.2 employs Matlab's `fmincon`, a local and gradient-based solver. The objective S according to Eq. (6) is only piecewise smooth with respect to the model parameters for the Roscher and the Modified Preisach model, which include saturation of $\psi_{i,1}$ and $\psi_{i,2}$ and switching through the hysteron operators, respectively. Gradient estimates obtained by finite differences may therefore be inaccurate in the vicinity of such events, and a local minimum cannot be guaranteed to be global a priori. To confirm that the reported parameter sets are independent of the solver and of its initialization, all minor loop fits were repeated with alternative optimization algorithms.

The results are summarized in Table F.11. Two quantities are reported for each algorithm. The parameter deviation compares the identified parameters directly: for each minor loop, the Euclidean norm of the difference between the identified parameter vector and the one obtained with `fmincon` is normalized by the norm of the latter, and the maximum over all N_{loop} minor loops is reported. The parameter vector comprises all parameters identified for the respective minor loop, that is, $\gamma_{i,\mathrm{ch}}$ and $\gamma_{i,\mathrm{dch}}$ for the Plett One-State model, $k_{i,\mathrm{ch}}$ and $k_{i,\mathrm{dch}}$ for the Huria model, $m_{i,\mathrm{ch},1}$, $m_{i,\mathrm{ch},2}$, $m_{i,\mathrm{dch},1}$, $m_{i,\mathrm{dch},2}$ and $\upsilon_{i,1}$ for the Roscher model, and the weights $\mu_{i,\alpha_{\hat{i}},\beta_{\hat{j}}}$ for the Modified Preisach model. Since the norm is evaluated on the unscaled parameters, parameters of larger magnitude contribute more strongly to the deviation. $\Delta\mathrm{MAE}_{\mathrm{fit}}$ compares the resulting fit quality and denotes the absolute difference of $\mathrm{MAE}_{\mathrm{fit}}$ according to Eq. (9), which is evaluated over all minor loops and both charge directions.

Table F.11
Verification of the parameter identification of the OCV hysteresis models. Comparison of the parameterization reported in Table 5, obtained with `fmincon`, against alternative optimization algorithms. The parameter deviation denotes the Euclidean norm of the difference between the identified parameter vector and the reported one, normalized by the norm of the reported vector and taken as the maximum over all N_{loop} minor loops. The parameter vector comprises all parameters identified for the respective minor loop, so that parameters of larger magnitude contribute more strongly to the norm. $\Delta\mathrm{MAE}_{\mathrm{fit}}$ denotes the absolute difference of $\mathrm{MAE}_{\mathrm{fit}}$ according to Eq. (9), evaluated over all minor loops and both charge directions for each algorithm.

	Number of parameters	Optimization algorithm	Parameter deviation /–	$\Delta\mathrm{MAE}_{\mathrm{fit}}$ /–
Plett	2	`fmincon` (reported)	Reference	Reference
One-State		parameter scan[a]	0.001	$<3 \cdot 10^{-5}$
Huria	2	`fmincon` (reported)	Reference	Reference
		parameter scan[a]	0.000	$<5 \cdot 10^{-10}$
Roscher	5	`fmincon` (reported)	Reference	Reference
		`ga`	0.005	$<8 \cdot 10^{-5}$
Modified	28	`fmincon` (reported)	Reference	Reference
Preisach		convex formulation[b]	0.526[c]	$<6 \cdot 10^{-9}$
		`ga`	0.588[c]	$<4 \cdot 10^{-8}$

[a] Exhaustive evaluation of the feasible parameter interval at a resolution of 10^{-4}.
[b] Global optimum according to Eq. (F.1), solved with `lsqlin`.
[c] The weight distribution realizing the optimum is not unique.

Plett One-State and Huria model. Both models are governed by a single parameter per charge direction, which allows the feasible parameter interval to be evaluated exhaustively on a uniform grid, rejecting all points that violate Eqs. (7) and (8). The resulting minimum is global up to the resolution of the grid and is obtained without an initial parameter guess. It coincides with the reported parameterization, confirming that `fmincon` identifies the global optimum for these two models.

Roscher model. Neither an exhaustive evaluation nor a convex reformulation is applicable for this model. The identification was therefore repeated with Matlab's genetic algorithm `ga`, a population-based global search method that requires no initial parameter guess and thus verifies that the identified parameters do not depend on the initialization of `fmincon`. Both algorithms yield the same parameter set and the same $\mathrm{MAE}_{\mathrm{fit}}$ within the precision reported in Table 5.

Modified Preisach model. The output of this model is linear in the weights, since $h_{i,\mathrm{preisach,lit}}$ is a weighted mean of the hysteron states $\zeta_{i,\alpha_{\hat{i}},\beta_{\hat{j}}} \in \{-1, 1\}$ and the hysteron sequence is determined by the input trajectory and the geometry of the Preisach triangle rather than by the weight values. Collecting the hysteron states of all n_{loop} measured normalized minor loop data points in a matrix Z reduces Eq. (6) to the convex quadratic optimization problem

$$\begin{aligned} \min_{\mu} \; S &= \sum_{i=1}^{n_{\mathrm{loop}}} \left((Z\mu)_i - h_{i,\mathrm{measured}}\right)^2 \\ &= \|Z\mu - h_{\mathrm{measured}}\|_2^2 \quad \text{with} \quad \mu \geq 0, \;\; \mathbf{1}^{\top}\mu = 1, \end{aligned} \tag{F.1}$$

which can be solved with Matlab's `lsqlin`. Here, μ denotes the vector of all $\mu_{i,\alpha_{\hat{i}},\beta_{\hat{j}}}$ of a minor loop and $\mathbf{1}$ a vector of ones, so that $\mu \geq 0$ and $\mathbf{1}^{\top}\mu = 1$ correspond to the non-negativity of the weights and to Eq. (35). Eqs. (7) and (8) are satisfied by construction and need not be imposed. Its solution is the global optimum of the identification problem and reproduces the reported $\mathrm{MAE}_{\mathrm{fit}}$, confirming that this value is not limited by the optimization procedure. An additional identification with Matlab's genetic algorithm `ga` yields the same result.

The weight distribution realizing this optimum is, however, not unique. Since an increasing input switches all hysterons along a line $\alpha_{\hat{i}}$ simultaneously and a decreasing input all hysterons along a line $\beta_{\hat{j}}$, and since a minor loop contains a single change in charge direction, only the corresponding line sums of the weight distribution influence the model output during parameterization. Different weight distributions therefore reproduce the measured minor loop identically, which is reflected in the parameter deviation reported in Table F.11. This is a known limitation of identifying a discrete Preisach weight distribution from minor loop data alone; a unique identification would require FORCs of the minor loops themselves, which are not provided by the measurement procedure applied in this work (see Section 2). Repeating the simulation with the differing weight distributions changes the MAE of the simulated OCV negligibly compared to the error contributions discussed in Section 5.1. The non-uniqueness is therefore not relevant for the results presented in this work and is not considered further.

Summary. Table F.11 reports the deviation of the parameters identified with the alternative algorithms from those obtained with `fmincon`, together with the resulting change of $\mathrm{MAE}_{\mathrm{fit}}$. For the Plett One-State, the Huria and the Roscher model, both quantities are negligible, so that the parameterizations underlying the values of $\mathrm{MAE}_{\mathrm{fit}}$ reported in Table 5 are reproduced by all algorithms. For the Modified Preisach model, the identified weight distributions differ, while the resulting $\mathrm{MAE}_{\mathrm{fit}}$ remains unchanged, which reflects the non-uniqueness discussed above. Across all models, the results indicate that the reported parameterizations correspond to the global optimum of Eq. (6) and are neither artifacts of the solver nor of its initialization.

Appendix G. Supplementary material for results and discussion

See Figs. G.10–G.12.

Appendix H. Structural properties of the OCV hysteresis models for embedded state estimation

For the intended use of the OCV hysteresis models within observer- and filter-based state estimation, two properties beyond accuracy and drift are relevant: the computational structure of a single time step and the number of parameters that must be stored and interpolated. Both follow from the model formulation and are therefore comparable across models, in contrast to execution times, which depend on the software environment. Since these properties support the recommendations summarized in Table 10 rather than constituting a separate contribution, they are reported here.

The quantities in Table H.12 are obtained by counting, for each model, the elementary operations required to advance the hysteresis sub-model by one time step, based directly on the discrete model equations of Section 3.2. Additions, subtractions, multiplications, comparisons, and saturations are counted as one operation each; divisions and transcendental functions are reported separately, as they differ

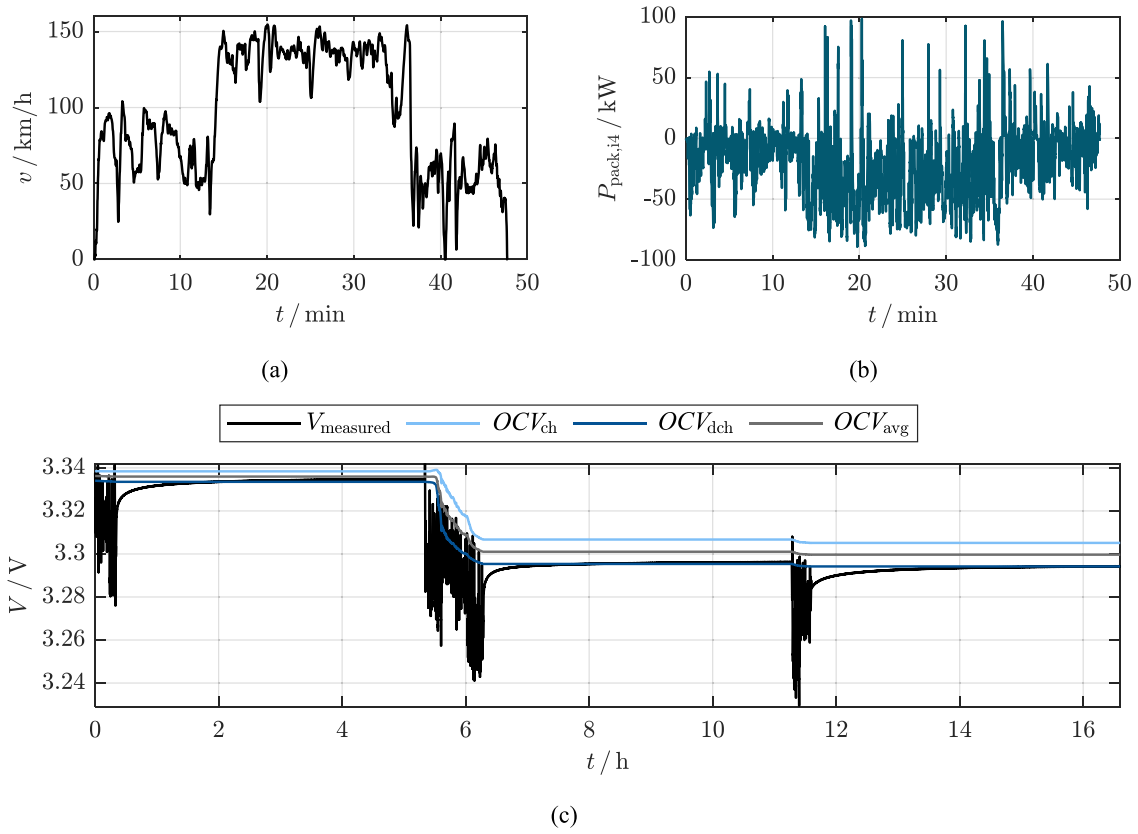


Fig. G.10. Real driving profile of a BMW i4 eDrive40. (a) Speed of the real driving profile. (b) Resulting power requirement of the battery pack $P_{\text{pack,i4}}$. (c) Scaled and extended validation profile with rest phases for validating OCV hysteresis models.

substantially in cost and in their portability to fixed-point arithmetic. Only the branch active in the respective charge direction is counted. The shared ECM with a series resistance and two RC elements is excluded, as it is identical for all models, as are the lookups of the major OCV loops. Accordingly, no operations are attributed to the direct OCV model, which reduces to a lookup of OCV_{dch}, OCV_{avg}, or OCV_{ch}.

The models differ by more than an order of magnitude in operations per time step, from three operations for the Plett Zero-State model to 102 operations for the Modified Preisach model, which evaluates 28 hysterons. For the latter, this worst case occurs only when the switching threshold $\epsilon_{\text{preisach}}$ is exceeded; otherwise the hysteron states and the weighted sum remain unchanged and need not be re-evaluated, so that the threshold introduced for drift mitigation also bounds the average computational cost of this model.

More relevant than the number of operations is their type, as it determines the model's portability to fixed-point arithmetic and to targets without a hardware floating-point unit. The Plett Zero-State, the Roscher, and the Modified Preisach model rely exclusively on multiply-accumulate operations, comparisons, and saturation. The Plett One-State model requires an exponential function in every time step and thus a math library or a piecewise approximation. The Huria model requires a division by $SOC_i - SOC_{i-1}$ for the backward differences; the case $SOC_i - SOC_{i-1} = 0\,\%$ is treated explicitly, but small non-zero increments at low currents and short time steps lead to a loss of significance in single precision and require special numerical handling.

It should be noted that both the exponential function and the division originate from the discretization rather than from the models themselves. As shown in Appendix C, both models are governed by structurally equivalent differential equations and yield exponential minor loop trajectories in continuous time. The Plett One-State model is discretized via the analytical solution, which retains the exponential, whereas the Huria model combines backward differences with a forward Euler step, which introduces the division by $SOC_i - SOC_{i-1}$. The operation types reported in Table H.12 therefore characterize the discretizations investigated here and indicate where an embedded implementation would require adaptation, rather than a fundamental limitation of either model.

The recursion variables reported in Table H.12 denote the values that must be carried from one time step to the next and are distinct from the state-variable interpretation of Table 5: only the Plett One-State model contributes an additional state to the system equation, whereas the recursion variables of the remaining models are internal to the hysteresis sub-model. For the Modified Preisach model, the hysterons are binary and can be stored as a bit field, so that its recursion memory is smaller than the number of variables suggests. Consequently, the demand on writable memory is small for all models, whereas the parameter tables and the associated interpolations per time step scale with the number of model parameters and are dominated by the 28 weights of the Modified Preisach model. These parameter tables remain smaller than the tables of the ECM parameters and of the major OCV loops, which are required irrespective of the hysteresis model. The sensitivity analysis in Section 5.3 is therefore relevant beyond accuracy: omitting the SOC-dependent parameterization reduces the parameter tables of each model to a single set and removes the corresponding interpolations from every time step.

A quantification of execution time, memory occupation, and numerical behavior on a specific automotive MCU is deliberately not attempted. Such figures depend on the target, the compiler and its optimization settings, the fixed-point scaling, and the surrounding task schedule rather than on the hysteresis model itself, and would therefore not generalize across the model comparison intended in this work. Moreover, the differences between the models reported in Table H.12 are small relative to the computational budget available in automotive

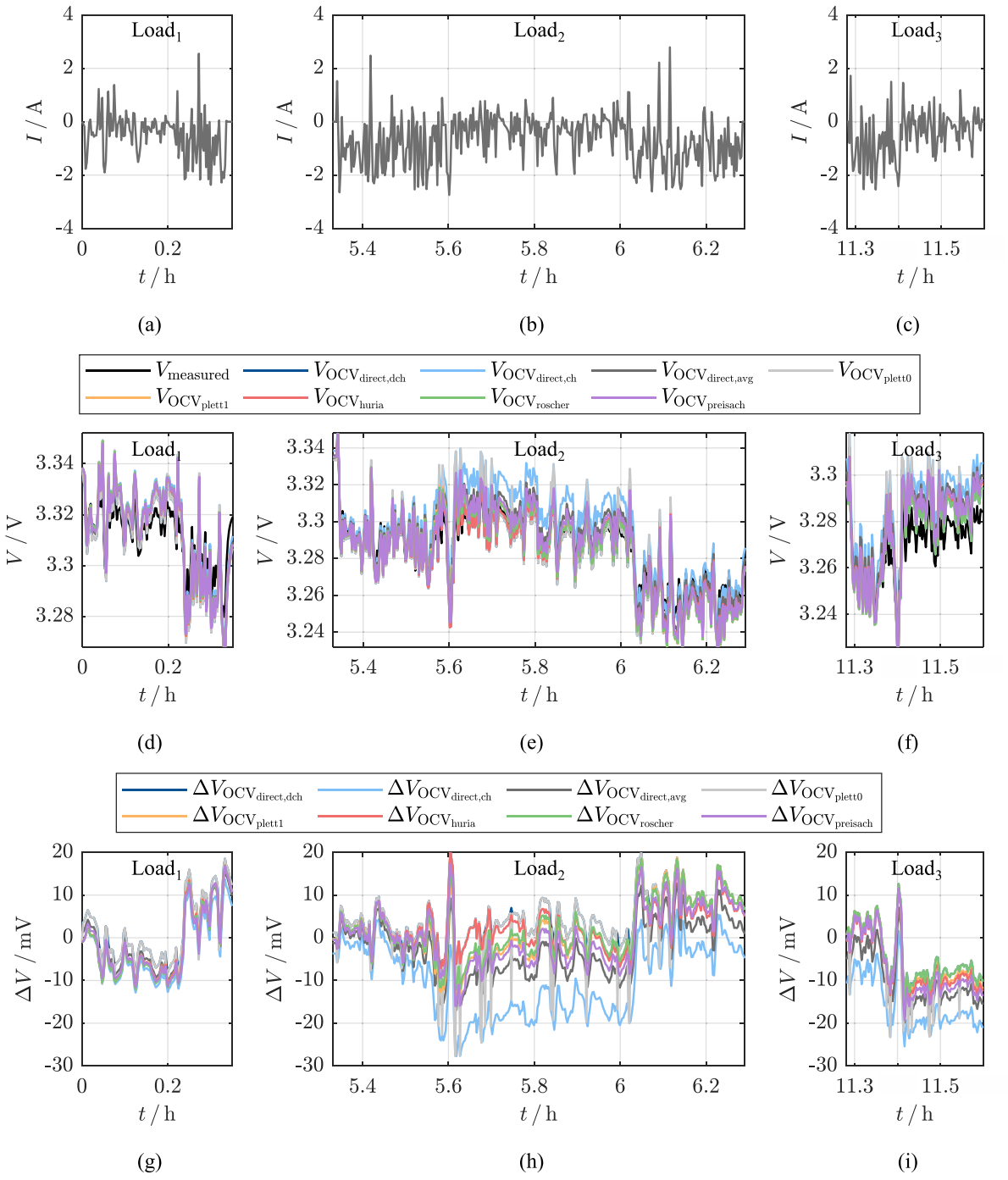


Fig. G.11. Simulation results for three distinct load phases based on the validation profile. (a)–(c) Applied current I_{app} resulting from the scaled power requirement of $P_{pack,i4}$. (d)–(f) Comparison of measured and simulated overall output voltage $V_{measured}$ and $V_{OCV_{mod}}$. (g)–(i) Difference $\Delta V_{OCV_{mod}}$ between measured and simulated overall output voltage.

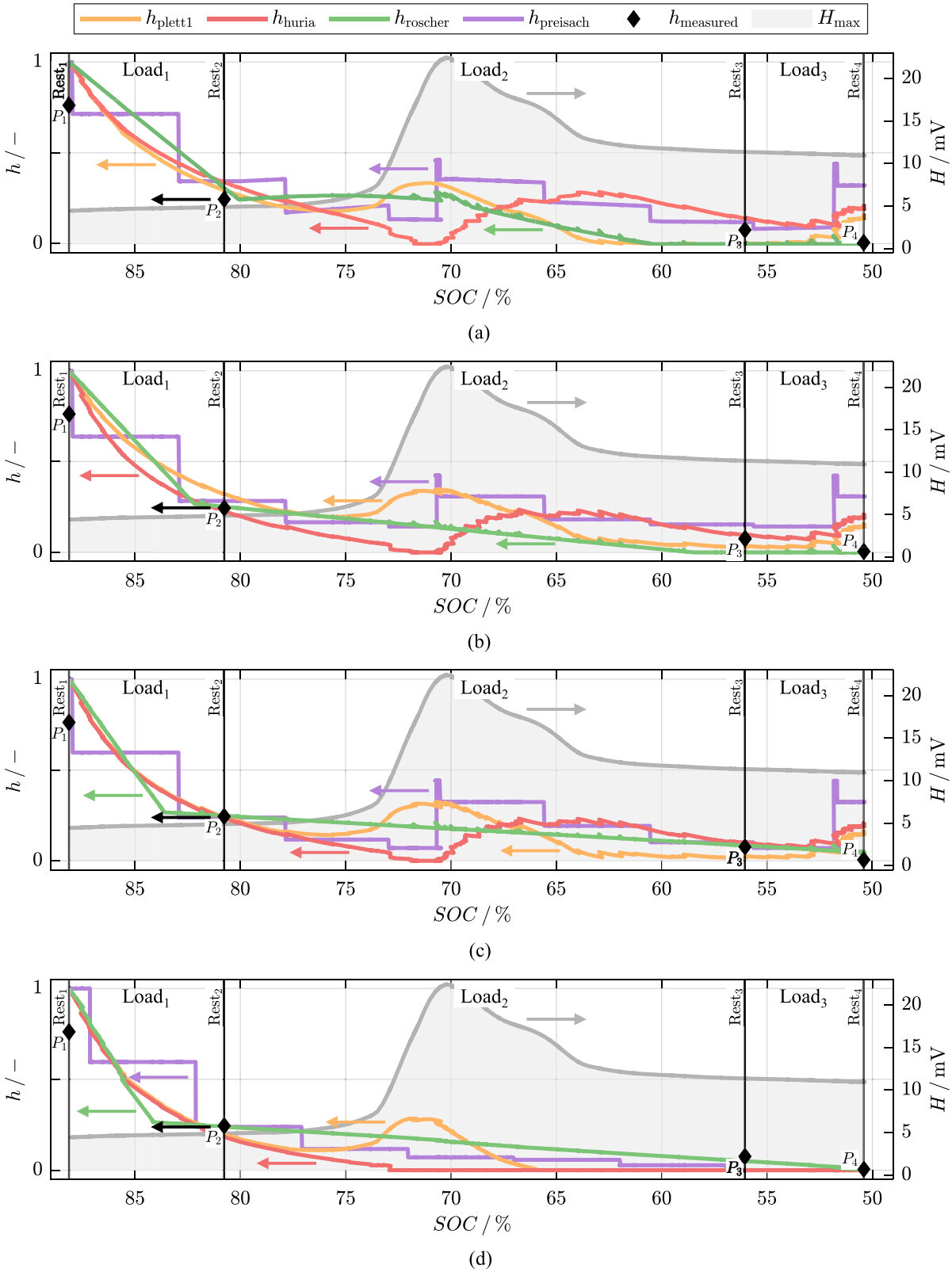


Fig. G.12. Sensitivity analysis of the Plett One-State, the Huria, the Roscher, and the Modified Preisach model for the validation profile, including the OCV hysteresis validation points P_1–P_4, with respect to parameterization, evaluated using h_{mod} over SOC. (a) Baseline implementation with SOC- and charge-direction-dependent parameterization. (b) Averaged parameterization. (c) Optimal parameterization using a single parameter set per charge direction without SOC dependence. (d) Optimal parameterization with suppression of recuperation.

Table H.12
Structural properties of the empirical OCV hysteresis sub-models per time step, derived from the discrete model equations of Section 3.2. The shared ECM with a series resistance and two RC elements is excluded, as it is identical for all models. Operations comprise additions, subtractions, multiplications, comparisons, and saturations; divisions and transcendental functions are listed separately. Recursion variables denote the values carried from one time step to the next and are not to be confused with the state-variable interpretation reported in Table 5, which applies to the Plett One-State model only. Parameters interpolated per time step refer to the SOC-dependent parameters active in the respective charge direction. For the Modified Preisach model, the worst case with hysteron switching is reported.

	Recursion variables	Operations per time step	Division, transcendental	Parameters interpolated per time step
Direct OCV	0	0	–	0
Plett Zero-State	1	3	–	0
Plett One-State	1	12	1 exponential	1
Huria	4	11	1 division	1
Roscher	2	17	–	3
Modified Preisach	28 (binary) + 4	102	–	28

BMS software, so that a measurement on one representative target would not alter any of the model recommendations derived.

Data availability

Data will be made available on request.

References

[1] International Energy Agency, Electric vehicle batteries, 2025, https://www.iea.org/reports/global-ev-outlook-2025/electric-vehicle-batteries. Global EV Outlook 2025, (Accessed 19 May 2026).

[2] S. Evro, A. Ajumobi, D. Mayon, O.S. Tomomewo, Navigating battery choices: A comparative study of lithium iron phosphate and nickel manganese cobalt battery technologies, Futur. Batter. 4 (2024) 100007, http://dx.doi.org/10.1016/j.fub.2024.100007.

[3] L. Yan, J. Peng, H. Li, Z. Huang, D.U. Sauer, W. Li, Breaking the voltage plateau barrier: Slope-adaptive state-of-charge estimation for LFP batteries with temperature-aware hysteresis modeling, ETransportation 26 (2025) 100473, http://dx.doi.org/10.1016/j.etran.2025.100473.

[4] D. Jöst, L.N. Palaniswamy, K.L. Quade, D.U. Sauer, Towards robust state estimation for LFP batteries: Model-in-the-loop analysis with hysteresis modelling and perspectives for other chemistries, J. Energy Storage 92 (2024) 112042, http://dx.doi.org/10.1016/j.est.2024.112042.

[5] L. Jahn, P. Mößle, F. Röder, M.A. Danzer, A physically motivated voltage hysteresis model for lithium-ion batteries using a probability distributed equivalent circuit, Commun. Eng. 3 (1) (2024) 74, http://dx.doi.org/10.1038/s44172-024-00221-4.

[6] A. Umar, S. Mukhopadhyay, A. Patra, Improved state of charge estimation of a Li-ion cell using a fractional order model with hysteresis, J. Energy Storage 103 (2024) 114114, http://dx.doi.org/10.1016/j.est.2024.114114.

[7] D. Chen, L. Sun, F. Shen, G. Gao, Y. Lou, G. Dong, A fuzzy extended PI observer for state of charge estimation of $LiFePO_4$ batteries across broad temperature ranges, J. Energy Storage 128 (2025) 116964, http://dx.doi.org/10.1016/j.est.2025.116964.

[8] D. Chen, S. Xie, G. Dong, Adaptive OCV hysteresis modeling for $LiFePO_4$ SOC estimation via unscented Kalman filter, in: 2025 IEEE 26th China Conference on System Simulation Technology and its Applications, CCSSTA, IEEE, 2025, pp. 1003–1009, http://dx.doi.org/10.1109/IEEECONF65522.2025.11137268.

[9] Z. Zhang, Y. Li, H. Wang, L. Lu, X. Han, D. Li, M. Ouyang, A comparative study of the $LiFePO_4$ battery voltage models under grid energy storage operation, J. Energy Storage 75 (2024) 109696, http://dx.doi.org/10.1016/j.est.2023.109696.

[10] P. Venegas, D. Gómez, M. Arrinda, M. Oyarbide, H. Macicior, A. Bermúdez, Kalman filter and classical Preisach hysteresis model applied to the state of charge battery estimation, Comput. Math. Appl. 118 (2022) 74–84, http://dx.doi.org/10.1016/j.camwa.2022.05.009.

[11] G. Oyama, Y. Yamada, R.-i. Natsui, S.-i. Nishimura, A. Yamada, Kinetics of nucleation and growth in two-phase electrochemical reaction of Li_xFePO_4, J. Phys. Chem. C 116 (13) (2012) 7306–7311, http://dx.doi.org/10.1021/jp300085n.

[12] P. Bai, D.A. Cogswell, M.Z. Bazant, Suppression of phase separation in $LiFePO_4$ nanoparticles during battery discharge, Nano Lett. 11 (11) (2011) 4890–4896, http://dx.doi.org/10.1021/nl202764f.

[13] V. Srinivasan, J. Newman, Discharge model for the lithium iron-phosphate electrode, J. Electrochem. Soc. 151 (10) (2004) A1517, http://dx.doi.org/10.1149/1.1785012.

[14] M. Farkhondeh, C. Delacourt, Mathematical modeling of commercial $LiFePO_4$ electrodes based on variable solid-state diffusivity, J. Electrochem. Soc. 159 (2) (2011) A177, http://dx.doi.org/10.1149/2.073202jes.

[15] M. Safari, C. Delacourt, Mathematical modeling of lithium iron phosphate electrode: Galvanostatic charge/discharge and path dependence, J. Electrochem. Soc. 158 (2) (2010) A63, http://dx.doi.org/10.1149/1.3515902.

[16] W. Dreyer, J. Jamnik, C. Guhlke, R. Huth, J. Moškon, M. Gaberšček, The thermodynamic origin of hysteresis in insertion batteries, Nat. Mater. 9 (5) (2010) 448–453, http://dx.doi.org/10.1038/nmat2730.

[17] G.L. Plett, Extended Kalman filtering for battery management systems of LiPB-based HEV battery packs: Part 2. Modeling and identification, J. Power Sources 134 (2) (2004) 262–276, http://dx.doi.org/10.1016/j.jpowsour.2004.02.032.

[18] T. Huria, G. Ludovici, G. Lutzemberger, State of charge estimation of high power lithium iron phosphate cells, J. Power Sources 249 (2014) 92–102, http://dx.doi.org/10.1016/j.jpowsour.2013.10.079.

[19] M.A. Roscher, D.U. Sauer, Dynamic electric behavior and open-circuit-voltage modeling of $LiFePO_4$-based lithium ion secondary batteries, J. Power Sources 196 (1) (2011) 331–336, http://dx.doi.org/10.1016/j.jpowsour.2010.06.098.

[20] V.H. Duong, N.T. Tran, W. Choi, D.-W. Kim, State estimation technique for VRLA batteries for automotive applications, J. Power Electron. 16 (1) (2016) 238–248, http://dx.doi.org/10.6113/jpe.2016.16.1.238.

[21] M. Thele, O. Bohlen, D.U. Sauer, E. Karden, Development of a voltage-behavior model for NiMH batteries using an impedance-based modeling concept, J. Power Sources 175 (1) (2008) 635–643, http://dx.doi.org/10.1016/j.jpowsour.2007.08.039.

[22] F. Baronti, N. Femia, R. Saletti, C. Visone, W. Zamboni, Preisach modelling of lithium-iron-phosphate battery hysteresis, J. Energy Storage 4 (2015) 51–61, http://dx.doi.org/10.1016/j.est.2015.09.004.

[23] Y. He, R. He, B. Guo, Z. Zhang, S. Yang, X. Liu, X. Zhao, Y. Pan, X. Yan, S. Li, Modeling of dynamic hysteresis characters for the lithium-ion battery, J. Electrochem. Soc. 167 (9) (2020) 090532, http://dx.doi.org/10.1149/1945-7111/ab8b96.

[24] S.R. Huang, S.Y. Chen, S.T. Lai, Application of the Jiles–Atherton model to construct the open-circuit voltage hysteresis model and determine the decommissioning of $LiFePO_4$ batteries, AIP Adv. 15 (3) (2025) http://dx.doi.org/10.1063/5.0252031.

[25] X. Zhao, R.A. de Callafon, Modeling of battery dynamics and hysteresis for power delivery prediction and SOC estimation, Appl. Energy 180 (2016) 823–833, http://dx.doi.org/10.1016/j.apenergy.2016.08.044.

[26] C.S. Chin, Z. Gao, J.H.K. Chiew, C. Zhang, Nonlinear temperature-dependent state model of cylindrical $LiFePO_4$ battery for open-circuit voltage, terminal voltage and state-of-charge estimation with extended Kalman filter, Energies 11 (9) (2018) 2467, http://dx.doi.org/10.3390/en11092467.

[27] T. Gallien, G. Brasseur, State of charge estimation of a $LiFePO_4$ battery: A dual estimation approach incorporating open circuit voltage hysteresis, in: 2016 IEEE International Instrumentation and Measurement Technology Conference Proceedings, IEEE, 2016, pp. 1–6, http://dx.doi.org/10.1109/I2MTC.2016.7520600.

[28] J. Schmitt, I. Horstkötter, B. Bäker, A novel approach for modelling voltage hysteresis in lithium-ion batteries demonstrated for silicon graphite anodes: Comparative evaluation against established Preisach and Plett model, J. Power Sources Adv. 26 (2024) 100139, http://dx.doi.org/10.1016/j.powera.2024.100139.

[29] X. Yang, S. Wang, P. Takyi-Aninakwa, X. Yang, C. Fernandez, Improved noise bias compensation-equivalent circuit modeling strategy for battery state of charge estimation adaptive to strong electromagnetic interference, J. Energy Storage 73 (2023) 108974, http://dx.doi.org/10.1016/j.est.2023.108974.

[30] M. Nagode, A. Gosar, C.A. Sweeney, J. Jaguemont, J. Van Mierlo, D. Šeruga, Mechanistic modelling of cyclic voltage-capacity response for lithium-ion batteries, Energy 186 (2019) 115791, http://dx.doi.org/10.1016/j.energy.2019.07.121.

[31] Z. Xu, J. Wang, Q. Fan, P.D. Lund, J. Hong, Improving the state of charge estimation of reused lithium-ion batteries by abating hysteresis using machine learning technique, J. Energy Storage 32 (2020) 101678, http://dx.doi.org/10.1016/j.est.2020.101678.

[32] X. Zhang, W. Bai, S. Xie, J. Wang, D. Sutanto, K.M. Muttaqi, A novel multi-scale joint approach for estimating lithium-ion battery model parameters and SOC considering hysteresis effect and temperature, Int. J. Electr. Power Energy Syst. 167 (2025) 110618, http://dx.doi.org/10.1016/j.ijepes.2025.110618.

[33] X. Lai, L. Sun, Q. Chen, M. Wang, J. Chen, Y. Ke, Y. Zheng, A novel modeling methodology for hysteresis characteristic and state-of-charge estimation of $LiFePO_4$ batteries, J. Energy Storage 101 (2024) 113807, http://dx.doi.org/10.1016/j.est.2024.113807.

[34] L. Yan, J. Peng, Z. Zhu, H. Li, Z. Huang, D.U. Sauer, W. Li, Data-driven modeling of open circuit voltage hysteresis for $LiFePO_4$ batteries with conditional generative adversarial network, Energy AI 20 (2025) 100478, http://dx.doi.org/10.1016/j.egyai.2025.100478.

[35] S. Schwunk, N. Armbruster, S. Straub, J. Kehl, M. Vetter, Particle filter for state of charge and state of health estimation for lithium-iron phosphate batteries, J. Power Sources 239 (2013) 705–710, http://dx.doi.org/10.1016/j.jpowsour.2012.10.058.

[36] C. Visone, W. Zamboni, Loop orientation and Preisach modeling in hysteresis systems, IEEE Trans. Magn. 51 (11) (2015) 1–4, http://dx.doi.org/10.1109/tmag.2015.2434419.

[37] X. Hu, S. Li, H. Peng, A comparative study of equivalent circuit models for Li-ion batteries, J. Power Sources 198 (2012) 359–367, http://dx.doi.org/10.1016/j.jpowsour.2011.10.013.

[38] J. Ma, J. Xie, K. Bai, Comparative study of non-electrochemical hysteresis models for $LiFePO_4$/graphite batteries, J. Power Electron. 18 (5) (2018) 1585–1594, http://dx.doi.org/10.6113/JPE.2018.18.5.1585.

[39] Lithium Werks, ANR26650m1B power cell, 2026, https://lithiumwerks.com/products/lithium-ion-26650-cells/. Product specifications, (Accessed 19 May 2026).

[40] J.P. Schmidt, E. Ivers-Tiffée, Pulse-fitting - A novel method for the evaluation of pulse measurements, demonstrated for the low frequency behavior of lithium-ion cells, J. Power Sources 315 (2016) 316–323, http://dx.doi.org/10.1016/j.jpowsour.2016.03.026.

[41] M.P. Mercer, C. Peng, C. Soares, H.E. Hoster, D. Kramer, Voltage hysteresis during lithiation/delithiation of graphite associated with meta-stable carbon stackings, J. Mater. Chem. A 9 (1) (2021) 492–504, http://dx.doi.org/10.1039/D0TA10403E.

[42] M.A. Roscher, O. Bohlen, J. Vetter, OCV hysteresis in Li-ion batteries including two-phase transition materials, Int. J. Electrochem. 2011 (1) (2011) 984320, http://dx.doi.org/10.4061/2011/984320.

[43] International Energy Agency, Trends in electric car markets, 2025, https://www.iea.org/reports/global-ev-outlook-2025/trends-in-electric-car-markets-2#electric-car-sales. Global EV Outlook 2025, (Accessed 19 May 2026).

[44] X. Tang, X. Zhang, B. Koch, D. Frisch, Modeling and estimation of nickel metal hydride battery hysteresis for SOC estimation, in: 2008 International Conference on Prognostics and Health Management, IEEE, 2008, pp. 1–12, http://dx.doi.org/10.1109/PHM.2008.4711432.

[45] F. Baronti, N. Femia, R. Saletti, W. Zamboni, Comparing open-circuit voltage hysteresis models for lithium-iron-phosphate batteries, in: IECON 2014-40th Annual Conference of the IEEE Industrial Electronics Society, IEEE, 2014, pp. 5635–5640, http://dx.doi.org/10.1109/IECON.2014.7049363.

[46] P. Aher, R. Deshmukh, C. Chavan, S. Patil, M. Khare, A. Mandhana, A comprehensive equivalent circuit model of Li-ion batteries for SOC estimation in electric vehicles based on parametric sensitivity analysis, Ionics 31 (1) (2025) 287–303, http://dx.doi.org/10.1007/s11581-024-05950-2.

[47] K. Huang, K. Sun, Y. Guo, Z. Wang, S. Li, Battery modeling considering hysteresis effect and temperature adaptability, Energy Technol. 11 (3) (2023) 2201064, http://dx.doi.org/10.1002/ente.202201064.

[48] Y. Chang, R. Li, H. Sun, X. Zhang, Estimation of SOC in lithium-iron-phosphate batteries using an adaptive sliding mode observer with simplified hysteresis model during electric vehicle duty cycles, Batteries 10 (5) (2024) 154, http://dx.doi.org/10.3390/batteries10050154.

[49] M. Elmarghichi, M. Bouzi, N. Ettalabi, Robust parameter estimation of an electric vehicle lithium-ion battery using adaptive forgetting factor recursive least squares, Int. J. Intell. Eng. Syst. 13 (5) (2020) 74–84, http://dx.doi.org/10.22266/ijies2020.1031.08.

[50] S. Qiu, Z. Chen, M.A. Masrur, Y.L. Murphey, Battery hysteresis modeling for state of charge estimation based on extended Kalman filter, in: 2011 6th IEEE Conference on Industrial Electronics and Applications, IEEE, 2011, pp. 184–189, http://dx.doi.org/10.1109/ICIEA.2011.5975576.

[51] H. Zheng, Y. Wang, Q. Du, S. Wang, Z. Li, B. Zhu, T. Qin, An advanced moving horizon framework for state of charge estimation in lithium-ion battery, Renew. Energy 256 (D) (2025) 124169, http://dx.doi.org/10.1016/j.renene.2025.124169.

[52] J. Zeng, S. Wang, P. Takyi-Aninakwa, M. Zhang, W. Cao, C. Fernandez, J.M. Guerrero, Battery lumped fractional-order hysteresis thermoelectric coupling model for state of charge estimation adaptive to time-varying core temperature conditions, Int. J. Circuit Theory Appl. 53 (2) (2025) 655–680, http://dx.doi.org/10.1002/cta.4138.

[53] J. Yang, S. Wang, H. Gao, C. Fernandez, J.M. Guerrero, Improved chaotic particle butterfly optimization-cubature Kalman filtering for accurate state of charge estimation of lithium-ion batteries adaptive to different temperature conditions, Ionics 30 (11) (2024) 6933–6949, http://dx.doi.org/10.1007/s11581-024-05777-x.

[54] C. Qi, S. Wang, W. Cao, Y. Wang, D. Liu, C. Fernandez, Improved joint prediction strategy for state of charge and peak power of lithium-ion batteries by considering hysteresis characteristics-current measurement deviation correction, J. Energy Storage 84 (2024) 110726, http://dx.doi.org/10.1016/j.est.2024.110726.

[55] M.A. Pisani Orta, D. García Elvira, H. Valderrama Blaví, Review of state-of-charge estimation methods for electric vehicle applications, World Electr. Veh. J. 16 (2) (2025) 87, http://dx.doi.org/10.3390/wevj16020087.

[56] L. Murugesan, S. Subramaniam, P. Murugesan, A novel approach for enhancing OCV estimation accuracy in EV lithium-ion battery cell employing adaptive segmentation with polynomial fitting, Energy Storage 7 (8) (2025) e70282, http://dx.doi.org/10.1002/est2.70282.

[57] J. Knox, M. Blyth, A. Hales, Advancing state estimation for lithium-ion batteries with hysteresis through systematic extended Kalman filter tuning, Sci. Rep. 14 (1) (2024) 12472, http://dx.doi.org/10.1038/s41598-024-61596-0.

[58] W. Zhou, X. Ma, H. Wang, Y. Zheng, SOC estimation based on hysteresis characteristics of lithium iron phosphate battery, Machines 10 (8) (2022) 658, http://dx.doi.org/10.3390/machines10080658.

[59] S. Nejad, D. Gladwin, D. Stone, A systematic review of lumped-parameter equivalent circuit models for real-time estimation of lithium-ion battery states, J. Power Sources 316 (2016) 183–196, http://dx.doi.org/10.1016/j.jpowsour.2016.03.042.

[60] Z. Zhang, H. Wang, L. Lu, Y. Li, W. Xu, H. Liu, D. Li, M. Ouyang, State-of-charge and capacity estimation for MWh-scale $LiFePO_4$ peak-shaving battery energy storage stations based on real-world operating data, Energy 339 (2025) 139086, http://dx.doi.org/10.1016/j.energy.2025.139086.

[61] Y. Ma, J. Zhu, X. Li, Z. Tang, State of charge and state of health estimation based on dual nonlinear adaptive observer and hysteresis model of lithium-ion battery, J. Renew. Sustain. Energy 13 (4) (2021) 044702, http://dx.doi.org/10.1063/5.0058265.

[62] Z. Zhang, L. Lu, Y. Li, H. Wang, M. Ouyang, Accurate remaining available energy estimation of $LiFePO_4$ battery in dynamic frequency regulation for EVs with thermal-electric-hysteresis model, Energies 16 (13) (2023) 5239, http://dx.doi.org/10.3390/en16135239.

[63] Y. He, Q. Li, X. Zheng, X. Liu, Equivalent hysteresis model based SOC estimation with variable parameters considering temperature, J. Power Electron. 21 (3) (2021) 590–602, http://dx.doi.org/10.1007/s43236-020-00213-5.

[64] V.-H. Duong, N.-T. Tran, Y.-J. Park, W. Choi, Novel estimation technique for the state-of-charge of the lead-acid battery by using EKF considering diffusion and hysteresis phenomenon, Trans. Korean Inst. Power Electron. 19 (2) (2014) 139–148, http://dx.doi.org/10.6113/tkpe.2014.19.2.139.

[65] C.Y. Chun, B. Cho, J. Kim, Covariance controlled state-of-charge estimator of $LiFePO_4$ cells using a simplified hysteresis model, Electrochim. Acta 265 (2018) 629–637, http://dx.doi.org/10.1016/j.electacta.2018.01.178.

[66] C. Chang, Y. Zheng, W. Sun, Z. Ma, LPV estimation of SOC based on electricity conversion and hysteresis characteristic, J. Energy Eng. 145 (6) (2019) 04019026, http://dx.doi.org/10.1061/(asce)ey.1943-7897.0000617.

[67] H. Chen, F. Liu, H. Hou, X. Shen, Estimation of fractional SOC for lithium batteries based on OCV hysteretic characteristics, Ionics 30 (5) (2024) 2627–2641, http://dx.doi.org/10.1007/s11581-024-05442-3.

[68] M. Fleckenstein, O. Bohlen, M.A. Roscher, B. Bäker, Current density and state of charge inhomogeneities in Li-ion battery cells with $LiFePO_4$ as cathode material due to temperature gradients, J. Power Sources 196 (10) (2011) 4769–4778, http://dx.doi.org/10.1016/j.jpowsour.2011.01.043.

[69] P. Fang, A. Zhang, D. Wang, X. Sui, L. Yin, Lumped model of Li-ion battery considering hysteresis effect, J. Energy Storage 86 (2024) 111185, http://dx.doi.org/10.1016/j.est.2024.111185.

[70] S. Parakkadavath, B. Bhikkaji, Identification of the non-linear dynamics and state of charge estimation of a $LiFePO_4$ battery using constrained unscented Kalman filter, IFAC-PapersOnLine 50 (1) (2017) 1571–1576, http://dx.doi.org/10.1016/j.ifacol.2017.08.311.

[71] L. Gagneur, C. Forgez, A.L.D. Franco, Lithium-ion state of charge observer with open circuit voltage hysteresis model, in: 2013 15th European Conference on Power Electronics and Applications, EPE, IEEE, 2013, pp. 1–7, http://dx.doi.org/10.1109/EPE.2013.6631974.

[72] Y. Ko, W. Choi, A new SOC estimation for LFP batteries: Application in a 10 AH cell (HW 38120 L/S) as a hysteresis case study, Electronics 10 (6) (2021) 705, http://dx.doi.org/10.3390/electronics10060705.

[73] J. Xie, J. Ma, Y. Sun, Z. Li, Estimating the state-of-charge of lithium-ion batteries using an H-infinity observer with consideration of the hysteresis characteristic, J. Power Electron. 16 (2) (2016) 643–653, http://dx.doi.org/10.6113/jpe.2016.16.2.643.

[74] J. Xie, J. Ma, K. Bai, State-of-charge estimators considering temperature effect, hysteresis potential, and thermal evolution for $LiFePO_4$ batteries, Int. J. Energy Res. 42 (8) (2018) 2710–2727, http://dx.doi.org/10.1002/er.4060.

[75] P. Chayratsami, G.L. Plett, Hysteresis modeling of lithium-silicon half cells using discrete Preisach model, in: 2018 8th IEEE International Conference on Control System, Computing and Engineering, ICCSCE, IEEE, 2018, pp. 31–36, http://dx.doi.org/10.1109/ICCSCE.2018.8685026.

[76] V. Franzitta, A. Viola, M. Trapanese, Description of hysteresis in lithium battery by classical Preisach model, Adv. Mater. Res. 622 (2013) 1099–1103, http://dx.doi.org/10.4028/www.scientific.net/amr.622-623.1099.

[77] H. Movahedi, N. Tian, H. Fang, R. Rajamani, Hysteresis compensation and nonlinear observer design for state-of-charge estimation using a nonlinear double-capacitor Li-ion battery model, IEEE/ASME Trans. Mechatronics 27 (1) (2021) 594–604, http://dx.doi.org/10.1109/tmech.2021.3068982.

[78] W.-Y. Sun, H.-T. Min, D.-N. Guo, Y.-B. Yu, Modeling of $LiFePO_4$ battery open circuit voltage hysteresis based on recursive discrete Preisach model, Chin. Phys. B 26 (12) (2017) 127503, http://dx.doi.org/10.1088/1674-1056/26/12/127503.

[79] R. Tjandra, S. Thanagasundram, K.J. Tseng, A. Jossen, Improved lithium-ion battery model with hysteresis effect, in: 2014 IEEE Transportation Electrification Conference and Expo, ITEC, IEEE, 2014, pp. 1–8, http://dx.doi.org/10.1109/ITEC.2014.6861809.

[80] L. Zhu, Z. Sun, H. Dai, X. Wei, A novel modeling methodology of open circuit voltage hysteresis for $LiFePO_4$ batteries based on an adaptive discrete Preisach model, Appl. Energy 155 (2015) 91–109, http://dx.doi.org/10.1016/j.apenergy.2015.05.103.

[81] P. Chayratsami, G.L. Plett, Hysteresis modeling of lithium-silicon half cells using Prandtl-Ishlinskii model, in: 2020 IEEE 16th International Conference on Control & Automation, ICCA, IEEE, 2020, pp. 1578–1583, http://dx.doi.org/10.1109/ICCA51439.2020.9264350.

[82] L. Yan, J. Peng, Y. Wu, Z. Zhu, H. Li, Z. Huang, Optimal operator-based modeling for open circuit voltage hysteresis of $LiFePO_4$ batteries, in: 2024 IEEE International Conference on Systems, Man, and Cybernetics, SMC, IEEE, 2024, pp. 71–76, http://dx.doi.org/10.1109/SMC54092.2024.10831251.

[83] H. Zhang, B. Hu, Z. Yu, H. Wang, L. Qu, J. Wang, W. Li, C. Bai, Y. Sun, et al., State-of-charge estimation of lithium-ion battery based on improved equivalent circuit model considering hysteresis combined with adaptive iterative unscented Kalman filtering, J. Energy Storage 102 (2024) 114105, http://dx.doi.org/10.1016/j.est.2024.114105.

[84] M. Trapanese, V. Franzitta, A. Viola, The jiles atherton model for description of hysteresis in lithium battery, in: 2013 Twenty-Eighth Annual IEEE Applied Power Electronics Conference and Exposition, APEC, IEEE, 2013, pp. 2773–2775, http://dx.doi.org/10.1109/APEC.2013.6520689.

[85] N.A. Windarko, J. Choi, SOC estimation based on OCV for NiMH batteries using an improved takacs model, J. Power Electron. 10 (2) (2010) 181–186, http://dx.doi.org/10.6113/jpe.2010.10.2.181.

[86] A. Umar, J. Sahoo, S. Mukhopadhyay, A. Patra, Onboard estimation of state of charge for Li-ion cells using fractional order model with hysteresis, in: 2025 IEEE/AIAA Transportation Electrification Conference and Electric Aircraft Technologies Symposium, ITEC+ EATS, IEEE, 2025, pp. 1–6, http://dx.doi.org/10.1109/ITEC63604.2025.11098022.

[87] I. Mayergoyz, Mathematical models of hysteresis, IEEE Trans. Magn. 22 (5) (1986) 603–608, http://dx.doi.org/10.1109/tmag.1986.1064347.

[88] K. An, G.-p. Cai, Discretization of Preisach hysteresis model, J. Cent. South Univ. 22 (12) (2015) 4724–4730, http://dx.doi.org/10.1007/s11771-015-3024-6.

[89] I. Mayergoyz, P. Andrei, Preisach modeling of clockwise hysteresis and its application to front propagation problems, J. Appl. Phys. 91 (10) (2002) 7645–7647, http://dx.doi.org/10.1063/1.1453311.

[90] M. Hedegård, T. Wik, Non-parametric convex identification of extended generalized Prandtl-Ishlinskii models, Automatica 50 (2) (2014) 465–474, http://dx.doi.org/10.1016/j.automatica.2013.12.010.

[91] M. Al Janaideh, S. Rakheja, C.-Y. Su, An analytical generalized Prandtl-Ishlinskii model inversion for hysteresis compensation in micropositioning control, IEEE/ASME Trans. Mechatronics 16 (4) (2010) 734–744, http://dx.doi.org/10.1109/tmech.2010.2052366.

[92] H. Zhang, M.-Y. Chow, On-line PHEV battery hysteresis effect dynamics modeling, in: IECON 2010-36th Annual Conference on IEEE Industrial Electronics Society, IEEE, 2010, pp. 1844–1849, http://dx.doi.org/10.1109/IECON.2010.5675395.

[93] H.R. Eichi, M.-Y. Chow, Modeling and analysis of battery hysteresis effects, in: 2012 IEEE Energy Conversion Congress and Exposition, ECCE, IEEE, 2012, pp. 4479–4486, http://dx.doi.org/10.1109/ECCE.2012.6342212.

[94] Y. Ding, T. Zhang, B. Cheng, Y. Yang, D. Deng, W. Li, State-of-charge estimation of the battery based on improved equivalent circuit model and adaptive extended Kalman filter, in: 2025 IEEE International Conference on Industrial Technology, ICIT, IEEE, 2025, pp. 1–6, http://dx.doi.org/10.1109/ICIT63637.2025.10965211.

[95] C. Chang, Y. Zheng, Y. Yu, Estimation for battery state of charge based on temperature effect and fractional extended Kalman filter, Energies 13 (22) (2020) 5947, http://dx.doi.org/10.3390/en13225947.

[96] N. Wassiliadis, J. Adermann, A. Frericks, M. Pak, C. Reiter, B. Lohmann, M. Lienkamp, Revisiting the dual extended Kalman filter for battery state-of-charge and state-of-health estimation: A use-case life cycle analysis, J. Energy Storage 19 (2018) 73–87, http://dx.doi.org/10.1016/j.est.2018.07.006.

[97] S. Klick, G. Stahl, D.U. Sauer, The influence of electrolyte volume on calendaric aging of lithium-ion batteries, Energy Technol. 12 (1) (2024) 2300566, http://dx.doi.org/10.1002/ente.202300566.